# Waveguide Single-Photon and Photon-Number-Resolving Detectors

PROEFSCHRIFT

ter verkrijging van de graad van doctor aan de
Technische Universiteit Eindhoven, op gezag van de
rector magnificus, prof.dr.ir. C.J. van Duijn, voor een
commissie aangewezen door het College voor
Promoties in het openbaar te verdedigen
op woensdag 15 januari 2014 om 16.00 uur

door

Döndü Şahin

geboren te Ankara, Turkije

Dit proefschrift van het proefontwerp is goedgekeurd door de promotoren en de samenstelling van de promotiecommissie is als volgt:

voorzitter:    prof.dr.ir. G.M.W. Kroesen
$1^e$ promotor:    prof.dr. A. Fiore
$2^e$ promotor:    prof.dr. G.N. Goltsman (Moscow State Pedagogical University)
leden:    prof.dr. J.J. Finley (Technical University of Munich)
    prof.dr. R.H. Hadfield (University of Glasgow)
    prof.dr.ir. W.M.M. Kessels
    dr. J.J.G.M. van der Tol

STW
Enabling new technology

# Contents

To my parents...

# Abstract

The generation, manipulation and detection of single photons as quantum bits (qubits) are at the very heart of optical quantum information processing. Single-photon sources, passive optical elements and single-photon detectors form the basis of all-optical quantum gates and of linear-optics quantum computing. However, present implementations are limited to few qubits, due to the large number of optical components required. The monolithic integration of quantum photonic circuits, as needed for scaling to tens of qubits, has so far been limited to passive implementations, due to the difficulty of integrating sources, waveguides and detectors on the same substrate. Therefore, the integration of single photon detectors within a single chip with single-photon sources and passive circuit elements is a key research objective, in view of the realisation of quantum photonic integrated circuits (QPICs).

Among the different approaches to detect single photons, nanowire superconducting single-photon detectors (SSPDs) outperform other single-photon detection technologies in near-infrared (NIR) due to their high efficiency, high timing accuracy and short dead time. Their outstanding properties and compatibility with the integration of single-photon sources and passive photonic networks make SSPDs very strong candidates for on-chip implementations. SSPDs are formed of ultrathin (4-5 nm) and narrow (~100 nm) superconducting (mostly niobium nitride (NbN)) nanowires patterned in a meander structure. The absorption of a single photon in the nanowire produces a transition from the superconductive to the resistive state, giving rise to a voltage pulse in the external circuit.

In this thesis, the design, realisation and characterisation of single-photon and photon-number-resolving detectors based on superconducting nanowires integrated with GaAs waveguides are presented. First, the optimisation of the challenging technology of ultrathin NbN film growth on a GaAs substrate by a dc magnetron sputtering technique is discussed. Then, the first demonstration of waveguide single-

photon detectors (WSPDs) based on NbN superconducting ultrathin films on top of GaAs ridge waveguides is introduced. A WSPD with 20% device quantum efficiency, >100 MHz estimated counting rate and 60 ps timing resolution is reported. Moreover, in order to increase the functionality of the QPIC, a beam splitter is realised on-chip by utilizing a 2x2 multi-mode interference coupler (MMI) on GaAs and it is integrated with two detectors as an equivalent of free-space Hanbury-Brown Twiss (HBT) interferometer. Furthermore, it has been shown that an integrated autocorrelator can be realised in a more compact geometry by putting two, electrically separated detectors on the same waveguide. Such a compact device is studied for any possible spurious interaction (namely crosstalk) between the two detection elements which would limit the functionality of the autocorrelators. No crosstalk, however, has been evidenced. Finally, waveguide photon-number-resolving detectors (WPNRDs) have been demonstrated which are able to count the number of photons in a pulse. These WPNRDs are based on the series connection of the nanowires by utilizing spatial multiplexing technique and are shown to resolve up to four photons.

The devices studied within this thesis constitute crucial building blocks of a QPIC with various functionalities and an important step towards the realisation of the fully-integrated optical quantum networks on a single chip.

# Chapter 1

# Introduction

This chapter aims at giving an overview on quantum information processing (QIP), single-photon detectors (SPDs) and photon-number-resolving detectors (PNRDs). First, a brief look at QIP, in particular QIP with photons is taken. Then, the concept of quantum photonic integration is introduced as an approach to scalability in order to replace the room-sized optical tables with a scalable photonic circuit and enable QIP beyond few tens of photons. Afterwards, two building blocks of such a circuit, SPDs and PNRDs and the current state-of-the-art of these elements are discussed. Finally, the chapter is concluded with the scope of this thesis.

## 1.1 Quantum information processing with photons

Whilst the term *photon* is introduced the first time in 1926 by G. N. Lewis[1], the concept of quantised electromagnetic radiation dates back to 1900 when Planck explained the black-body radiation spectrum, which brought him a Nobel prize in physics in 1918. The concept was also used by Einstein to explain the photoelectric effect in 1905 with which he also got a Nobel prize in physics (1921). From then on, it became an attractive research subject for several different branches of optics. In this section, quantum information processing with photons is briefly discussed.

Quantum photonics provides enhancement in precision and speed in quantum simulation and quantum computation. Quantum computation[2] for instance is expected to solve more complex problems than those within the capabilities of conventional computers. In addition, quantum photonics enables the most secure form of cryptography, based on quantum key distribution (QKD)[3].

QIP uses quantum bits (qubits) as a unit of basic information. While the qubits can be based on atomic and solid state systems, photons have emerged as a promising approach for QIP among others in particular for quantum communication and computation[4] owing to their high-speed transmission, low decoherence and the possibility of sending them to different parts of a circuit on quantum network. The low decoherence property of photons

assures long-distance and secure quantum communication, and potentially faster and more precise simulations of quantum systems, such as many-body interactions.

## 1.1.1 Quantum communication

Confidentiality is a common concern as it affects people in their daily lives, for instance in internet banking or digital signatures. Quantum cryptography, also known as QKD, provides the most secure communication between two parties by exploiting the superposition principle and non-classical correlations in quantum mechanics[3]. That is classically impossible via an insecure communication channel because the transmission in a classical channel is subject to inspection by an eavesdropper[5].

QKD relies on single-photons which are transmitted at the speed of light and they are impossible to clone owing to their quantum mechanical nature. The inherent low-noise nature fosters the reliability of photons for such an application. As currently there is no efficient ideal single-photon source available, highly-attenuated laser pulses (typically down to an average photon number $\mu = 0.1$[3]) are used. After a single photon is generated, it is transmitted through a quantum channel, which could be either fibers or free space links before being detected by single-photon detectors.

Quantum cryptography was demonstrated experimentally the first time in 1989 (but only published in 1992)[6] but there are still several limitations for practical implementation. There are stringent requirements such as low-loss transmission, efficient single-photon detectors compatible with telecommunication wavelengths as well as difficulties in realising quantum repeaters. QKD protocols relying on attenuated laser pulses offer unconditional security for practical use only for short distances ($\sim$ 40 km)[7] or if coupled to decoy-state QKD protocol[8]. The imperfections as the channel losses and the detector performance metrics (jitter, dark count, speed and quantum efficiency) put certain limitations to the maximum distance and the bit rate in QKD[9]. QKD can be achieved in free-space only for a limited distance[10] due to beam broadening. The longest distance QKD over 300 km has recently been obtained based on a fiber system using an attenuated laser source and a superconducting single-photon detector (SSPD) with 0.1 cps dark count rate and 5.6 % system detection efficiency at 1550 nm wavelength[11]. Increasing the distance much further requires the implementation of quantum repeaters[3], which rely on linear-processing and photon-detection, and on quantum memories. For practical applications, it will be very advantageous to integrate such quantum repeaters on a chip.

## 1.1.2 Quantum simulators

The idea of simulating quantum systems dates back to 1981 when Feynman gave a talk titled, *Simulating Physics with Computers* (published one year after[12]). Quantum simulators offer an environment that exploits another quantum system obeying the same rules of quantum mechanics as the system to be simulated, but easier to measure. The concept can be clarified by a comparison to a classical counterpart such as classical orreries[1].

---

[1]Classical orreries[13] are three dimensional models that illustrate the relative positions and motions of celestial bodies in the solar system. The bodies are mechanically driven by using the gearwheels in order to mimic the orbital motions.

Classical orreries simulate the motion of the planets and moons in the solar system while quantum computers simulate the many-body interactions of quantum systems.

Quantum simulators are especially essential to tackle the problems that are infeasible to solve on conventional computers. For instance, calculating the ground state energies of many-body systems becomes exponentially harder by using the classical supercomputers as the number of particles increases whilst it gets only polynomially difficult for a simulating quantum system. It is expected that quantum simulators with approximately 150 qubits may outperform supercomputers[14].

The photonic implementations of quantum simulators are being investigated in Ref.[14].

### 1.1.3 Quantum computers

In quantum computers, the conventional bits (0 and 1) are replaced with qubits. Thus, the value of a bit is no longer only 0 or 1 but any superposition of those. For some important problems that are computationally difficult on classical computers (like the factorization of large numbers), quantum computers offer exponentially speed-up due to their inherent parallelism (entanglement). This means that the number of operations needed scales polynomially with the scale of the problem rather than exponentially as in classical computers. This does not mean that quantum computers are universally faster, they might be even slower in some cases compared to the computers available today (with $>$ 3 GHz clock speed). Therefore, they are only promising and useful for particular applications or algorithms where their inherent computational parallelism is an advantage.

There is a great research interest to establish this promising technology with various systems. Spin systems, trapped atoms, superconducting qubits and photons are a few to mention. Photons are a promising approach[2,4] owing to their low-decoherence and the ease of exchanging photons between different parts of the processor. There are, however, formidable challenges to be solved in order to implement a quantum computer on a photonic or any other technology. Therefore, quantum computers are likely the last to appear as a commercial application of quantum physics among the others mentioned in this section.

## 1.2 Quantum photonic integration circuit

It is very challenging to implement any of the above mentioned quantum processing functionalities on a large scale with bulk optics due to the extreme stability requirement as well as the complexity in size and coupling losses that scale proportionally with the number of circuit elements. Integrated quantum photonics[15] offers a solution to those formidable challenges by replacing the bulk optics with a more compact and efficient integrated configuration. Currently, many quantum optics experiments are already conducted with integrated passive circuit elements (optical waveguides). They provide a link to the external network by interfacing with fibers, and the coupling of the photons generated to the rest of the circuit[16–18]. So far, the most common material for the passive circuitry is silica. That is because it is possible to fabricate 3D waveguides on silica and it is low-loss
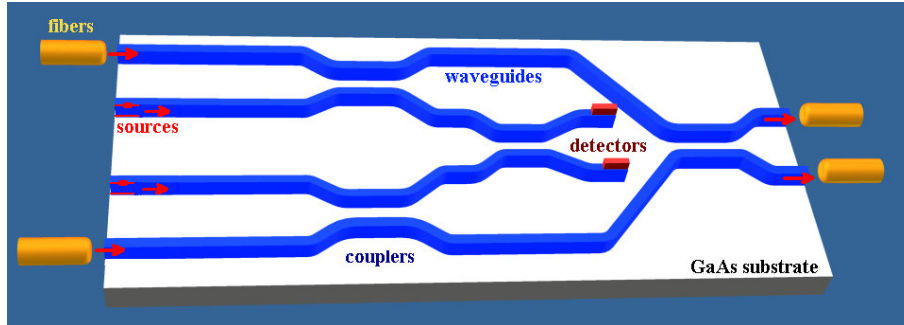
Figure 1.1 – Sketch of a quantum photonic integrated circuit (QPIC) to be realised on a GaAs substrate. Such a circuit allows the quantum processing fully *on-chip* where single-photon sources and detectors are integrated with the passive circuit elements.

at telecom wavelengths[19]. Silicon photonics offer a denser integration level than silica and is therefore being considered for quantum integration photonics[20].

In order to realise a fully-functional quantum photonic integrated circuit (QPIC), all the optical components, such as single photon sources, passive circuit elements and single photon detectors are required to be integrated on a single chip[15]. For the realisation of a fully integrated QPIC[21], the III-V material system is very promising and seems to be a straight-forward approach because it includes direct bandgap materials and allow the integration of single-photon sources[22]. GaAs and InP are the strongest candidates amongst III-V semiconductor compounds since heterostructures emitting in telecom band (1300 - 1550 nm) can be grown epitaxially which is compatible with the well-developed low-loss fiber technology. Additionally, as compared to silicon and silica, GaAs and InP provide the advantage of a second-order optical nonlinearity (useful for realising phase modulators).

As a single photon source, quantum dots (QDs) have attracted considerable attention due to their potential to be integrated with photonic crystals (PhCs)[23–26]. As compared to integrated single-photon sources based on parametric processes in $LiNbO_3$[27] or Si waveguides[28], QDs offer the advantage of much easier filtering of the probe beam.

As detectors, both SPDs and PNRDs are needed for a QPIC in order to increase the functionality of the circuit. There are different type of detectors, such as semiconductor- and superconductor-based and will be discussed in the next section. At the beginning of this thesis, no waveguide single-photon detectors had been demonstrated. In 2011, our group (see chapter 4 of this thesis)[29], a University Oxford/NIST collaboration[30] and a group in Yale[31] almost simultaneously demonstrated waveguide detectors based on GaAs, silica and silicon, respectively. In the last two years, waveguide detectors have been demonstrated also on $Si_3N_4$[32] and again GaAs[33].

Figure 1.1 shows a sketch of our proposal to QPIC. The circuit contains single photon sources based on two level systems (such as QDs in a photonic crystal) and interfaced to the rest of the chip with passive waveguides[25,34]. The linear processing based on waveguides also is obtained on the same chip (see chapter 5) and finally the photons are detected either by waveguide single-photon detectors (WSPDs, see chapter 4) or

photon-number-resolving detectors (WPNRDs, see chapter 6) based on superconducting nanowires[29,35,36].

## 1.3 Single-photon detectors (SPDs)

The interest in SPDs is growing for the applications, including but not limited to single-molecule spectroscopy and light detection and ranging (LIDAR). In this thesis, SPDs for integrated quantum photonics will be discussed. An SPD typically produces an electrical signal after absorption of a photon. They can be classified into two main groups, based on the material's ability to conduct electricity as semiconducting SPDs and superconducting SPDs. In the first group, photo-multiplier tubes (PMTs) and single-photon avalanche detectors (SPADs) (InGaAs-based for the telecom wavelength range and Si-based for the visible range) are mentioned. These technologies are very mature and the detectors do not require cryogenic temperatures to operate. Nevertheless, they are plagued either by the high dark count rates (DCRs) or the long dead time or by both, particularly at telecom wavelengths. That makes these detectors not suitable for specific applications in QIP where these figures are the primary demands. In the second group, transition-edge sensors (TESs) and SSPDs have developed rapidly in recent years and deserve particular attention. Superconducting detectors require cryogenic temperature. TES detectors intrinsically resolve the photon number in a given pulse while they require extremely low working temperature and are also very slow for high speed QIP. SSPDs, the subject of this thesis, are very promising owing to their high speed, low jitter and low achievable dark counts. For a detailed information on SPDs including the other types that are not mentioned here, the reviews on SPDs[37–40] can be referred.

### 1.3.1 Photo-multiplier tubes (PMT)

PMTs can be built for different spectral ranges by changing the photocathode (see Figure 1.2 (left), which is made of a material with a low workfunction. Photomultiplier tubes operate in a vacuum condition. When a photon hits the photocathode, an electron is ejected. This electron is accelerated by the positive voltage applied on the first dynode so that it can eject other electrons from the successive dynodes. That process continues typically till obtaining about $10^6$ electrons by increasing the voltage drops on each subsequent dynode. That becomes a large enough signal to be detected by ordinary electronics. PMTs offer a reasonable efficiency in particular in the visible range (40 % at $\lambda = 500$ nm while 2 % at $\lambda = 1550$ nm)[41]. Nevertheless, both the DCRs and the dead time restrict its availability in applications like QKD. Moreover because of their physical dimensions, they obviously cannot be integrated.

### 1.3.2 Single-photon avalanche detectors (SPAD)

SPADs are typically operated in so called 'Geiger mode', where the diode is biased in reverse bias with a voltage greater than breakdown voltage. When a photon arrives to the
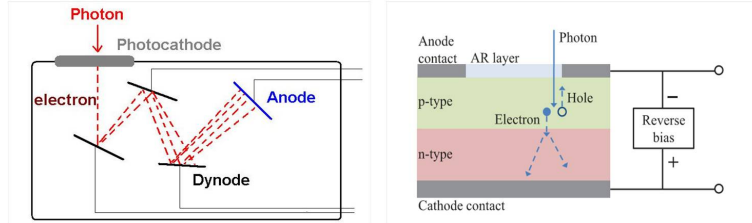
Figure 1.2 – Schematic of (left) a photomultiplier tube, with three dynodes and (right) a single-photon avalanche photodiode from Ref.[39].

active region (below the AR (anti-reflective) window in Figure 1.2(right)), an electron-hole pair is generated. As in PMTs, when the voltage is applied, the charge is accelerated and charge multiplication occurs. The multiplication continues till the saturation current is reached which is usually limited by the external circuit. Once the detection event is registered, the voltage is lowered below the breakdown voltage to make the detector ready for the next detection event.

Geiger-mode Si-SPAD works in the visible spectrum including a part of ultra-violet and near-infrared regimes (350 - 1000 nm). Si-SPAD can have a count rate above 100 MHz[42]. While Si-SPADs can have detection efficiencies as high as 80 % at 800 nm in free running mode[42], the detector efficiency decreases dramatically in the NIR. Therefore, InGaAs/InP-SPADs replace Si-SPADs in the telecom band (1310 and 1550 nm). However, their detection efficiencies drop to $\sim$ 20 % at $\lambda$= 1550 nm[43]. Besides that, the SPADs in the NIR mostly need to be gated as the multiplication layer of the SPADs has trap sites (defects), which are populated during the avalanche. In order to avoid a second avalanche initiated by the trap-site resulting in afterpulsing, those sites need to be depopulated. Afterpulsing requires gating of the InGaAs/InP-SPADs with a long (tens to hundreds of ns) off-time. The detectors are also plagued by the relatively high DCRs, which are in the order of a few kHz[43,44].

Additionally, SPADs are very non-linear (they give the same output pulse for any number of incident photons) and have a high jitter (see section 1.5). If SPADs are biased in the linear mode rather than in Geiger mode, the output signal would be proportional to incident number of photons, enabling the measurement of the number of photons. However, due to the low gain achievable in the linear mode, the signal-to-noise ratio is poor. Operating SPADs at the edge of the Geiger mode has been resulted in photon-number-resolving capability, but with a low signal-to-noise[45]. Therefore, resolving the high photon numbers becomes unfeasible.

## 1.3.3 Transition-edge sensors (TES)

Superconducting TES (also called superconducting phase-transition thermometer -SPT) is a thermal detector that measures the energy of an optical pulse. These type of detectors require a narrow, sharp phase transition from the superconducting to the resistive state at which the increase in resistance with temperature is maximum, since their operation is based on sensing the small resistance change upon photon absorption. A TES works with
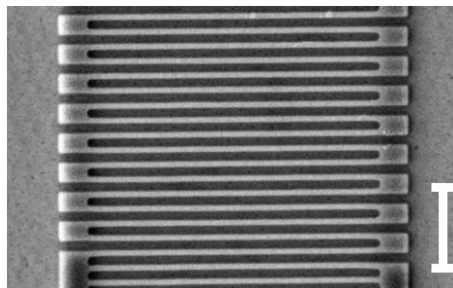
Figure 1.3 – A scanning electron microscope image of a meandered 5x5 $\mu$m SSPD. This design is suitable for free space coupling. The scale bar corresponds to 1 $\mu$m. Fabrication is done by Dr. A. Gaggero in CNR, Rome.

a constant voltage bias for a stable operation. The incident photon energy is absorbed and converted to heat in the absorber material that is thermally in contact with the detector. That raises the temperature of the superconducting material and therefore the resistance. TESs are extremely sensitive to incident photons and have very high detection efficiencies, such as $>$ 90 %[46]. The change in the resistance is measured using a superconducting quantum-interference device (SQUID) array at cryogenic temperatures which complicate the device fabrication. TESs exhibit very low DCRs owing to the extremely low operating temperatures ($<$ 100 mK)[46,47].

While TES are very sensitive to temperature changes, they are relatively slow detectors[2] (maximum count rate of 1 MHz). Thus, TESs are unsuited for high-speed QIP. These detectors inherently show photon-number-resolving (PNR) capability[46] and this will be discussed later in this chapter, in section 1.6.

### 1.3.4 Nanowire superconducting single-photon detectors (SSPDs)

The concept of using superconducting NbN stripes as a single-photon detector dates back to 2001 when first proposed and demonstrated by Golt'sman et. al.[48]. The first proposed structure of an SSPD (also referred as SNSPD) was based on 5 nm-thick and 200 nm-wide NbN nanowire. The detector structure was later modified towards slightly thinner (4-5 nm) and narrower (100 nm) wires folded into a meander (see Figure 1.3) to increase the active interaction area with the incoming photon. Upon absorption of a single-photon, a highly resistive hotspot region is formed by a sequence of relaxation processes. The detection mechanism was first explained on the basis of the hotspot detection model[48,49], which was later refined in 2005[50].

The hotspot mechanism is schematized in Figure 1.4 and explained in the following.

---

[2]The speed of TES detectors is imposed by the maximum bandwidth of SQUID electronics.

## 1.4 Detection mechanism of an SSPD

NbN is a well-known traditional type-II superconductor[51], with high critical temperature ($T_c$) of 17 K (for thick films)[52], a coherence length of $> 100$ nm and a magnetic penetration depth of about 4 - 5 nm[51]. For a sufficiently narrow wire ($< 100$ nm) at the bias current close to the wire's critical current ($I_c$), the hotspot mechanism is used to explain the detection mechanism of SSPDs[48,49]. An SSPD, operating well below its critical temperature ($T \ll T_c= 10 - 12$ K for 4-5 nm-thick NbN), is biased with a current slightly below its critical current, $I_b \sim I_c$ (Figure 1.4(a)). When an incident photon with an energy of $h\nu$ is absorbed, it breaks at first instance a Cooper pair (named after Leon N. Cooper) in the wire– this creates a highly energetic quasi-particle. During the relaxation process, this quasi-particle breaks new pairs successively by inelastic electron-electron scattering ($e^-$ - $e^-$ interaction), causing an avalanche of quasi-electrons from other broken Cooper pairs. The formation of hot-electrons can cause the creation of a resistive region called 'hotspot' in the wire[48]. When the energy of the quasi-electrons becomes close to the superconducting bandgap energy, the quasi-electrons start to recombine and the interaction of the quasi-electrons with the phonons dominates ($e^-$ - $ph$ interaction) over $e^-$ - $e^-$ interaction. This means that the energy of the quasi-particle is dissipated as heat in the material. The photon-induced hotspot is in the scale of few tens of nanometers in diameter depending on the incident photon energy. Therefore, the hotspot is not enough by itself to make the whole section of the wire resistive. Due to the formation of the hotspot, however, the current avoids the resistive region and is expelled to the side-walks (Figure 1.4(b)). At the sidewalks the current density exceeds the critical current density, which also breaks the superconductivity at that region and the whole section becomes resistive (Figure 1.4(c)). This transition from superconducting to normal state is detected as a photoresponse pulse.

Even though the hotspot model is very intuitive and can explain the detection of high-energy photons (in the UV and visible range, Figure 1.5), it suggests a sharp spectral cut-off in the detection efficiency. As the bias decreases, the normal spot size decreases and becomes smaller than the coherence length, $\xi$. For a hotspot size smaller than $\xi$, a resistive state formation is not suggested, meaning that no photon detection should occur. However, in experiments the efficiency decreases continuously with the increasing photon wavelength as shown in Figure 1.5. Therefore, this model was refined later in 2005[50]. Unlike the hotspot model which assumes that all quasi-particles are concentrated in a small cylinder around the hotspot (where the photon is absorbed), the refined hotspot model considers the diffusion of non-equilibrium quasiparticles from the photon absorption spot, in the still superconducting neighbourhood across the wire. The formation of a resistive state due to the redistribution of the supercurrent can also occur without the formation of a normal region. This model has been compared with the experimental results by Semenov et. al. in Ref.[50] and it has shown a better agreement as compared to the original hotspot model. Even though this model predicts better agreement with the experimental results at a longer cut-off wavelength, still does not explain the origin of the photocounts beyond the cut-off wavelength and of the dark counts (see Figure 1.6 right-axis) and their exponential behaviour as a function of the bias current. These effects have been explained by mechanisms related to the vortices. Here, only the current-assisted
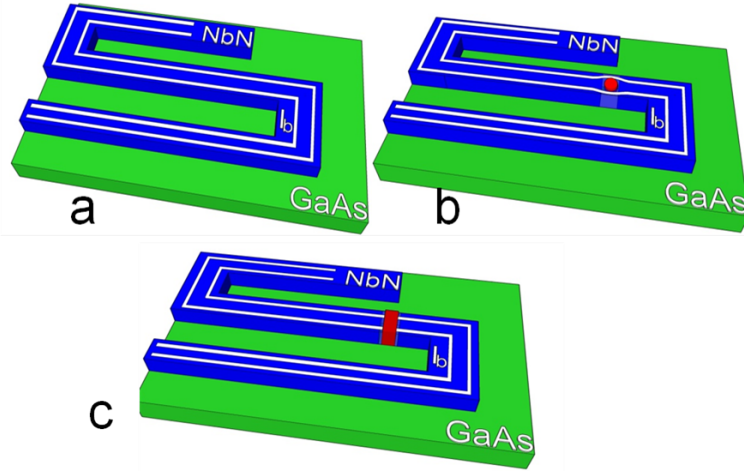
Figure 1.4 – Schematic of the formation of photo-generated resistive hotspot in an ultrathin superconducting wire. a) The wire is biased with a DC bias current close to its critical current, $I_b \sim I_c$. b) The incident photon breaks one Cooper pair and the highly-energetic quasi-particle breaks hundreds of Cooper pairs forming a hotspot (red section of the wire). c) The current density around the resistive region overcomes the critical current density and a resistive belt across the wire is formed.

unbinding of vortex-antivortex pair and the vortex crossing are briefly discussed as the possible mechanisms.

The nanowire can be treated as a 2D superconductor as its thickness is comparable to the $\xi$. For such a superconducting thin film, below $T_c$ the resistance does not vanish. Instead it decreases continuously until a second transition is reached at T= $T_{BKT}$. This transition is defined by the Berezinskii-Kosterlitz-Thouless (BKT) superconducting transition model. Therefore, it is also named BKT transition temperature ($T_{BKT}$). The current-assisted unbinding of vortex-antivortex pairs (VAPs) has been argued by several groups as a possible mechanism to explain the origin of the dark counts [54–56] and also the low-energy photon detection [53]. For this model, the VAPs are free at the temperature between $T_{BKT}$ and $T_c$ and bound below the $T_{BKT}$. These magnetic vortices feel a net Lorentz force exerted on the pairs in the opposite directions when a current passes through the wire. Therefore, the vortices and antivortices align perpendicular to the current direction, where the binding energy reaches to a partial minimum. As the separation between the pairs (r) is current-dependent (r $\propto I_c/I_b$), a high bias current ($I_b \sim I_c$) decreases the binding energy further. Even when the temperature is set well below the BKT transition temperature, at high bias the VAP can be de-paired [53]. Once the VAPs are unbound, they cross the wire perpendicular to the current (to annihilate) and form a finite resistance across the wire, producing a dark count. When a photon is absorbed, the normal state formation becomes more probable. The theoretical argument has been demonstrated to agree well with the experimental data in Refs. [53,55–57] to explain the mechanism of the dark counts as well as low-energy photon detection. Furthermore, a single-vortex crossing
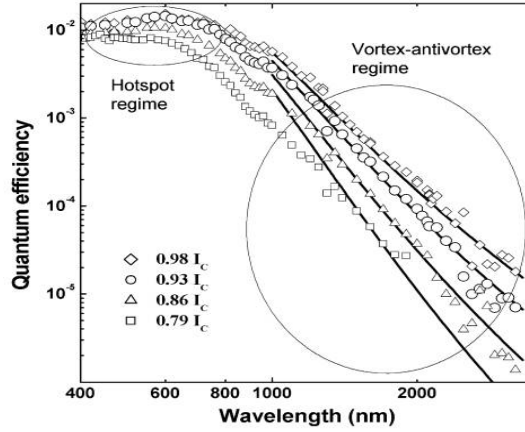
Figure 1.5 – Spectral dependence of the SSPDs. While the detection of the high-energy photons is explained by hotspot mechanism (as a consequence of the formation of a photon-induced non-equilibrium spot), detection at long wavelengths is explained by vortex-antivortex pair- (VAP) model. The quantum efficiency is measured for different bias currents and the solid lines are the obtained from VAP-model fit. The nanowires are 80-nm wide, covering a 4x4 mm$^2$ area with a filling factor of $\sim$ 0.6 on a R-plane sapphire substrate. The figure is taken from Ref.[53].

from one to the other edge of the wire has been argued as another possible mechanism of the dark[58] and photon[59] counts as a vortex-assisted detection mechanism. Thermally-activated single-vortex crossing has been proposed to explain the dark counts in SSPDs for applied current $I_b \geq 0.6\ I_c$ and shown to agree well with the experimental data[58]. Upon a photon absorption, again the mechanism is enhanced and the count rate increases[59].

After a section of the wire has become resistive, due to Joule heating this resistive region grows and the resistance becomes in the order of a k$\Omega$. Then, the current is expelled to the external load resistance ($R_{out}$ =50 $\Omega$ in Figure 1.7) and generates a voltage pulse. By using room temperature amplifiers, the signal is amplified and measured for example by a frequency counter. When the coupling between the material and the thermal heat sink (substrate) overcomes the decreasing Joule heating, the hotspot relaxes, the superconductivity is recovered and therefore the detector becomes ready to detect the next photon (Figure 1.4(a)).

Whilst the time constant of the hotspot formation strongly depends on the material system, it is a very fast process in the order of few tens of picoseconds[60]. On the other hand, the recovery time is determined by the kinetic inductance of the wire (see sub-section 1.5.3) and in the order of few nanoseconds. This recovery is modelled by an electro–thermal equation by considering the effect of the Joule heating[61] and the current at the load resistance simulated from the equivalent circuit as shown Figure 1.7 (left). An SSPD is modelled as a variable resistance ($R_{HS}$) with a parallel switch (open when the photon is absorbed and closed otherwise) and a kinetic inductance ($L_{kin}$). The SSPD is connected to a parallel load resistance ($R_{out}$). The calculated temporal dependence of the
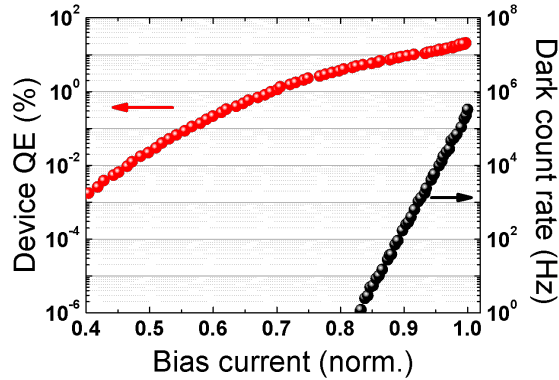
Figure 1.6 – The device quantum efficiency (left-axis) and the dark count rate (right-axis) of a waveguide single photon detector (see chapter 4) as a function of bias current, which is normalised by the critical current. The efficiency measurement is performed at T= 2.1K and the dark measurement at T= 1.2 K.

current distribution on the SSPD ($I_{SSPD}$) and the load ($I_{out}$) is plotted on the right side of the figure with a recovery time given by $\tau_{rise}$[62].

Some performance related parameters of an SSPD– that will be useful in the following chapter(s), are discussed more in detail in the following section.

## 1.5 Performance parameters of an SSPD

The performance of an SSPD is appraised in a variety of terms. Some of the terms which are mentioned in the following are the quantum efficiency (the system and the device quantum efficiency), the dark count rates, the dead time and last but not least the jitter. The emphasis is given to the requirements for the applications discussed at the beginning of this chapter.

### 1.5.1 Quantum efficiency (QE)

QE is the probability that an incident photon generates a measurable signal. Throughout this thesis, the quantum efficiency is referred as percentage, with a maximum QE corresponding to 100 %.

There are two sub-definitions of the QE such as the device quantum efficiency (DQE) and the system quantum efficiency (SQE). The DQE is an intrinsic property of the detector which is directly related with the material and the geometry. It is defined as the probability that the detector clicks when a photon is incident on its active area. It is equal to the product of the absorptance (A) and the internal quantum efficiency ($\eta_i$) (the probability of forming a voltage output upon absorption of a photon), DQE= A$\times\eta_i$. As anticipated from the definition, this value does not include any possible losses that occur before the photon
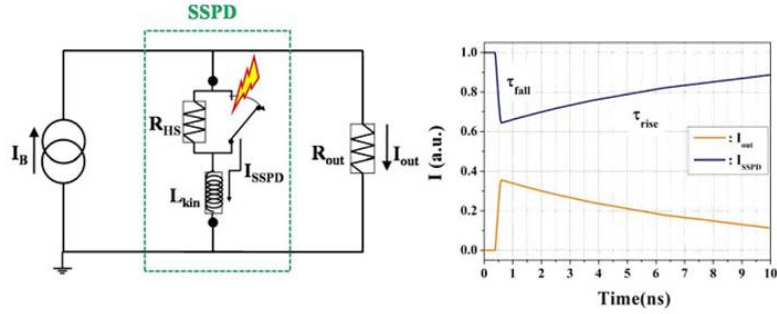
Figure 1.7 – (Left) Equivalent electrical circuit diagram of an SSPD and (right) Inductance-limited recovery of the current for 100 nm-wide and 500 $\mu$m-long NbN nanowire, taken from Ref.[62].

arrives to the detector active region. Therefore, for fiber-based or free-space experiments, another efficiency definition that is more relevant, SQE, is also used. SQE is the probability that the detector clicks if a photon is incident at the input of the detection system (e.g. input fiber, microscope objective, etc.). It is equal to the product of the DQE and the coupling efficiency ($\eta_c$) of the light to the device, SQE= DQEx$\eta_c$. The term $\eta_c$ comprises any loss between the input and the detector.

It is worth mentioning here that this work focuses on the superconducting nanowires integrated with the GaAs ridge waveguides as shown in Figure 1.8 (left), therefore the coupling efficiency $\eta_c$ considers in this system the reflection at the waveguide facet due to high refractive index contrast of air and GaAs, the mode overlap from the fiber to the waveguide and the loss in the waveguide before the photon arrives the detector active region. $\eta_c$ is determined by measuring a simple waveguide with no absorbing wire on top. The DQE and SQE are measured for waveguide detectors in the rest of this thesis as follows (see Figure 1.8 (right)).
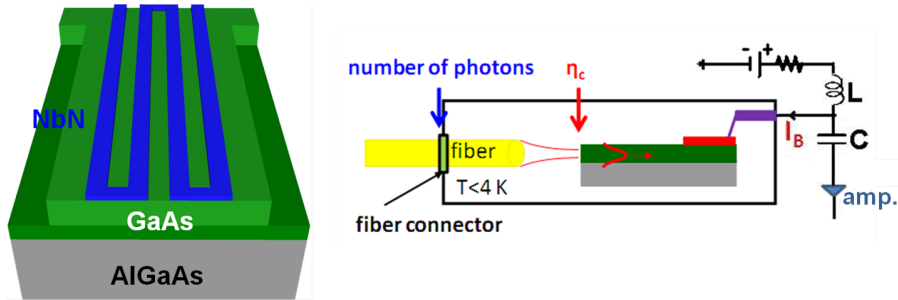


Figure 1.8 – (Left) Sketch of a waveguide SSPD. (Right) The measurements of the system quantum efficiency and the device quantum efficiency in the waveguide probe station. $\eta_c$ is the coupling efficiency. In the biasing circuit, C is the capacitor, L is the inductor and amp. is the amplifier.

The SQE is calculated from:

$$SQE = \frac{N_c}{N_\phi} \tag{1.1}$$

where $N_c$ is the number of counts per second and $N_\phi$ is the number of photons per second coupled to the system at the fiber connector as shown in Figure 1.8 and calculated from $N_\phi = P/h\nu$ where P is the power and $h\nu$ is the photon energy. In this measurement the number of photons absorbed within the detector recovery time is kept $\ll 1$ in order to avoid multiphoton absorption and saturation of the number of counts.

On the other hand, the DQE is the efficiency of the device and is not setup dependent (as long as the operating temperature is kept the same) and calculated from:

$$DQE = \frac{N_c}{N_{\phi\prime}} \tag{1.2}$$

where $N_{\phi\prime}$ is the number of photons incident on the detector coupled in the waveguide and calculated from $N_{\phi\prime} = (P \times \eta_c)/h\nu$, where $\eta_c$ is determined by measuring Fabry-Perot fringes in a waveguide with no NbN wires on top of it. The measurement is explained in subsection 2.2.2.

Being a most practical value for fiber-coupled detectors, in the last years there has been a great effort to maximise the SQE. Up to date, it has been shown that, with a proper choice of optics and a careful alignment, an $\eta_c > 0.90$ can be obtained for single-mode fibers. While SQE is a more practical value to be reported for fiber coupling, the DQE is more relevant for the waveguide detectors since in a QPIC photons will be generated and processed in a waveguide.

As depicted in Figure 1.6, the QE has a strong dependence on the bias current ($I_b$). It increases exponentially with increasing $I_b$ due to the increasing internal quantum efficiency, $\eta_i$. For a higher bias it becomes more probable that the detector clicks when a photon is absorbed as compared to a low bias. In order to operate the detector with a high efficiency, it is very common to bias a detector as close as possible to the maximum current just before it switches to the resistive state. On the other hand, the DCR also increases with $I_b$ as seen in the figure and also discussed in subsection 1.5.2. As the efficiency increases with the bias, it is very common to lower the temperature below 2K both to increase the efficiency and to decrease the dark count.

The detector efficiency depends also strongly on the wavelength of the incident photon (Figure 1.9) as well as it depends on the width of the nanowires. A higher energy photon breaks more Cooper pairs in a nanowire SSPD, which increases the intrinsic efficiency ($\eta_i$) and therefore the detector efficiency. With the similar reasoning, the probability of creating a resistive section is higher with the narrow wires and it is explained further in the following. As discussed previously, according to the hotspot model, a cut-off wavelength is anticipated while the experimental demonstrations disagree with that argument and show a detection ability at wavelengths beyond the anticipated cut-off[50]. In this work, the photon-induced vortex dynamics is invoked as the possible origin.
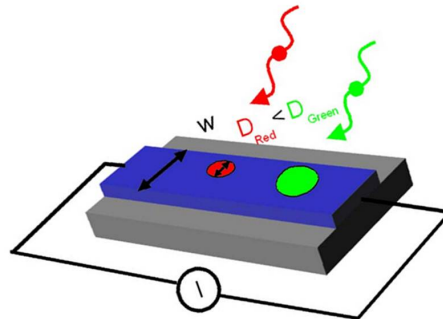
Figure 1.9 – Schematic of a hotspot size for a high-energy (green) and low-energy (red) photon, taken from Ref. [63].

## Limitations to QE and solutions

As anticipated in the previous section, the parameters $\eta_i$ and the A are two important parameters for the device efficiency and each of them needs be maximised in order to achieve a high efficiency.

The first limitation in the QE is due to the $\eta_i$. It means that if one photon is absorbed by the wire, no signal is generated. The low $\eta_i$ can be related to two possible reasons, the film quality and/or the energy of the photon.

The film quality: As the superconducting films used for the detectors are ultrathin ($\sim$4-5 nm), it is quite likely that there are inhomogeneities that limit the bias current and the maximum efficiency , correspondingly. Indeed, if the critical current is locally suppressed due to a variation in the wire width, the crystal structure or the thickness of the film, the bias current is limited by that section and the rest of the wire is biased at a current lower than its critical current. Therefore, only the section of the wire with smaller $I_c$ will be efficient upon photon absorption. This has been investigated in Ref. [64] leaving the question of the exact origin of the inhomogeneities (often referred to as constrictions) still unknown.

The energy of the photon: In order to address the latter reason for a limited $\eta_i$, narrower wires and low bandgap materials are exploited and explained in the following.

- Narrower wires: The energy of NIR photons is smaller compared to the visible photons. The number of broken Cooper pairs is proportional to the photon energy. A NIR photon creates a smaller hotspot as shown in Figure 1.9 and therefore the quantum efficiency of the detector decreases with the wavelength. In order to boost the efficiency by increasing the probability of pulse generation upon a NIR photon absorption (increase $\eta_i$), one approach could be to reduce the width of the nanowires which is traditionally about 100 nm. A quantum efficiency of $> 90$ % has been demonstrated with narrow (70 nm wide) NbN wires located on the waveguide at 1550 nm [31] which exploits also the waveguide structure to satisfy a high absorption condition. Wires as small as 30 nm have been demonstrated to provide a high $\eta_i$ for wavelengths up to 5 $\mu$m [65]. The photoresponse amplitude of

an SSPD is proportional to the bias current and the amplitude of output pulse decreases because of the low bias current. However, this issue has been addressed by connecting the SSPDs in parallel to improve the signal level[66] and therefore the signal-to-noise ratio.

- Low-bandgap superconducting materials: This is another approach to increase $\eta_i$. The number of quasi-particles created by the absorbed photon is proportional to the ratio of the photon energy to the superconducting gap. Therefore, by decreasing the superconducting bandgap, more Cooper pairs are broken for a given photon energy. Materials such as niobium silicide (NbSi)[67], tantalum nitride (TaN)[68] and tungsten silicide ($W_x Si_{1-x}$)[69] with low superconducting bandgap have been investigated in that perspective. $W_x Si_{1-x}$ SSPDs have been demonstrated with an internal quantum efficiency approaching unity and a SQE of 93 % has been reported for an SSPD integrated with a cavity structure[69]. As the crystal structure of WSi is amorphous, it is easier to deposit and therefore more promising among the other low bandgap materials. On the other hand, the maximum $T_c$ for low bandgap wires are generally below 4.2 K and they require cooling to lower temperatures for the operation.

The second limitation in the QE is due to the absorption of the light by ultrathin NbN film. SSPDs are typically fabricated in a meander[48] of 5x5 $\mu m^2$ (see Figure 1.3) or 10x10 $\mu m^2$ in order to couple the light efficiently. The filling factor can be ranging from 18 % to 80 %[70]. However, due to the fact that the thickness of the NbN films for the detectors is very thin (4-5 nm), the absorption is limited and the theoretical limit is calculated to be 30 % on sapphire[71] and 10 % on GaAs[72]. In order to address this limitation, the optical cavities or waveguides are used to enhance the absorptance and these approaches have also been deployed in the following.

- SSPDs integrated with optical cavities: This refers to the challenge in the absorption (A) by ultrathin and narrow superconducting wires. Both the front[48] and the back[71] illuminations put a limit on the maximum absorptance of the incident photon by the nanowires[73]. Meander SSPDs have been demonstrated inside an optical cavity[72,74] in order to create an optical resonance and increase the absorptance. A 57 % DQE has been reported based on NbN nanowires on sapphire at 1550 nm[74]. Moreover, an SQE as high as 80 % has been reported on silica based cavity structure with NbN nanowires at 1550 nm[70]. As already mentioned, WSi has been demonstrated with 93 % system quantum efficiency at 1550 nm, where WSi is embedded in an optical stack to enhance the absorption of the nanowires[69]. Integration of SSPDs with optical microcavities based on GaAs/AlGaAs distributed Bragg reflector (DBR) has shown 18 % DQE at 1300 nm[72].

- SSPDs integrated with waveguides: The absorption efficiency can be also enhanced by exploiting the waveguide geometry where the travelling wave is evanescently coupled to the detector. The waveguide SSPD approach (WSPD as referred in this thesis) benefits from the high modal absorption of the guided mode that allows unity absorptance with waveguide lengths of a few tens of micrometers. Several groups including ours (see chapter 4) have recently presented SSPDs integrated on

Table 1.1 – Comparison of the SSPDs in terms of their efficiencies (QE), measurement wavelengths ($\lambda$) and fabrication approach. In the table, Mat. and $\triangle_0$ stand for material and the superconducting bandgap, respectively.
[a]: on Si, [b]: on GaAs, [c]: on $Si_3N_4$, [*]: SQE, [+]: DQE and [x]: on-chip PL measurement.

| Mat. | QE (%) | $\lambda$ (nm) | Cavity | Waveguide | Low $\triangle_0$ | Width (nm) | Ref. |
|---|---|---|---|---|---|---|---|
| NbSi | < 1 % | 1550 | $\sqrt{}$ | – | $\sqrt{}$ | 100 | [67] |
| WSi | 93 % | 1550[*] | $\sqrt{}$ | – | $\sqrt{}$ | 120 | [69] |
| NbN[a] | ~80 % | 1550[*] | $\sqrt{}$ | – | – | 80 | [70] |
| NbN[a] | 91 % | 1550[+] | – | $\sqrt{}$ | – | 70 - 100 | [31] |
| NbN[b] | 20 % | 1310[+] | – | $\sqrt{}$ | – | 100 | [29] |
| NbN[b] | 20 % | 940 [+,x] | – | $\sqrt{}$ | – | 80 | [33] |
| NbTiN[c] | 70 % | 1542[+] | – | $\sqrt{}$ | – | 60 | [32] |

a waveguide[29–33]. The maximum efficiency has been reported on WSPDs based on NbN nanowires on Si and the DQE reaches to 91 % at the maximum bias current[31]. A DQE of 70 % and 20 % have been reported for NbTiN wires on $Si_3N_4$ and NbN wires on GaAs ridge waveguides, respectively. The results of our waveguide single photon detectors are presented in chapter 4.

As a summary for the state-of-the-art of SSPDs, a comparison is given in Table 1.1. Without any optical structure integrated, the theoretical maximum efficiency cannot exceed 30 % on sapphire ($Al_2O_3$) when the light is illuminated through the substrate[71]. Therefore, enhancement structures such as optical cavities and waveguides are needed to overcome the limited absorptance of the NbN nanowires.

## 1.5.2 Dark count rate (DCR)

A dark count is defined as a false detection event occurring in the *dark condition* of the experimental set-up, i.e. without intentional optical input. It can be originated from two different sources, that can be classified as the intrinsic and extrinsic DCR. The intrinsic DCR can be decreased but stays finite while the extrinsic DCR can be totally eliminated as explained in the following.

The intrinsic DCR is due to thermal fluctuations which produce a switching to the resistive state without photon absorption. While the DCR increases with the $I_b$ (see Figure 1.6), it can be decreased by lowering the operating temperature of the detector. Even though the DCR is lower at low temperatures, the intrinsic DCR does not vanish and stays finite with the sub-critical bias, at $I_b \sim I_c$. It is directly related to the material properties and lower for the high superconducting gap materials as compared to the low band gap ones. The vortex-crossing[54] and non-equilibrium quasiparticle[50] mechanisms are reported as the possible sources of DCR, as also explained previously in subsection 1.5.1.

The IR photon detection could also be the possible source of the dark counts, which is called the extrinsic DCR. Since the SSPDs are still efficient in the mid-infrared region of the electromagnetic spectrum[75], the cryostat requires a proper shielding against blackbody radiation. This is a critical issue particularly for the set-ups with optical windows (see

subsection 2.2.2, Figure 2.12).

### 1.5.3 Dead time and jitter

As for all single photon detectors, SSPDs are *blind* for the next photon for a certain time after the first photon is detected. The second photon cannot be registered if it arrives before the detector is reset. The time needed to recover the bias current of an SSPD ($I_{SSPD}$, see Figure 1.7(right)) is called 'dead time' ($\tau_d$). The dead time is also referred as *recovery time* or *reset time* in the literature. The dead time is in the order of a few nanosecond as illustrated in Figure 1.10 (left) as an example. In this figure, the rising part of the pulse is due to the detection of the photon while the decay part corresponds to the recovery of the current. This time is determined by a negative feedback loop which has been discussed in Refs.[76,77]. The time constant which is given by $\tau_{1/e} = L_k/R_{out}$ (1/e time, shown in Figure 1.10) is imposed by the kinetic inductance ($L_k$) and it is inherent to any thin superconducting film. The current in the wire recovers to about 95 % of its bias value in SSPD in about $3 \times \tau_{1/e}$. As this current allows recovering a QE close to the steady-state value, the dead time is conventionally defined as $\tau_d = 3\tau_{1/e}$[76].

The dead time limits the maximum count rate (CR) of the detector as $CR_{max} \sim 1/\tau_d$. Therefore, to speed up the device, $\tau_d$ needs to be decreased. There are two ways to reduce the time constant, 1- decreasing the $L_k$ by reducing the total length of the wire or 2- by increasing the impedance seen by the detector[78]. The reduction of the wire length may limit the area of the meander and that decreases the coupling efficiency or for the waveguide detectors the absorptance decreases and leads to a lower detection efficiency. Both decreasing the length and increasing the resistance, on the other hand, might lead to 'latching'[61]. The latching occurs when the recovery of the current in the nanowire is faster than the full re-establishment of the superconducting state. Thus, the current recovers and flows back through the detector before its resistance has dropped to zero. Due to the corresponding Joule heating, it cannot recover back to the superconducting phase. This phenomenon is called *latching*. In order to avoid that, these two parameters need to be determined carefully[61,77,78]. Taking latching into consideration, the shortest possible time in a single wire for a large area SSPDs is well below GHz regime[78]. Multi-pixel SSPD geometries have been proposed to overcome the speed limitation[66,77,79]. SSPDs are nevertheless faster than other single-photon detectors. Semiconductor SPDs such as PMTs[41], SPADs[43,80] has a maximum CR ~10 MHz. TES detectors on the other hand are even slower, and have a maximum count rate up to 1 MHz[81].

Jitter (timing jitter, timing resolution) is the timing accuracy of registering a photon, namely the uncertainty in the delay between the photon absorption and the output pulse. While semiconductor SPDs have a non-Gaussian distribution for jitter, SSPDs show a Gaussian-like jitter[82] as shown in Figure 1.10 (right). NbN SSPDs have been reported with jitter as low as 18 ps[83,84]. Low jitter is demanded in fast lifetime measurements using time correlated single-photon counting (TCSPC) since the temporal resolution is determined by that value[85].

Owing to the fast response (a few ns) and low jitter (<50 ps), which are very appealing for high-speed quantum photonic information processing, SSPDs outperform the other SPD technologies in the near-infrared. The other advantage of these detectors is that
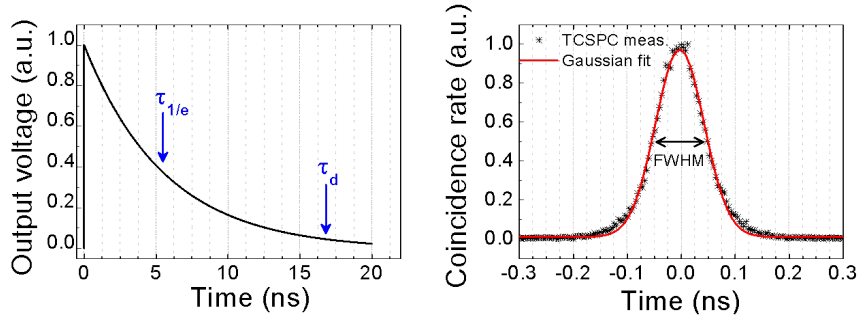
Figure 1.10 – (Left) Simulated pulse shape of a waveguide photon-number-resolving detector. $\tau_d$ is the dead time of the device and it is equal to 3x$\tau_{1/e}$. (Right) Jitter of waveguide detectors measured using time- correlated single-photon counting (TCSPC) module at 0.98x I$_b$ [85]. The data is fit by using Gaussian (red) function.

they do not suffer from afterpulsing although they may latch, which can be avoided by controlling the time constant by changing L$_k$ and R$_{out}$.

## 1.6  Photon-number-resolving detectors (PNRDs)

An SPD is a binary detector and responds in the same way to one or more photons arriving onto the detector at the same time or within the dead time. On the other hand, a PNRD can resolve the number of photons in a single optical pulse. Detectors providing photon-number resolution are important in quantum cryptography, for example to detect the photon-number splitting attacks to the transmission line, and generally in photonic quantum information processing[21]. Recently, there has been a considerable effort to realise photon-number-resolving detectors either by multiplexing single-photon detectors or by using intrinsically photon-number resolving detectors. So far, using the multiplexing technique, SSPDs[77,79,86–88] and avalanche photo-diode detectors[89,90] have been demonstrated. Moreover, charge integration photon detectors[91] and transition edge sensors (TESs)[92] have been shown to resolve the photon number intrinsically. In addition to those, recently in 2008 an avalanche photodetector has been shown to discriminate the photon numbers if the signal is measured at the very early stage of the avalanche[45].

The fidelity of a PNRD is an important figure of merit that gives the probability of measuring n photons when n photons are incident on the detector (P(n|n)). The fidelity can be limited due to several factors, such as the low QE, the limited number of elements, the low signal-to-noise (S/N) ratio and the crosstalk for any type of PNRD. Besides those factors, PNRDs based on time-multiplexing are affected from the transmission losses in the delay line and can be considered as a multi-element detector with different efficiencies. The fidelity limitations for PNRDs based on spatial multiplexing over an array of SPDs (as shown in the inset of Figure 1.11)are discussed in the following.

As widely discussed in the Ref.[86], when n photons arrive on an N-element detector array (for n ≤ N), the fidelity is mainly limited by the low QE ($\eta$) rather than the number
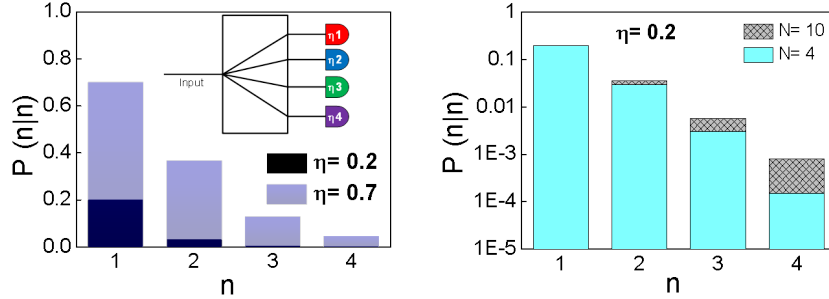
Figure 1.11 – Calculated probability P(n|n) of detecting 1-4 photons with a 4-element PNRD for (left) two different efficiencies of a detector (inset shows the same graph in a log-scale) and (right) two different number of elements, N= 4 and N= 10 with an $\eta$= 0.2, N= 4 and N= 10 with an $\eta$= 1, where $\eta$ is the efficiency and n is the number of photons.

of elements, which is depicted in Figure 1.11. The probability of detecting 1-4 photons, P(n|n) as plotted (left) for different efficiencies, such as $\eta_1$= 0.2 and $\eta_2$= 0.7 and (right) for different number of elements, such as $N_1$= 4 and $N_2$= 10[86]. It is clearly seen that the increase in the QE increases the fidelity dramatically while with a low QE, increasing N has no significant effect. However, once the high QE is achieved, the number of elements will be a limiting factor for the fidelity of a PNRD. For instance, when there are two photons arriving at the same time, there is a chance that two of them will be absorbed by the same element, which produce an error. Moreover, a high S/N is needed for well-separated signal levels, which leads to a clear discrimination of the photon levels. It is shown for four-element PNRD based on four NbN nanowires that a good S/N ratio is obtained[36,87]. The last limitation can be the crosstalk, which is a spurious firing of a detector after photon absorption in an other one. As it is not a real detection event, it is expected to limit the fidelity as well.

PNRDs presented in chapter 6 of this thesis are integrated with GaAs ridge waveguides and called waveguide photon-number-resolving detectors (WPNRDs). WPNRDs are based on four NbN nanowires and show photon-number-resolving capability up to four photons. Before this thesis, only WPNRDs based on transition-edge sensor detectors (TESs) have been reported on an integrated platform based on silica-on-silicon waveguides[30,93]. As TESs are thermal detectors, they are relatively slow and unsuited for high-speed QIP as compared to WPNRDs. In addition, the sub-Kelvin operating temperature complicates their implementation. Therefore, the WPNRDs based on nanowires presented in chapter 6 are more promising.

## 1.7 Scope of this thesis

In this thesis, the design and the experimental demonstration of WSPDs, WPNRDs and more complex detector structures are reported as well as the fabrication and analysis of

simple NbN nanowires on GaAs. chapter 2 covers the experimental methods, including the film deposition, the measurement set-ups, the fabrication processes and the design of the devices. The following four chapters introduce the experimental results achieved in this research. The optimisation and characterisation of NbN ultrathin films on GaAs is discussed in chapter 3. In chapter 4, waveguide single-photon detectors (WSPDs) on GaAs ridge waveguides are introduced. Later in chapter 5, more functional structures with two SSPDs such as integrated multi-mode interference (MMIs) couplers and waveguide auto-correlators are reported. Waveguide autocorrelators are studied to investigate any possible crosstalk (spurious switching effect of a wire after photon absorption in an adjacent one) between closely spaced detector elements. In chapter 6, waveguide photon-number resolving detectors (WPNRDs) are presented based on four nanowires patterned on the same waveguide. Finally, in chapter 7, the results are summarised and the work that has been done towards a fully integrated QPIC is presented.

# Chapter 2

# Experimental Methods

In this chapter, the methods for

- the deposition and characterisation of ultrathin superconducting NbN films

- the processing techniques (mainly of the processing of the simple wires in TU/e),

- the electro-optical measurement setups, and

- the design of the devices and optimisation of the geometry

are presented in this order. They are all related to the experimental results presented in the rest of the thesis.

## 2.1 Fabrication, characterisation and processing of NbN films

The superconducting NbN films are not grown only for waveguide single-photon and photon-number-resolving detectors presented in this thesis but also for other *free-space* activities ongoing within the group. The NbN films are deposited by a sputtering technique on a variety of surfaces, ranging from polished GaAs substrates to distributed-Bragg reflectors (DBRs). Due to the fact that the top layer of the waveguide and DBRs are all GaAs and grown in the same crystallographic direction, optimisation of the films is done on pieces cleaved from single-side polished GaAs (100) wafers. The GaAs substrates are ordered from *Wafer Technology Ltd.*, the DBR structures are grown by both molecular beam epitaxy (MBE) (Mr. R. Hamhuis) and metalorganic vapour phase epitaxy (MOVPE) (Mr. P. J. van Veldhoven) in TU/e and GaAs/AlGaAs waveguide heterostructures are grown by MBE (Mr. M. Lermer) in University of Würzburg. In order to keep the thickness uniformity of the NbN films during the sputtering, the specimens are cleaved into 1x1 cm$^2$ or up to 1.5x1.5 cm$^2$ pieces from the 2-inch wafer.

The films presented in the following chapters are grown by the reactive DC-magnetron sputtering in the *NanoLab@TU/e* cleanroom facility (except the waveguide single photon

detectors presented in *chapter 4*, grown by Dr. A. Gaggero in École Polytechnique Fédérale de Lausanne (EPFL)). Moreover, a lithography process is developed for the first time in TU/e to fabricate simple nanowire structures in order to gain an understanding of the detectors based on NbN superconducting films on GaAs.

## 2.1.1 DC reactive magnetron sputtering

Sputtering is a non-thermal, physical vapour deposition (PVD) process and is suitable for atomic deposition. It can be used to deposit various materials from dielectrics to superconductors with thicknesses from a few nanometers (i.e. NbN films) up to micrometer scale or even to form multi-layer structures[94]. The process is based on the energy and momentum transfer from the ionized sputtering gas to the solid target. For the most efficient momentum transfer, the atomic weight of the ionised gas and the target are chosen to be similar. That brings an advantage of sputtering over evaporation systems as the materials with very high melting temperatures are easily sputtered. Under a low-pressure inert gas (Ar) atmosphere, a high voltage across the anode and the cathode is applied and the plasma is created. Then, the cathode material, i.e. the target (Nb) is bombarded with the inert gas (Ar) ions and the surface atoms of the target are ejected by the highly energetic ions. The specimen on the anode (GaAs) is coated by the bombarded cathode material. Sputtering target can be either an element or a compound. Commonly, nitride and oxide compounds are deposited by introducing a reactive gas such as $N_2$ and $O_2$ into the plasma during the deposition, as in the case to form niobium nitride (NbN). Therefore, this type of technique is called a reactive-sputtering technique.

Sputtering process is done in a high or ultra-high vacuum environment. There are two reasons for that. First of all, it provides a longer mean-free path for the ejected atom. Secondly, it increases the quality of the film in terms of purity by controlling the amount of contamination. Typically a sputter system is operated below $10^{-6}$ Torr[1]. In our processing, the fabrication of superconducting material is very demanding and requires the highest possible purity level. Thus, the base pressure is kept at the level of $\sim 10^{-9}$ Torr which is considered as a ultra-high vacuum.

During this study, a sputtering system from *AJA Intern., INC.*, ATC 1500-F has been used to grow NbN films on different material systems. It is a magnetron (planar, circular configuration) sputtering installed with both DC and RF supplies and the reactive gasses, $N_2$ and $O_2$. In this configuration of the sputtering system, the sputtering mainly occurs between the center and the edges of the target, leading to an erosion of the target in a circular shape. It is equipped with four targets as source materials and each is 2-inch in diameter. In Figure 2.1, the sputter system employed to grow NbN films (top) and the inside of the vacuum chamber with four-chimneys (below) are shown. The parts that are mentioned in the following are highlighted with the numbers. The inlet (1) is where the $N_2$ is introduced into the growth chamber. $N_2$ flow is controlled with a qualified $N_2$ flow meter. The view port (2) is mainly to look through while engaging the sample holder and retracting the "transfer-arm" to the linear, rotary stage and also to observe the plasma during the process. The colour of the plasma can be used to identify if there is any contamination in the chamber. Plasma colour with pure Ar at low-pressures is identified

---

[1]1 Torr = 1.333 mbar

with its characteristic purple emission. It turns to pink-purple with $N_2$ and the oxygen contamination on the other hand changes the colour to the dark-purple. There is also a shutter inside to protect the window from being deposited. Number (3) shows the load-lock chamber which holds a great importance to preserve the high vacuum condition in the main vacuum chamber while transferring the samples. It allows us to introduce a new batch of samples without breaking the high vacuum. Therefore, it takes very short time to condition the vacuum chamber for the next deposition. In a day, typically 2-3 deposition-runs can be made. There are two vacuum gauges (4) available in the system for low (convectron gauge) and high (capacitance manometer) range of vacuum measurement. Number (5) is the bias unit, with which it is possible to adjust the current (voltage) biasing. The unit labelled with (6) is the temperature control unit and it is used for reading and setting a temperature value. In order to be able to stabilize the temperature without damaging the infrared lamp, it is first set to around 100 °C and then ramped up above 400 °C (growth temperature) by changing the proportional, integral and derivative (P-I-D) settings determines present, past and future errors, respectively. Moreover, a picture taken from the inside of the chamber (Figure 2.1(bottom)) shows the chimneys where the targets are mounted. According to the current configuration, the location of the NbN target is shown at (7), and Au, Ti and Cr are located at (8), (9) and (10), respectively. As it is discussed later in this section, Au and Ti are also used in this study but for the pre-conditioning of the chamber.

The samples are prepared by cleaving the wafers into smaller sizes (between 10x10 mm$^2$ and 15x15 mm$^2$) with a diamond-tip scriber along the (110) and (1$\bar{1}$0) crystal orientations. In order to remove the dust deposited on the samples due to the cleaving, every time when new batch of samples is cleaved the samples are cleaned in an ultrasonic bath, using acetone and isopropyl alcohol for 2" each and then dried by blowing $N_2$.

Sputtering is a powerful tool due to the large number of variables that can be tuned within a process. With the AJA sputtering system, there are several parameters that can be varied and in this work, the following parameters are controlled in order to obtain high-quality, ultrathin NbN films.

- *The total sputtering pressure*: This parameter sets the amount of total particles (inert gas + reactive gas) in the chamber to form a plasma during the deposition. Sputtering process occurs mostly at low-pressure ($< 5$ mTorr) and in our experiments this value is varied between 2.0 - 3.0 mTorr during the optimisation. This is enabled by the use of a *magnetron* sputtering system. Indeed, the plasma is localised around the target since the electrons are trapped by the magnetic field present under the target and the ionisation yield increases. It allows us to do the deposition at low-pressures and that is an advantage to obtain high mean-free path ($\lambda$), which is inversely proportional to pressure (P) $\lambda \propto 1/P$. Therefore, the pressure is kept low enough to enhance the $\lambda$ and high enough to ignite and sustain the plasma. The pressure is adjusted automatically by setting a value as a position of the "VAT gate valve" corresponding to the set pressure. The VAT gate valve is located in front of the turbo pump and it is adjusted by *VAT adaptive pressure controller*.

- *The partial pressure of the reactive gas $N_2$*: That determines the stoichiometry
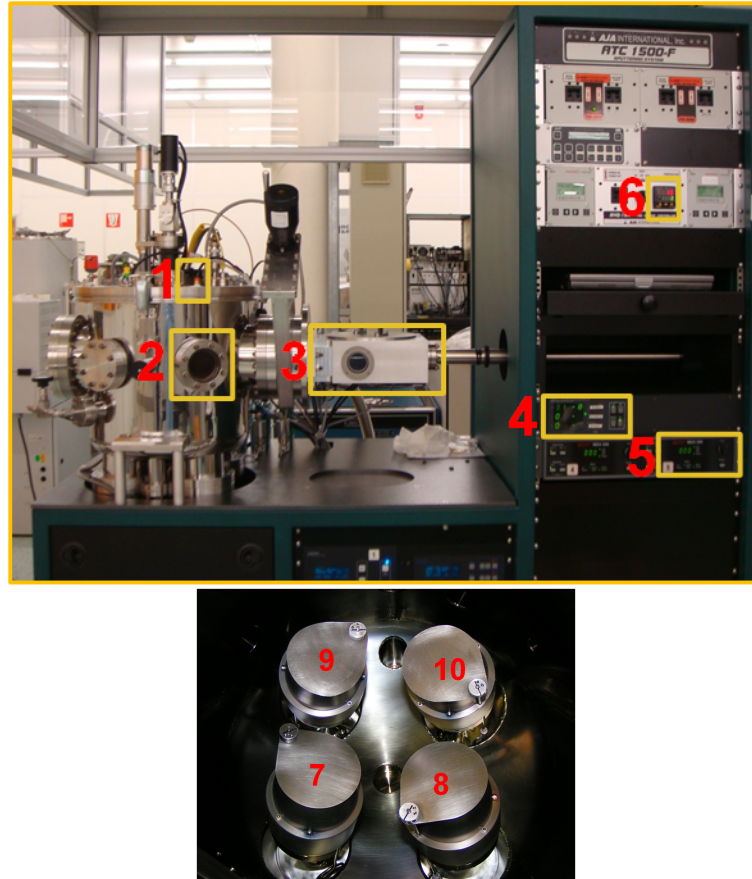
Figure 2.1 – (Top) The picture of the sputtering set-up that is located in the cleanroom of TU/e. On the picture $N_2$ inlet (1), sample view port (2), load-lock chamber (3), vacuum gauge read-out (4), bias unit (5) and the temperature control unit (6) are highlighted with the associated numbers. (Bottom) Inside the vacuum chamber, there are four chimneys used for Nb (7), Au (8), Ti (9) and Cr (10).

of $Nb_xN_y$: In the sputtering system at the TU/e, the flow is set in unit of sccm (standard cubic centimetres per minute) and can be varied from zero to 20 sccm for $N_2$. During the optimisation, this parameter is scanned between 1.4 - 5.9 sccm, corresponding to 10 - 33 % $N_2$ concentration.

- *Current (voltage) supply*: This is directly related to the energy provided to the positively charged ions which are accelerated and then eject an atom from the target material. The NbN film growth is done under the constant current mode and during the optimisation process the value is swept between 250-300 mA.

- *The distance between the target and the substrate*: The distance between the target and the substrate is mostly shorter for a sputter system than for the other vacuum
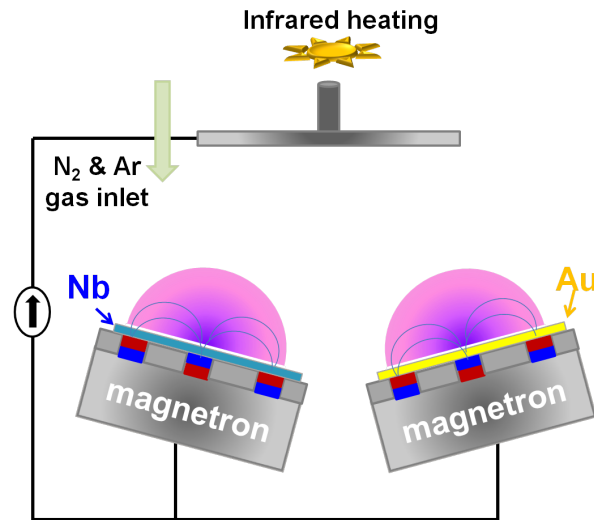
Figure 2.2 – The cold-sketch of sputtering system, showing only the two targets (Nb (7) and Au (8)).

systems. The most important reason is to eliminate the number of intermediate scatterings/collisions the ejected atom might experience during the time of flight. This is set to about 6 cm during the deposition.

- *The angle of the target accompanied by the rotation of the sample holder*: These parameters are adjusted in order to obtain a uniform film thickness on the samples grown within the same batch. The angle also plays a role to convey the momentum of ions to the atom which is the highest at a right angle. As there are four targets in the system, there is a certain angle introduced to the NbN target. Thus, the sample views the target at a non-zero angle (see the sketch in Figure 2.2). The rotation can be increased up to 24 rotations per minute (rot/min) and it is set to 14 rot/min in the experiments.

- *The substrate temperature*: The temperature determines the particle dynamics at the substrate surface. At low temperatures, the mobility of the adatoms is small which may create a thickness variation along the surface. While at higher temperature the mobility is increased, the problem of arsenic evaporation from the substrate starts (see Figure 3.7). The nominal temperature can be tuned from room temperature up to 800 °C. The value is read using a thermocouple located between the two infrared-lamps, located at the back side of the substrate holder. Therefore, it is expected that the temperature is lower on the sample holder and surface than the reported values. This parameter is varied between 300-600 °C but the optimised nominal temperature is in the range of 410 - 475 °C with a deviation related to the differences among the installed lamps. After the installation of the new infrared lamps, the deposition temperature is tuned by a set of AFM measurements.

- *The deposition time*: The deposition time is determined by spectroscopic ellipsometer as explained later in this chapter and a growth rate of about 0.6 Å/s is estimated under the optimised conditions.

All these variables can be modified to optimise the desired film stoichiometry and the quality of the film. While having so many parameters brings a flexibility, it might complicate the optimisation. For example when the reactive gas concentration is changed, the growth rate changes, too and the thickness needs to be optimised in order to study the real change due to the modified parameter and not to the thickness. That requires to optimise the time of the deposition for the new concentration. In addition, it is crucial to keep track of the erosion of the target deposited[95]. It is known that when the target is eroded, the effective applied power applied on the target changes and therefore the energy and the dynamics of the ejected Nb atoms do. That degrades the quality of the film. In order to avoid that, the target is operated within a voltage range of 345-360 V. The targets are ordered either from *AJA Intern., INC.* or from *Kurt Lesker*, with a dimension of 2 x 0.250-inch$^2$ and purity of 99.95 %.

## Conditioning the chamber

Chamber conditioning is done in two steps: 1- gold (Au) deposition and 2- titanium (Ti) deposition. While the former is done only after the deposition chamber is exposed to the atmospheric pressure, the latter takes place before every deposition run in order to improve the vacuum condition and therefore the material quality.

In general, high vacuum systems are built with certain equipments that prevent the adhesion of the water $H_2O$ molecules in the vacuum (deposition) chamber. For example: when the pressure is broken, hot water flows through the vacuum walls, which decreases the adsorption of the $H_2O$ molecules on the walls of the deposition chamber. This is essential because every monolayer on the wall takes longer to pump since the bonding energy between $H_2O$ molecule and the metal (deposition chamber) is large[96]. In addition, once the chamber is closed and pumped down, hot-dry air or $N_2$ are the most common gasses used to improve the base pressure. These techniques are not easily realisable in our setup. Therefore, other techniques are implemented to *clean* the deposition chamber. Therefore, a deposition run of Au is made into the chamber. The idea is to deposit the metal such as Au to stick the $H_2O$ molecules to the wall and to cover the chamber with Au. As a complementary cleaning technique, a titanium (Ti) deposition cycle is used prior to each real deposition run to decrease the base pressure temporarily below $1\times10^{-8}$. Titanium is well known for interacting with the gasses and form a stable product, therefore used in titanium sublimation pump (TSP) for ultra-high vacuum systems[97]. By depositing Ti prior to the real deposition run, the same effect as in TSP is realised. It is believed that temporarily the system is conditioned by decreasing the concentration of the $H_2O$ molecules present in the chamber. It is temporary because Ti is consumed and becomes not functional any more due to the following deposition run and a constant out-gassing within the chamber. It has been observed that if Ti is deposited in the chamber and the vacuum is decreased one order of magnitude, the critical temperature ($T_c$) of unprocessed film is increased by more than 1 K. For the same film thickness, if the Ti deposition run is performed on the sample holder (Inconel type) as well, the film $T_c$ increases by another
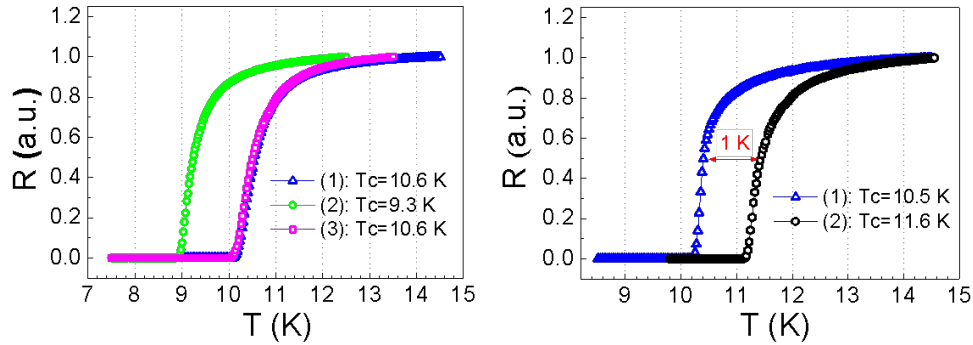
Figure 2.3 – The graphs show the resistance (normalised) of the films as a function of tempera-ture. (Left) The plot demonstrates how the different chamber conditionings affect the film quality. (1, blue triangle) is the deposition right after 12 min. of Ti cycle, (2, green circle) is w/o Ti pre-deposition and (3, magenta square) w/ 12 min. Ti deposition in order to check the reproducibility. (Right) The graph shows (1, blue triangle) the deposition run after Ti is deposited into the deposition chamber prior to the NbN run and (2, black circle) after Ti deposition is done also on the sample holder.

1 K. This indicates the importance of the base pressure and even of the contaminant concentration for a high-quality NbN film growth. This argument is given in Figure 2.3 (also in subsection 3.2.2) and it is clearly seen that Ti deposition improves the film quality as reflected by the increase in $T_c$ by $> 2$ K. This will be discussed further in detail in subsection 2.1.2.

It has to be noted that, the surface of the deposition holder needs to be cleaned time to time due to the indium remnants[2]. As the surface cleaning is done mechanically outside the cleanroom, the holder is at first cleaned with standard 2 minutes/each acetone and isoproponal treatment in ultrasonic bath and then dried with $N_2$. Then, it is always baked over the growth temperature ($>450$ °C) in order to assure the cleanness of the holder and evaporate the water molecules. First the temperature is set to, $T_1 = 100$ °C and kept for half an hour in order to evaporate water molecules. Secondly, it ramps up to $T_2 = 250$ °C and stays for forty-five minutes. The last step is to increase the temperature over the growth temperature, $T_3 = 500$ °C for another forty-five minutes. During all the procedure, there is a Ar flow introduced into the chamber ($P_{Ar} = 15$ sccm). Then the holder is cooled down to room temperature before taking it out.

## 2.1.2 Characterisation of superconducting ultrathin films

In order to evaluate the superconducting, ultrathin NbN films, they are characterised by several techniques. To this aim, the very first and continuous characterisations start

---

[2]Indium is used to mount the samples on the deposition holder.

with measuring the temperature dependent resistance behaviours, from which the critical temperature of a superconducting thin film, $T_c$ and the transition width, $\triangle T_c$ as well as the resistivity of the films are extracted. The R(T) measurement[3] is a very practical and easy way to obtain a relatively fast feedback on the films. Atomic force microscope (AFM) is another technique that is heavily used during the study to characterise the surface roughness of the films as the roughness has a substantial influence on ultrathin film quality. The film thickness of every grown batches/films is determined by using spectroscopic ellipsometer (SE) from *J. A. Woollam Co. Inc.*, M2000D working in a spectral range from 200 nm up to 1000 nm. The initial work has been established with the help of Mr. J.-W. Weber from the PMP group at the TU/e. In order to determine the crystallography and independently confirm the thickness value measured by SE, few films are analysed with high-resolution cross-sectional transmission electron microscopy (HR-XTEM). The samples are prepared by Dr. B. B. Campo at the TU/e and measured by Dr. M. A. Verheijen in MiPlaza. Owing to the good agreement between the two measurements, the film thickness of every sample/film could be measured by SE directly after the growth without relying only on the *growth time*. This is an important tool because during the optimisation several parameters are varied and most of them change the growth rate, and the thickness of the films. However, SE provides an immediate feedback and the time is varied to obtain the right thickness for a proper comparison.

## Electrical characterisation

The superconducting properties of the films are measured to compare the different batches grown with different growth parameters. A cryogenic dipstick is used to measure the resistances of the films as a function of temperature (R(T) measurement). From that measurement, three parameters that are the critical temperature ($T_c$) and the corresponding transition temperature ($\triangle T_c$) of the superconducting film can be extracted as well as the residual resistivity ratio (RRR). All these parameters are extrapolated from a single R(T) measurement and each measurement takes maximum about 3 hours. The setup is given schematically in Figure 2.4. There are a bias source from *Yokogawa* 7651, a multimeter from *Keithley* 2010 and a temperature controller from *LakeShore* 330 to take the measurements. The measurements are computer-controlled with a home-written LabVIEW program. It measures the resistance by driving the temperature controller between a certain initial and final values with a step size of 25 mK (all defined by the user). The temperature is measured with a *LakeShore DT-670* diode and changed by a thin-film resistance with a feedback loop. Both the diode and the resistance are located in the sample holder right under the sample stage.

In one cooling down, it is possible to put two samples in the sample holder, located at the bottom of the dipstick (Figure 2.4). The dimension of each sample is about 0.4x0.8 cm$^2$ and they share the common ground with the dipstick. More information on the dipstick and the sample mounting can be found in Ref.[98]. Furthermore, the parameters $T_c$ and $\triangle T_c$ are determined using the average and the difference of the temperatures corresponding to 80 % and 20 % of the average normal resistance derived following the

---

[3]The resistance versus temperature measurement will be referred to as *R(T) measurement* in the rest of the thesis.
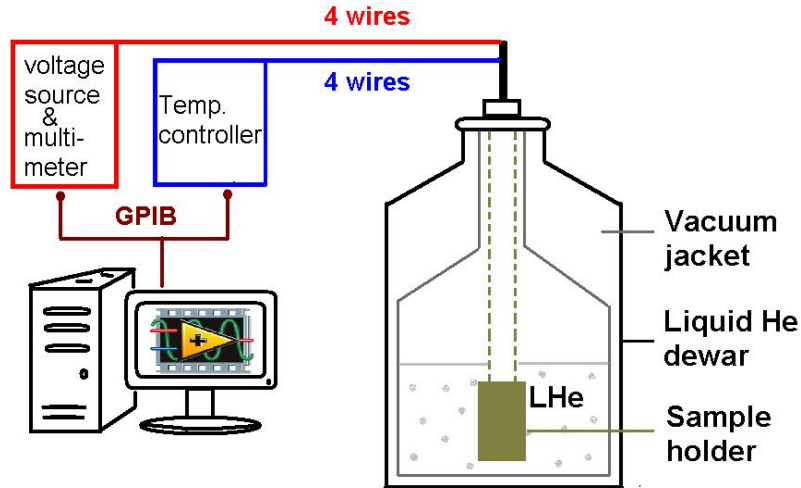
Figure 2.4 – Scheme of the set-up for the R(T) measurements. The temperature controller is the Lake Shore 320, the bias source is the Yokogawa 7651 and the multimeter is the Keithley 2010. The measurements are performed with a Labview 8.5 code.

procedure in[98]. Even though this is not a common technique to report the $T_c$, it is a convenient way to compare the results within the different batches. Lastly, RRR is the ratio of room temperature resistance to the resistance at 20 K, RRR $= R_{300}/R_{20}$. For the optimised parameters, the values obtained are $T_c = 10 - 11.5$ K, $\Delta T_c = 0.45 - 0.65$ K and RRR $= 0.74 - 0.88$ for 4.5 - 6 nm thick films.

## Surface analyses

AFM measurements are performed in this work to study the roughness of the surface both before and after the growth of NbN films. As the films are ultrathin (only a few nm thick), the roughness plays an important role in the quality of the superconducting NbN film. It has been observed both in this study and in Ref.[72] that when the growth temperature is increased, the roughness of the film increases. That is assigned to the arsenic (As) evaporation above 350 °C[99]. Even though the $T_c$ still increases above the critical growth temperature ($\sim 350°C$), at a point the roughness deteriorates the crystal quality and reverses that effect. Figure 2.5 discusses the effect of the growth temperature when it rises from 350 °C (b) to 400 °C (b), the roughness increases and that decreases the $T_c$ and increases $\Delta T_c$ (c).

To the aim of obtaining a *good* roughness along with high $T_c$ and low $\Delta T_c$, the nominal growth temperature is reduced to a value where the roughness is comparable to the value measured on GaAs before the deposition while the $T_c$ is still high. The roughness is defined in root-mean-square (RMS) and the best RMS values obtained in this study is reported in the range of 0.25-0.4 nm.
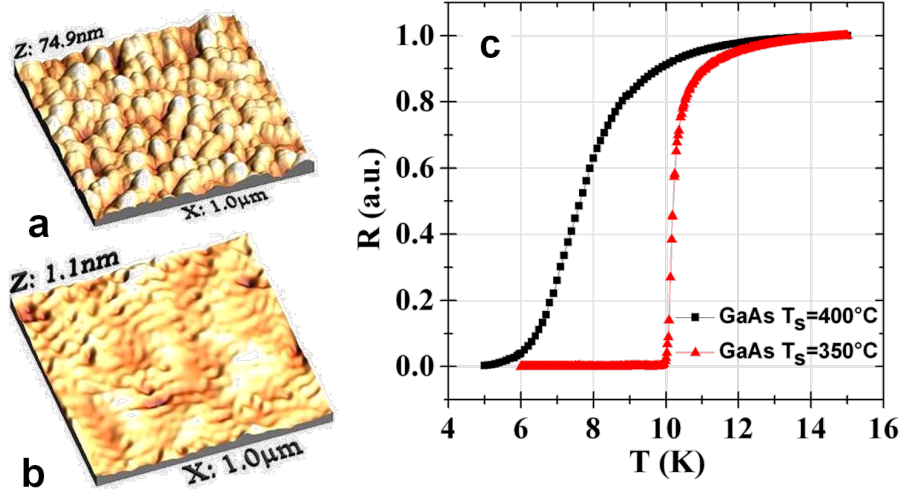
Figure 2.5 – The figure depicts the relation between the surface roughness and the film quality. The films grown with a substrate temperature of (a) 400 °C have an rms rougness of > 10 nm while that decreases dramatically < 0.2 nm at (b) 350 °C. (c) There is a significant change for $T_c$ and $\Delta T_c$ for the rough and smooth surface from Ref.[72].

## Thickness measurements

Thickness measurements are performed ex-situ with spectroscopic ellipsometry (SE) from *J. A. Woollam Co. Inc.* right after the deposition. SE is a non-destructive technique and operates in a spectral range of 200-1000 nm. The software, *CompleteEASE*, is interfaced for data acquisition and analysis. The SE is a very accurate technique as it measures the changes in the polarisation of light state after the reflection from a film or a multilayer. The thickness accuracies below the wavelength of the probing light, down to few atomic layers are easily obtained. In SE, the sample is purely defined by the complex reflectance ratio ($\rho$) which is the ratio between the field reflection coefficient for light polarised parallel ($E_p$) and perpendicular ($E_s$) to the plane of incidence as shown in eqn.2.1 for a single material interface. Figure 2.6 depicts the working principle of SE. The light source is polarised (polariser) and reflected at a certain angle which is close to the Brewster angle and then arrives to the detector (after passing through an analyser), carrying the fingerprints of the reflected surface by phase shift and change in the polarisation. Then, $\rho$ can be rewritten in terms of $\Psi$ and $\Delta$, where $\Psi$ is defined as the angle introduced between two polarisation directions of the light (eqn.2.2) and $\Delta$ is as the phase shift between them (eqn.2.3), as shown in Figure 2.6.

$$\rho = \frac{E_p^{out}/E_p^{in}}{E_s^{out}/E_s^{in}} = \frac{\tilde{R}_p}{\tilde{R}_s} = \frac{|R_p|}{|R_s|}e^{i(\Delta_p - \Delta_s)} \tag{2.1}$$

where,

$$\tan(\Psi) = \frac{|R_p|}{|R_s|} \tag{2.2}$$

$$\Delta = \delta_p - \delta_s \tag{2.3}$$

$R_p$ and $R_s$ are the field reflection coefficients, and $\delta_p$ and $\delta_s$ are the phase changes introduced at the reflection for parallel and perpendicular polarisations of light, respectively.

The measurements are taken around the Brewster angle for the highest accuracy since the difference between the p- and the s-polarised light is the highest. These two parameters, $\Psi$ and $\Delta$, are measured by ellipsometry and used to determine not only the thickness and the refractive indices of the samples but also some other properties such as surface roughness, composition, crystallinity, uniformity, etc.

The light-sample interaction at the interfaces gives an infinite series for the reflection (due to multiple reflection) and for a two-layer system that is a function of the thickness given by the relation for the total reflection $R_{tot} \propto e^{-i\beta}$ where $\beta$ is a function of thickness and defined as,

$$\beta = 4\pi\left(\frac{d_{NbN}}{\lambda}\right)n_{NbN}\cos\theta \tag{2.4}$$

where $d_{NbN}$ is the thickness of the film layer (NbN), $n_{NbN}$ is the refractive index of NbN, $\lambda$ is the measurement wavelength and $\theta$ is the incident angle (see Figure 2.6).

In order to maximise the accuracy of the measurements, the single-side polished GaAs substrate is measured with SE before the characterisation of the NbN layer and data is fit based on the GaAs substrate described in the library. Then, a purely mathematical technique, which is called Basis-spline (B-spline), is used in order to model the thin metal layer (NbN) on top of the semiconductor substrate (GaAs). B-spline is a powerful fitting technique of the layer without requiring any prior knowledge of the layer in interest. It can also be utilised for absorbing and semi-absorbing layers as well as the dielectric layers[100]. Even though, the fitting technique is purely mathematical, it provides the physical parameters such as the thickness, refractive indices and if needed also the surface roughness, composition, optical resistivity etc. of the layer material.

Another technique to measure the thickness and to test SE results is cross-section high-resolution transmission electron microscopy (HR-XTEM). This is a supplementary technique rather than being a regular basis one like SE. The reason is that the sample preparation for HR-XTEM is very demanding and takes much longer compared to the SE analysis. The sample being investigated is thinned from half mm down below 100 nm by focus-ion-beam (FIB) technique and that takes hours before the sample is ready. Therefore, this technique is only used to confirm the results from the previous technique and also to learn about the interface and the crystallinity of the films.

## 2.1.3 Processing of single NbN wires

After optimising the films, some simple NbN nanowire structures (the results will be presented in chapter 3) are fabricated in TU/e in order to gain an understanding of the electro-optical response correlated with different growth parameters. Thus, the films are
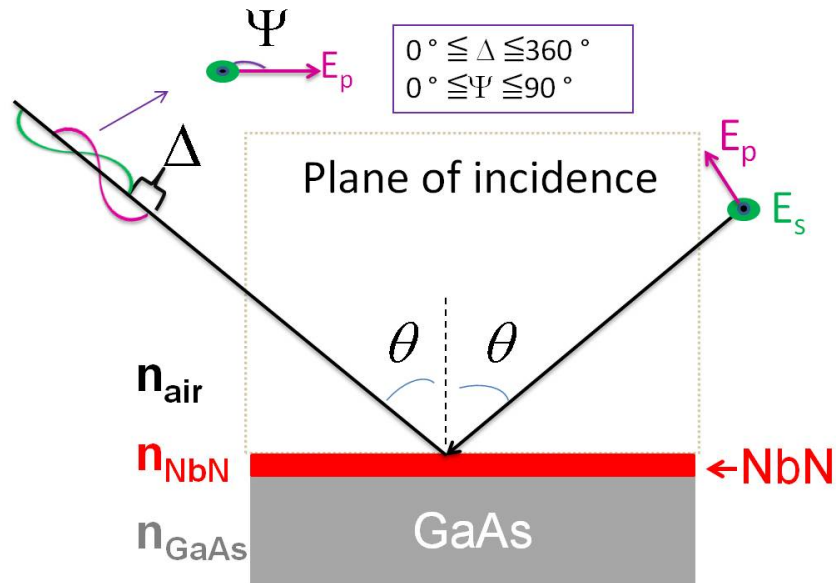
Figure 2.6 – Working principle of spectroscopic ellipsometer. Light is sent through a polariser and after reflection goes through an analyser and arrives to the detector. $\Psi$ is the angle and $\Delta$ is the phase shift between two polarisation mode of the light, and $\theta$ is the angle of incidence.

nanostructured into nanowires using lithography techniques. An optical lithography (*Karl Süss Microtech*, MA6) and an e-beam metal evaporator (*Temescal FC-200*) are used to define the contact pads and a *Raith150$^{TWO}$*- Direct Write electron-beam lithography is employed to define the nanowires. The aim is to investigate a range of deposition parameters in order to increase the understanding on the constrictions, efficiency and the yield.

The wires as shown in Figure 2.8 are patterned by the successive processing steps of optical and electron-beam lithography. The processes are briefly explained in the following but more detail can be found on the lithography systems in Ref.[101]. Here, the processing is explained over the single nanowires as they are processed at the TU/e. The processing of the waveguide detectors are done in CNR, Rome by Dr. A. Gaggero with the similar processing techniques, therefore they are discussed in the related chapters separately.

Optical Lithography:

Optical lithography in this work is utilised for the fabrication of the contact pads of the wires, as they are relatively large (smallest structure is 2x10 $\mu m^2$) and are not changed from one design to the other. Optical lithography is not as a flexible technique since it is based on the transfer of the design from a pre-defined mask. The mask is designed with graphics database system (GDS) compatible software and written on quartz with chromium (Cr) in TU Delft. Two different layout are designed on a single mask. While
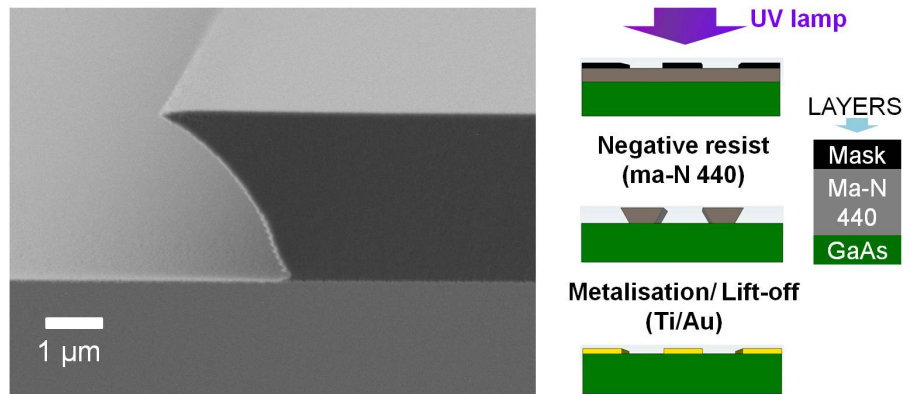
Figure 2.7 – (Left) A cross-section SEM micrograph of the resist profile after the developing step. The resist thickness is 2 $\mu$m. (Right) Processing flow in optical lithography for a negative tone photoresist, followed by metallization and lift-off. Layers are shown at the side with a colour-coded layer structure.

one allows both wiring and probe contacting, the other one is only suitable for contacting with the probe. The latter one is used to maximize the device density by decreasing the contact pad size when the wiring is not necessary. Ultra-violet (UV) light is used to transfer the pattern. The resolution of this mask aligner can only go down to 0.6 $\mu$m with a proper selection of photo-sensitive polymer.

The samples are coated with a negative photoresist, ma-N 440 from *Micro Resist Tech.* on GaAs substrate with a spinning rate of 5000 rotation per minute (rpm) and an acceleration of 5000 m/s$^2$ for 30 s using the *Karl Süss RC 8* spinner. Then, samples are soft baked on a hot plate at 95 °C for 5 minutes and the resist is exposed with the mask aligner. While the exposure time may vary depending on the lamp power, during this work with the lamp power of 9 mWatt/cm$^2$, the exposure time is kept as 100 min. After the illumination, the samples are post-baked (a hard baking step) at 115 °C for 2 min and 30 s. Then, the photoresist is developed using an organic solvent, called ma-D 332s. The most critical dimension in the design belongs to the alignment marks (required for the next lithography step for realigning) and it is 2 $\mu$m.

In Figure 2.7 (left), a scanning electron microscope (SEM) image of the cross section profile after the developing of photoresist is given. The negative slope with a thickness of 2 $\mu$m provides a good profile for the alignment marks and the contact pads.

Metal Evaporator:

After the resist is developed, contact metal layers of Ti/Au (14 nm/ 140 nm) are deposited by electron-beam (e-beam) evaporation. An e-beam evaporator operates at high vacuum levels. typically around $10^{-7}$ mbar. The electrons that are ejected from the filament are directed on the ingot (Ti or Au in this work) in a well-defined trajectory with a 10 kV acceleration voltage and the deposition starts when the metal starts to evaporate. The

metal layer is deposited on the sample by precipitation of the sublimated material.

The metals, Ti and Au, are deposited on GaAs on a lithographically-patterned structure. Besides creating the contact pads of the devices, alignment marks are also fabricated in this step. 10 nm of Ti is deposited before a 150 nm-thick Au layer in order to have a better stiction between GaAs and Au.

This step is followed by a lift-off. The sample is preferably kept for at least 1 hour in the acetone vapour, which diffuses in the optical resist and creates some cracks. Then, it is neatly located in a holder which keeps the sample upside down in the acetone. This is a simple but an important step in the processing flow that eliminates the back sticking of the Au particles that come off. The process flow starting with optical lithography till metallization is depicted in Figure 2.7 (right).

### Electron-beam Lithography (EBL):

The wires with a dimension beyond the resolution of the optical lithography are written by an EBL with an acceleration voltage of 20 kV. As compared to optical lithography, EBL is slower as each structure is defined into the squares of 100x100 $\mu m^2$ (called write field and determines the deflection area of the beam) sequentially but for the same reason, it is a very flexible technique. The design can be modified easily.

In order to pattern the wires (detectors) with a high resolution, a negative-tone aqueous resist, hydrogen silsesquioxane (HSQ) XR-1541-006 resin in a carrier solvent of methylisobutylketone (MIBK) from *DOW CORNING* has been used for the wires with 90 - 400 nm width. The HSQ is spinned on the sample using *Convac ST 146* with 2000 rpm for 60 s and the spinning is followed by a baking step at 150 °C and 220 °C for 2 min/each. That gives a thickness of HSQ about 130 nm. Right before exposing the sample with EBL, a very thin layer of Au ($\sim$ 5-8 nm) is deposited with thin film evaporator *Edwards Auto 306, FL400* at the bottom edge of the sample. Since HSQ is a non-conducting material, that is expected to decrease the charging effect and therefore help to shorten the time required for focusing the beam as well as helping to improve the beam shape. The wires are designed and written in the centre of each write field by automatically realigning with the alignment marks defined by optical lithography (see dotted circles in Figure 2.8(right)). Finally, the sample is developed in a KOH-based inorganic developer (*AZ* 400K), diluted in water $H_2$):AZ-400K (4:1) for 1 min and 15 seconds at 60 °C. It is important to stir the solution while warming up and during the developing to have a uniform solution and etching rate.

All uncovered material is finally removed by fluorine based ($CHF_3+SF_6+Ar$) reactive-ion etching (RIE) in Rome by Dr. A. Gaggero. In Figure 2.8 the sketch (left) and an SEM (right) of the fabricated nanowires are shown.

## 2.2 Electro-optical characterisation of the devices

The results obtained and presented in the rest of the chapters are measured mainly in two different cryogenic probe setups. They are referred as micro-manipulated probe station ($\mu$-PS) and waveguide probe station (w-PS). They are both micro-manipulated and con-
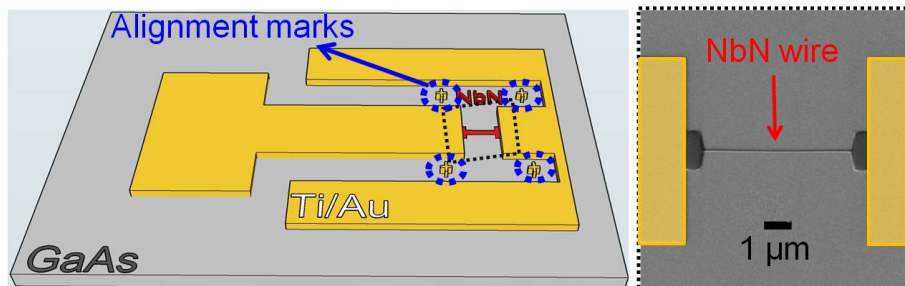
Figure 2.8 – (Left) The sketch of the final look of a patterned wire on GaAs substrate. The wire is 17 $\mu$m-long and the width varies between 80 - 400 nm. The contact pad is deposited by a successive optical lithography and e-beam metal evaporation (10 nm Ti and 150 nm Au) steps. The black dash line shows the region where the SEM image (right) is taken and the alignment marks used for electron-beam lithography are shown with dashed blue circles. (Right) A scanning electron microscope (SEM) image of 80 nm-wide nanowire fabricated on GaAs substrate. The scale bar is 1 $\mu$m and the contact pads are coloured for clarification.

tinuous He- flow cryostat. The $\mu$-PS is utilised mainly for free-space coupling experiments such as the measurements of simple nanowire structures. Besides, the setup is used for fast characterisation and pre-check of the waveguide detectors since it allows mounting a larger-size sample (with tens or hundreds of devices). On the other hand, the w-PS is designed specifically for waveguide coupled systems with all the manipulations mounted in the cryostat.

## 2.2.1 Micro-manipulated probe station

The experiments reported in chapter 3 are conducted in micro-manipulated probe station ($\mu$-PS) from *Janis Research Co. Inc.* (ST-500) with some modifications done by Dr. David Bitauld. Figure 2.9 shows a schematic of the setup. The cryostat has an inlet that hosts two smaller tubes inside. One of them is the vacuum line that provides a system vacuum through a turbo-molecular pump. The other one is for the transfer line required to cool the sample by a continuous flow of liquid helium (L-He). The transfer line has an adjustable flow-control needle in order to regulate the L-He flow. This setup reaches a base temperature of $\sim$4-5 K, measured at the sample mount.

The $\mu$-PS allows mounting the samples up to 1x1 cm$^2$ on a removable sample holder. Therefore, this setup is very convenient to test a whole chip (in a suitable size) in one cooling down. It is quite critical to keep the whole sample at a temperature as close to as possible to the base temperature read on the sensor. Therefore a high thermally conducting varnish from *LakeShore* (VGE-7031) and copper clamps are exploited for the sample mounting. The application of the varnish is very critical since the thermalisation to the sample holder is mostly provided through the varnish. Thus, the varnish is evenly distributed on the mounting holder and the sample is gently rotated in small degrees and pressed on the sample holder in order to avoid any air gap that can play a role as
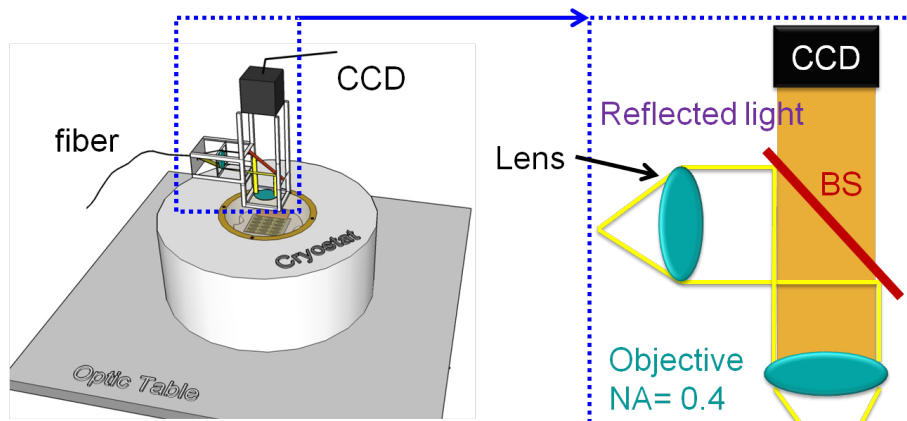
Figure 2.9 – Schematic of the $\mu$-probe station. The sample size is allowed up to 1x1 cm$^2$ in this cryogenic setup. Light is coupled from an single-mode fiber and the optical arm includes a lens, a beamsplitter (BS) and an objective (NA=0.4). The light that couples to the sample is indicated by yellow lines and the reflected light detected by the CCD camera is by dark yellow lines.

an insulating layer. Based on the size of the sample, two copper clamps can aid for a good thermal contact with a careful mounting. It is important not to press too strong on the sample holder, to avoid either breaking the sample or lifting the other side of the piece (most critical for the mountings with one copper clamp). It is also important that the holder is flat on either side. If there are some scratches, the surface can be improved using polishing papers with very fine grading. With a careful mounting and a good cooling down, it is possible that the base temperature reaches down to $\sim$4.2 K[4].

The devices are contacted with a 50 $\Omega$, 40 GHz microwave probe ($\mu$m-probe) from *GGD Industries, Inc.*, which is configured with a ground-signal-ground (GSG) configuration, each with a spacing of 100 $\mu$m (not shown in the figure). The probes are translated with micro-manipulated independent X, Y, Z translation stages and they have a travelling range of a few centimeters. While micro-manipulation with a larger range of translation is advantageous, the room-temperature control of the $\mu$-probe introduces some heat-transfer to the setup. Thus, even though it is possible to mount two probes for this system, for the temperature concern only one is assembled.

The cryostat has an optical window (at 300K) and a cold filter (at 25K) for a free-space coupling. The optical window is needed both for observing the sample (purple line in Figure 2.9) and coupling the light on the devices (yellow lines in Figure 2.9) and cold filter allows only the visible and near infrared range of the spectrum and eliminates the far-infrared portion of the blackbody radiation. The optics is mounted on the computer-controlled *Thorlabs* X, Y, Z translational stages, each controlled with *TDC-001* motion controllers. The stage carries a lens at the fiber coupling arm to collimate the beam from the fiber, a beamsplitter to reflect the infrared light and transmit the visible light (90:10

---

[4]That has been verified by checking the samples in liquid helium using a dipstick.

ratio) and a reflective objective with a high numerical aperture of NA= 0.4 (with a 24 mm working distance) to focus the light on the device. The reflective objective can focus the light into a spot size of ~1 $\mu$m (FWHM) at 1300 nm[1025]. The reflected light from the sample is collected on a charge-coupled devices (CCD) camera for displaying. The camera is also used for a coarse focusing of the probe beam on the device active area. That is performed with a fiber coupled, coherent light source (680 nm) before coupling the near infrared laser source. The laser (1300-1550 nm) is coupled to the optics through a fiber connector.

## 2.2.2 Waveguide probe station (w-PS)

The experiments reported in chapter 4 - chapter 5 and chapter 6 are all conducted in the w-PS. The w-PS was designed by Dr. J. P. Sprengers at the TU/e using a commercial cryostat from *Janis Research Co. Inc.* There are several similarities between the w-PS and the $\mu$-PS (subsection 2.2.1) whilst some characteristic properties of this setup makes it unique. The sample mounting procedure and the free-space coupling optics are the same as for the $\mu$-PS and they will not be repeated here. It is worth to concentrate on the differences in this section.

The main differences are in the contact-making and light coupling into the waveguide, which are detailed in the following. The approach taken in this particular cryogenic setup is that both electrical connections and optical coupling to the waveguide photon detectors are manipulated in-situ. Since there are less interfaces to room temperature (less thermal load), it is possible to reach to a base temperature of ~2 K, and with this base temperature the temperature on the sample is estimated and also confirmed by control measurements to be <4 K.

Figure 2.10 gives a schematic look into the fiber-coupled w-PS. The top image shows the free-space optics (not different from the $\mu$-PS) and a cross-sectional view of the cryostat. Different from the $\mu$-PS is that the probes and the fiber coupling are manipulated by piezos. There are four independent nano-manipulated X, Y, Z piezo stages (ANP(x & z)101/ LT type) from *Atto*cube *systems* with a maximum travelling range of 5 mm. They are mounted on the cold plate and anchored to its temperature. Their manipulation is done by two base positioning controllers (ANC300, *attocube systems*). The configuration is flexible to change according to the design of the chip but at maximum four different movable parts can be hosted in the cryostat. In Figure 2.10 (bottom-left image), as an example a configuration with two $\mu$-probes that are facing to each other (used for the measurements of MMI with detectors and waveguide autocorrelators, chapter 5) and a fiber and a dark-count blocker (DC blocker) on the other two sides is shown. The DC blocker is made of aluminium (Al) and anchored as well to the cold plate temperature to cover the detectors during the measurement. That is employed in order to decrease the dark count rate (DCR) in the system about as discussed at the end of this section. This configuration is changed with a probe and fiber facing each other for waveguide single-photon and photon-number-resolving detector measurements and with two fiber facing each other for transmission measurements through the waveguides.

---

[5]The objective is reflective microspoce objective with high numerical aperture and wide spectral band from *Newport Corporation*.
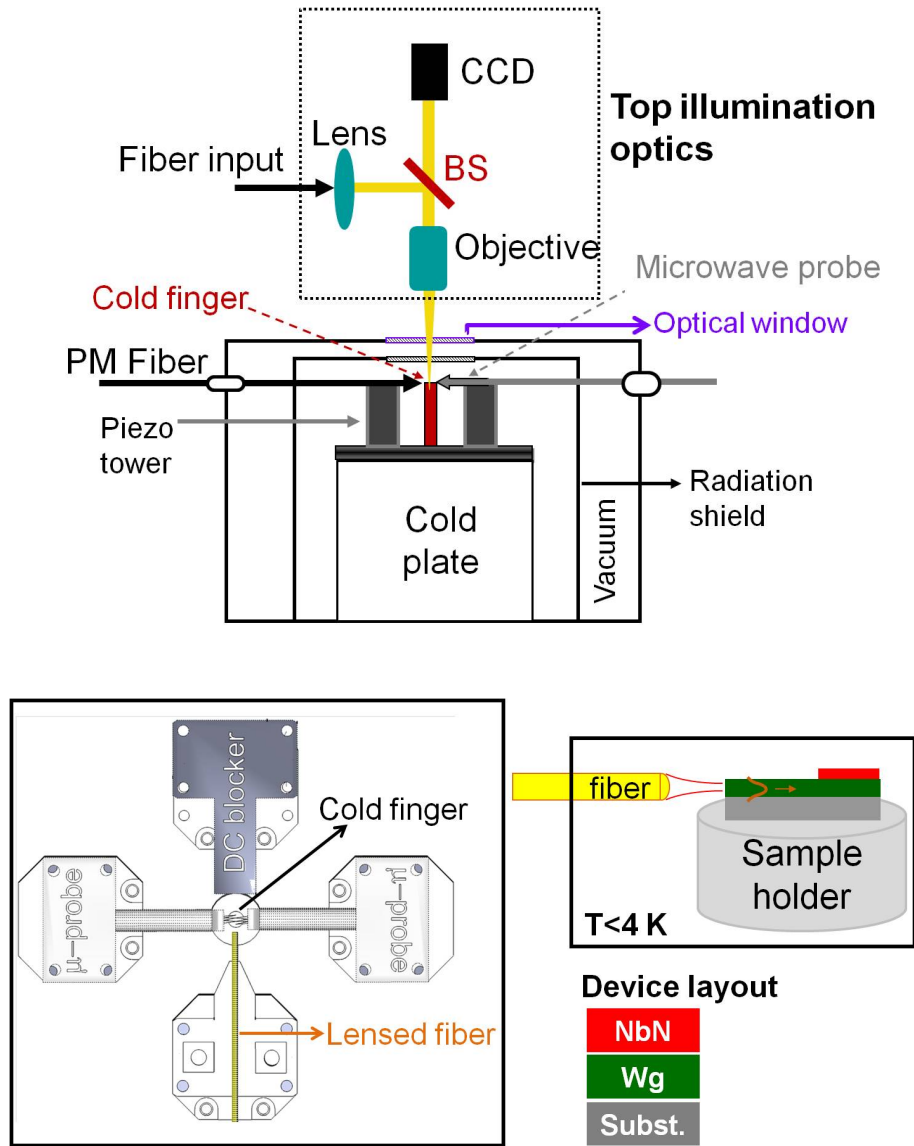
Figure 2.10 – (Top)Schematic of the waveguide probe station setup. (Bottom) On the left, the drawing of the inside of the cryostat. There are four X, Y, Z piezo-stages, two host $\mu$-probes, one holds the lensed fiber and the one opposite to that is used interchangeably but in this figure there is a dark count blocker. On the right side, a blow-up, side-view sketch of the optical coupling from lensed fiber to the waveguide. Light is coupled with a lensed fiber into the waveguides. In this setup, the temperature seen by the devices is <4K. (Subst: substrate and Wg: waveguide)

The bottom, right sketch in Figure 2.10 depicts the light coupling in the w-PS. The sample is mounted on the cold finger (located on top of the cold plate) with a movable sample holder. The sample holder has a size of 4x7 mm$^2$. The reason of this small size is mainly related to the limited travelling range of the piezos. In the present configuration of the setup, two fibers can be mounted. They are lensed fibers from *Oz Optics* with a spot size of 2.5 $\pm$ 0.5 $\mu$m. The fiber is aligned to the waveguide by the nano-manipulated piezo stages. The alignment can be relatively easy. For the detectors, first, coarse alignment is done by coupling a laser with high power (980 nm diode laser, which is visible to the CCD camera) and measuring the I$_c$ of the detectors, which is sensitive to its temperature. The maximum decrease in I$_c$ is observed at the best coupling. However, since the interesting regime is the spectral range around 1300 nm, the fine tuning is done later by coupling a laser diode working at 1310 nm (SR9D-DB9 type from *ThorLabs* driven by TDC 201 ULN 100mA controller). Furthermore, for the transmission measurements again first coarse alignment is done by maximizing the output of a 980 nm diode laser and then fine tuning is done with the interesting wavelength by increasing the output power read in the power meter (*NOVAII OPHIR*), calibrated for near infrared wavelengths.

As has been discussed previously in subsection 1.5.1, the evaluation of the device quantum efficiency is based on the transmission measurements on a waveguide structure with no detectors on top. These measurements are performed in the w-PS. For this aim, the waveguide is cleaved at the two facets (two mirrors), creating a Fabry-Perot (FP) resonator, and leading to interference fringes as the wavelength of the laser is changed. The light is coupled and collected at room temperature using two nominally identical lensed fibers faces to each other. In Figure 2.11 an example of FP fringes is given for a transmittance measurement of a 2 mm-long waveguide with a tunable laser working around 1300 nm (from *Hewlett Packard* 8167A).

The electrical connections of the piezos inside the cryostat are provided by *Atto*cube and the probes are wired by the user by using low resistance and low thermal conducting *LakeShore* miniature coaxial cables (type-C). Finally, all the room temperature and interface cabling is provided by Janis. The room temperature cables are anchored first to the radiation shield and then to the cold plate with bobbins in order to decrease the thermal load to the setup.

The cooling as in the $\mu$-PS is controlled with the adjustable cryogenic flow control needle valve integrated on the transfer line. The valve is rotated for three-quarters as an initial flow setting. After the temperature on the radiation shield reaches below 20 K (there is a temperature sensor integrated), the flow is regulated by decreasing the rotation to two-quarters in few steps. The temperatures both at cold finger and the radiation shield are measured by Si-diodes through a temperature controller, *LakeShore* 331.

The last thing that needs to be mentioned about this cryostat is the DCR. Even though the base temperature read on the temperature controller is ~2 K and the DCR is known to decrease with the temperature (see Figure 1.6 in chapter 1), it is unexpectedly high in the w-PS setup compared to the ones taken with a dipstick. In order to resolve the origin of the problem, an intensive study has been done on the DCR (see Figure 2.12). It is well known that the DCR of superconducting single-photon detectors is very sensitive to any change in temperature or the background radiation in the infrared range of spectrum. The optical window currently available in the setup and the cold filter on the radiation shield
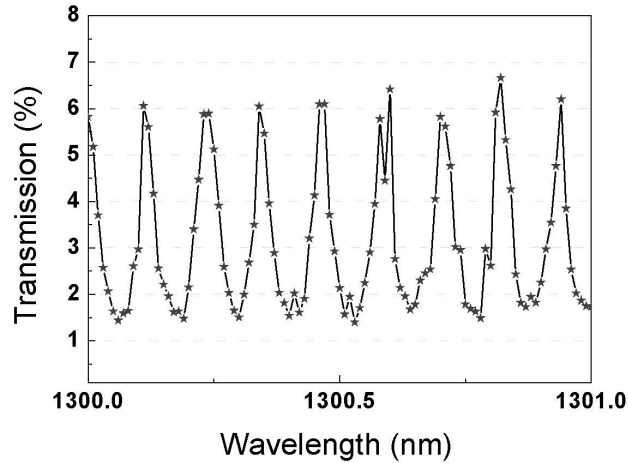
Figure 2.11 – Fabry-perot (FP) fringes measured on a simple 2 mm-long ridge waveguide (with no wires on top).

are transmitting more than 80 % of the incident light in the range of 250 - 3200 nm. Therefore, there is a large part of the room-temperature blackbody radiation transmitted and most likely trapped in the cryostat and that increases the DCR. We are confident to assign that to the blackbody radiation rather than the temperature seen by the detector because according to our study at different temperatures for $I_c$ (see inset in Figure 2.12), we observed that the temperature in the w-PS is about 2 K while the DCR is higher as compared to the case where the temperature is at 4.2 K. Figure 2.12 shows that while in the current configuration of the w-PS a DCR of few hundreds of kHz is observed at $I_b \approx 0.95 I_c$ due to the infrared photons, it can be reduced to few hundreds of Hz at the same bias by a proper shielding as well as lowering the temperature to $\sim$1 K. The 1 K measurements are conducted in another cryostat called VeriCold (with no optical window). For more details on that setup, one may refer to the Ref.[104]). In order to eliminate the DCR by blocking the infrared radiation through the optical window, a "dark count (DC) blocker" (made of aluminium in the TU/e workshop) is mounted on one of the piezo stages (see Figure 2.10) and anchored to the base plate. After the fiber is aligned to the sample, the sample is fully covered by the DC blocker and the DCR is measured. Figure 2.13 shows that there is not a significant improvement. It is believed that after the blackbody radiation enters the setup, most likely it is trapped and reflected by the metal blocker and still enhances the DCR. Thus, the cold filter is planned to be improved as a future perspective.
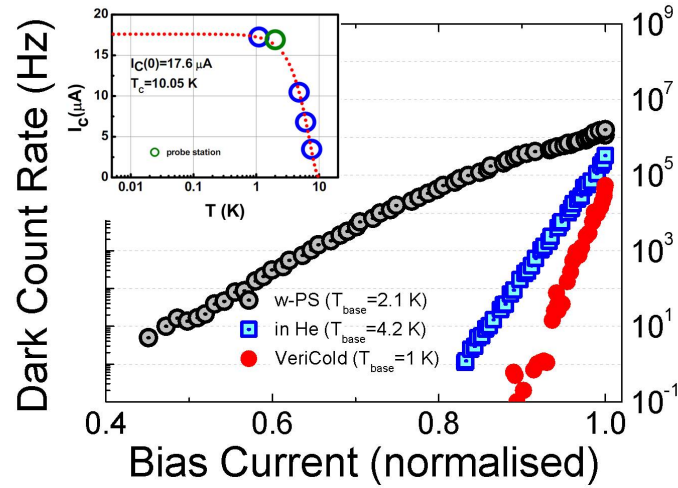
Figure 2.12 – The dark count rate of a waveguide single-photon detector observed in three different setups, w-PS at a base temperature of T= 2.1 K and with an optical window (black circle), LHe dipstick at T= 4.2 K without an optical window (blue squares) and VeriCold at T= 1 K without an optical window (red dots). Inset: The $I_c$ studied at different temperatures in VeriCold during a cooling down and fitted with the formula as a function of T [Ref. [103]]. VeriCold and dipstick measurements are taken by Dr. G. Frucci and Dr. S. Jahanmirinejad, respectively.

## 2.3 Design of waveguide detectors

The devices presented in the chapters 4-6 based on GaAs/AlGaAs ridge waveguides (also called rib waveguides) are designed with an RF module in perpendicular hybrid mode using Comsol Multiphysics (a finite element method). The electromagnetic wave equations are solved using Maxwell equations for the case of no source ($J = 0$) and no free charges ($\rho = 0$) with the refractive indices for the layer materials as given in Table 2.1 for 1300 nm and 1550 nm. A perfect electric conductor is assumed for the boundary conditions.

While a propagating ray theory in a slab waveguide provides an intuitive feeling, the quantitative modelling of waveguide modes can be numerically calculated with the Maxwell equations. In our design, since the waveguide is homogeneous along the propagation axis, the Maxwell equations are solved in 2D. For such a waveguide, there are certain modes allowed to propagate in the waveguide slab and they are called *waveguide modes*. The FEM (finite element method) analysis is used for waveguide detectors to optimise the design and also to gain an understanding on the mode profile. The modal absorption coefficient is calculated using the imaginary part of the effective index [105] by solving for the eigenvalues. In Table 2.1, the refractive indices that are used in the simulations are given for two wavelengths at 1300 nm and 1550 nm.

The detector is simulated for NbN superconducting nanowires on top of a GaAs/
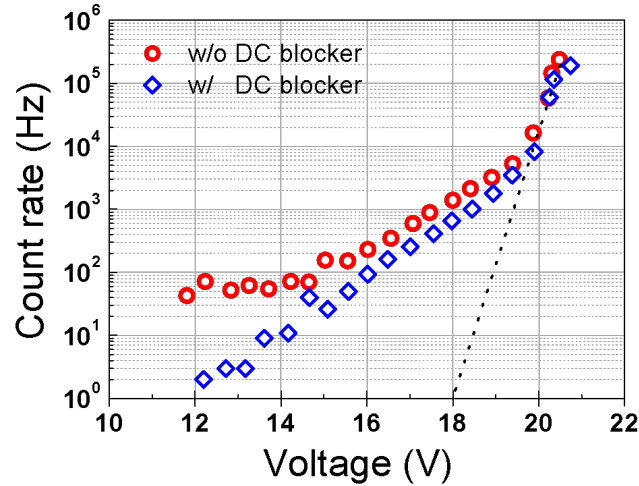
Figure 2.13 – The dark count rate measured on a waveguide single photon detector with (blue diamonds) and without (red circles) DC blocker.

Table 2.1 – Refractive indices used in the simulation given for 1300 nm and 1550 nm.
*The refractive index of NbN at 1550 nm should be slightly higher but in this work it has been considered the same value as at 1300 nm, taken from Ref.[71]

| $\lambda$ | $SiO_2$ | NbN | GaAs | $Al_{0.75}Ga_{0.25}As$ |
|------|-------|-----------|-------|----------------|
| 1300 | 1.547 | 5.23 - 5.82i | 3.386 | 3.039 |
| 1550 | 1.528 | 5.23 - 5.82i* | 3.431 | 3.282 |

$Al_xGa_{1-x}As$ ($0.70 \leq x \leq 0.75$) ridge waveguide. The nanowires on the waveguide sense a different portion of the same mode depending on the location along the horizontal direction. Since a high confined mode profile is employed, it is very likely (and will be discussed later in chapter 6) the absorption decreases towards the edges. A 1.85 - 3.85 $\mu$m-wide and 300 - 350 nm-thick ridge GaAs waveguide etched by between 250 - 300 nm and located on top of a AlGaAs cladding layer is simulated. The thickness of wires varies between 4 nm to 6 nm and they are 100 nm-wide with a spacing of 150 nm. In the simulation, a 100 nm-thick $SiO_x$ layer is considered on top of the NbN nanowires, which is left as a residue of the hydrogen silsesquioxane (HSQ) resist after the patterning (see subsection 2.1.3). For this type of dimensions, the modal absorption coefficients are calculated to be at least as high as 300 cm$^{-1}$. More details are given in each chapter when the design of the device is mentioned.

An example is given in Figure 2.14 simulated at $\lambda$= 1550 nm for four wires on top of a GaAs waveguide. The ridge has a core thickness (t= d + h ) of 0.35 $\mu$m with an etching depth of 0.30 $\mu$m. Moreover, the width is 1.85 $\mu$m and the AlGaAs lower cladding layer is 1.5 $\mu$m. In the figure the mode profiles of the fundamental modes (00) for TE (top) and TM (bottom) are shown.
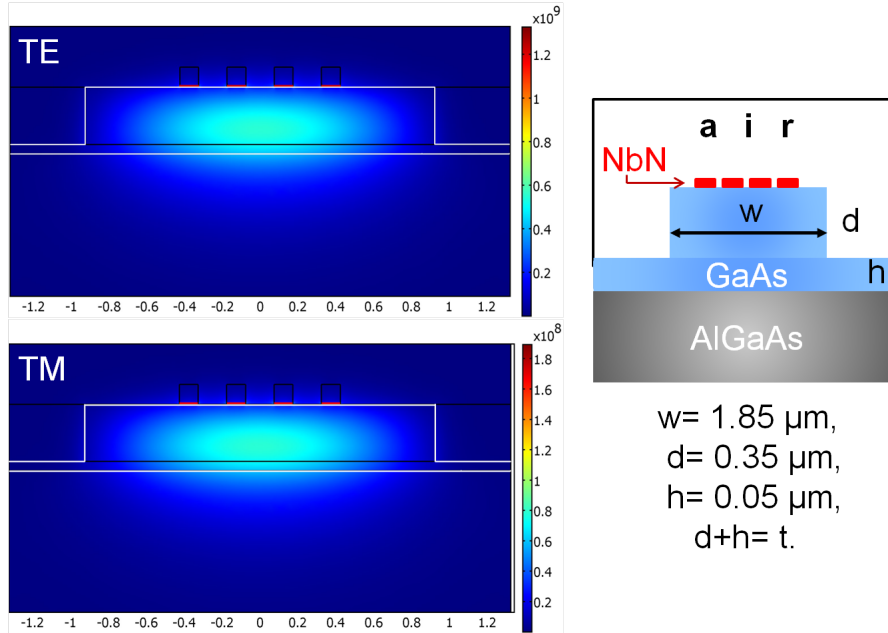
Figure 2.14 – Contour plots of the electric field for the fundamental TE and TM modes of a ridge waveguide for given dimensions (shown on the sketch at the right, not to scale) at $\lambda = 1550$ nm. White lines on the plots show the boundary of GaAs and red lines are for NbN in order to guide the eyes. The scale bars are given separately for TE and TM polarisations. HSQ is not shown on top of NbN in the sketch.

The dimensions of the waveguide are optimised by considering three factors, 1- keeping the width in the order of the spot size to have an efficient coupling of the light from the lensed fiber into the waveguide, 2- leaving some space for the alignment tolerance in patterning the wires on the waveguide and while satisfying the first two requirements 3- having still a high absorption by the nanowires. The optimised dimensions are 0.30x1.85 $\mu$m$^2$ for waveguide single-photon detectors and 0.35x1.85 $\mu$m$^2$ for the waveguide autocorrelators. In Figure 2.15 the calculated absorptance of a waveguide detector with different dimensions are given. As shown, with the optimised dimensions, it is possible to obtain more than 90 % of absorptance for 100 $\mu$m-long waveguide while that decreases down to 60 % for a waveguide with a 0.5 $\mu$m core thickness.
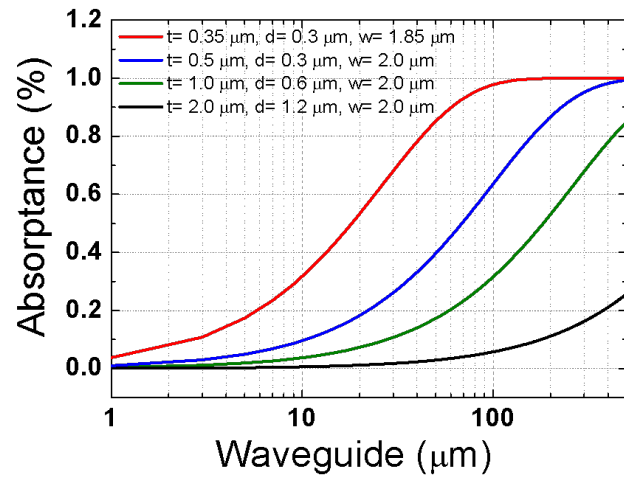
Figure 2.15 – Calculated absorptance of a waveguide detector with four wires at $\lambda = 1550$ nm and TE polarisation (for the fundamental mode) for different dimensions (t is the core thickness, d is the etching depth and w is the width of the waveguide, refer to Figure 2.14 for the sketch).

# Chapter 3

## Study of NbN Superconducting Films on GaAs

### 3.1 Introduction

A very promising way to increase the detection efficiency of the NbN nanowire superconducting single-photon detectors (SSPDs or SNSPDs) is to integrate them with optical structures, such as cavities and optical waveguides in order to increase the absorption. Moreover, integrating them with waveguides allows realisation of a fully-functional quantum photonic integrated circuit as discussed in section 1.2. Traditionally, SSPDs are fabricated on sapphire ($Al_2O_3$)[106] or magnesium oxide (MgO)[107], and recently also on silicon (Si)[108]. The fabrication of microcavities and waveguides is not straightforward in these materials (with the exception of Si) and additionally they are not suited to the realisation of single-photon sources based on spontaneous emission. Sources of correlated photon pairs and heralded single-photon sources have been demonstrated using nonlinear processes in Si waveguides, but filtering of the pump represents a huge challenge for the integration of the sources with the detectors. Thus, a technology transfer is required from the conventional substrates to an optically active material system, such as III-V material system. As already discussed in section 1.2, GaAs is a highly suitable semiconductor for integration as the single photon sources can be obtained within photonic-crystals (PhCs) and low-loss passive circuit elements can be fabricated. Therefore, GaAs is promising for a fully integrated circuit platform.

The technology transfer of SSPD from sapphire and MgO to GaAs is not very straightforward, though[109]. The deposition of NbN films on the usual materials is mostly performed at high growth temperatures ($> 400$ °C)[110]. On the other hand, GaAs is well known to start evaporating above 350 °C[99]. That restricts the working range of the growth in terms of temperature on GaAs.

In the beginning of this thesis work, SSPDs integrated with advanced GaAs/ AlGaAs based optical structures such as distributed Bragg reflectors (DBRs)[72] and optical waveg-

uides[29] have been reported by our group. Those films have been grown in EPFL till October 2009 with the research facility of Dr. R. Sanjines, first by Dr. F. Marsili[109] and later developed further by Dr. A. Gaggero[72]. The initial work with spectroscopic ellipsometer (SE) has been established with the help of Mr. J.-W. Weber from the PMP group and the high-resolution cross-sectional transmission electron microscopy (HR-XTEM) samples are prepared by Dr. B. B. Campo at the TU/e (FNA group) and then measured by Dr. M. A. Verheijen at MiPlaza. In the first half of this work, a lot of effort has been dedicated to transfer the superconducting NbN film technology to the TU/e cleanroom, and to optimise their superconducting properties, as described in this chapter.

In the first part of this chapter the optimisation of the NbN films on GaAs are extensively discussed. In the second part, the fabrication of detector structures on the device-grade films and their opto-electrical characterisation are reported. Lastly, some optical analysis performed by ellipsometry on NbN films on GaAs are presented.

## 3.2 Optimisation of the deposition parameters of ultrathin NbN films on GaAs

There are several reported techniques for the characterisation of NbN films including but not limited to XRD (X-ray diffraction) and RHEED (reflection high energy electron diffraction) techniques. However, most of these techniques are not suitable for a few nanometer thick NbN layer simply due to sensitivity reasons[1].

As explained in subsection 2.1.2, through this study, as a main technique temperature dependent resistance (R(T)) measurements are performed from which critical temperature ($T_c$), transition width ($\triangle T_c$) and residual-resistivity-ratio (RRR) can be extracted. Moreover, atomic-force microscopy (AFM), spectroscopic ellipsometry (SE) and high-resolution cross-sectional transmission electron microscopy (HR-XTEM) are also exploited as complementary techniques to support the data. The $T_c$ is very sensitive to the growth parameters, such as the $N_2$ concentration, temperature and the base pressure. However, by carefully setting the growth parameters, it is feasible to obtain state-of-the-art films. To this aim, several parameters are varied and the results are explained in this section.

Before the optimisation started, one issue that has to be resolved is measuring the thickness as precisely as possible. Therefore, SE is heavily used for the thickness measurements. As it is a non-destructive technique, every samples can be measured to have an information on the thickness of that sample without relying on the growth time. The next issue is conditioning of the deposition chamber. The *cleaner* the deposition chamber is, the *higher* the $T_c$ gets. Then, the amount of the reactive gas ($N_2$) is adjusted by studying the effect on $T_c$. Deposition temperature is another critical variable among the parameters due to arsenic (As) evaporation from the surface. This is studied measuring both $T_c$ by R(T) measurement and the surface roughness by AFM. As the $T_c$ is known to decrease with decreasing thickness[111], this has also been studied in our material system. Lastly, it needs to be mentioned again that due to the change of infrared lamps in the sputtering

---

[1]Some XRD measurements have been performed on our films at the TU/e by Mr. W. Keuning and Mr. P.J. van Veldhoven but no information could be extracted.
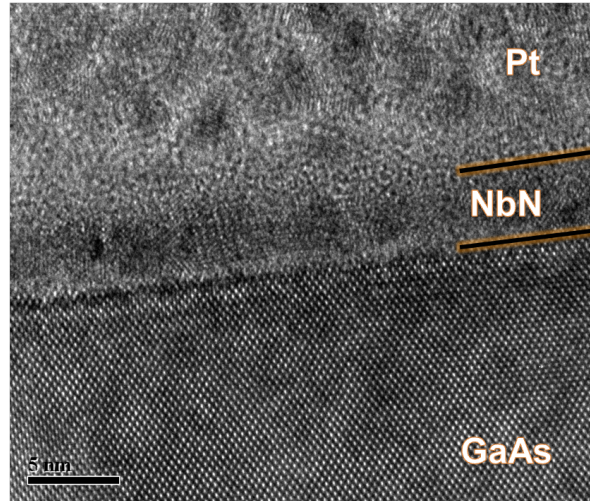
Figure 3.1 – HR-XTEM image of a 4.6 nm-thick NbN film deposited on GaAs. The deposition is done under 30 % $N_2$ flow (before the final optimisation).

system during this work (two times), the optimised nominal deposition temperature has been observed to vary in the 410 - 475 °C range[2]. Thus, each time when the lamps are exchanged, the temperature range is scanned to attain the same result as obtained with the previous lamps and the optimised nominal temperature $T_{growth}^{opt}$ is determined. This value is reported as reference value in the systematic study below, in order to allow a comparison between the results obtained with the different sets of lamps.

### 3.2.1 Thickness calibration

As a non-destructive technique, spectroscopic ellipsometry (SE) has been exploited to have a direct information on the thickness (and optical properties) of NbN films right after the deposition. The thicknesses reported throughout this work have been measured by SE working in the spectral range of 200 - 1000 nm if not stated otherwise. In order to validate and confirm the SE measurements, the HR-XTEM technique has been used. Therefore, two films with t= 4.6 ± 0.1 nm and t= 7.8 ± 0.1 nm thicknesses measured by SE are cross-checked with HR-XTEM and a very good correspondence is found especially for the thinner film. The thickness of the thin film is measured as 4.6 ± 0.2 nm by HR-XTEM whilst the thickness of the thick films is measured as 7.3 ± 0.2 nm. This shows the power of SE for thickness measurements of highly absorbing thin films. Therefore, SE has provided an independent measurement of film thickness of each deposition batch.

Using the ellipsometer, a range of thicknesses is studied in terms of $T_c$. While the bulk NbN has been reported to have a $T_c$ as high as 17 K[52], it drops down to 10 - 12 K for 4-6 nm films[111]. The suppression of superconductivity could be due to the proximity effect which occurs when a superconducting film is in contact with a non-superconducting

---

[2]The temperature sensor is located between the lamps.

film. It was suggested first by Cooper in 1961[112] and has been widely used to explain the decrease in $T_c$[113,114]. Thus, the thickness plays an important role in degradation of $T_c$ as well as the other deposition parameters, i.e. temperature and reactive gas flow and it is essential to know the film thickness upon growing a new batch in order to be able to precisely compare the deposition parameter that has been varied.

The simplified McMillan model suggests a proximity effect in a planar thin-film geometry due to the formation of a interlayer between the superconducting and the normal layers[115] due to the inter-diffusion of the atoms (Ga and/or As in our material system). As a result of that, the density of states is reduced[115] and the decrease in the electron density with the film thickness results in the decrease in $T_c$[116]. Then, the $T_c$ is given by,

$$T_c = T_{c0} \left( \frac{3.5 T_D}{T_{c0} \pi} \right)^{-\frac{\alpha}{d}} \tag{3.1}$$

where $T_{c0}$ is the critical temperature for the bulk film ($T_{c0}$= 15 K), $T_D$= 174 K is the Debye temperature[117], d is the film thickness and $\alpha = d_N N_N(0)/N_S(0)$ where $d_N$ is the thickness of the interlayer and $N_{N,S}(0)$ are the density of states in the normal (N) and the superconducting (S) layers at Fermi level, respectively[115].

Figure 3.2 shows the variation of $T_c$ as a function of the inverse of the thickness for the optimised conditions, fitted by using the relation in eqn. 3.1. The fits of the equation for $\alpha$= 0.55 (red line) and $\alpha$=0.70 (blue line) are plotted on the figure, too. Using $\alpha = 0.63 \pm 0.08$ nm and considering $N_N(0)/N_S(0)$=1, $d_N = \alpha = 0.63 \pm 0.08$ nm is calculated. This value is similar to the values reported for Nb[118].

In the sputtering chamber for the optimised deposition conditions, a growth rate of $\sim$ 0.6 Å/s is extracted. Even though this number is used to estimate the thickness, it is always double checked with SE for the real thickness. It is worth mentioning here that due to the low growth rate, the impurity level is more important in this work as discussed in the following section.

## 3.2.2 Conditioning of the deposition chamber

The conditioning of a deposition system is essential for the homogeneity and the reproducibility of the deposited material. The extreme sensitivity of superconducting materials to impurities requires extreme care in all steps from sample cleaving to the unmounting, including the chamber conditioning as much as deposition parameters. As shown in Figure 3.3 (see also Figure 2.1.1), the conditioning of the chamber by a Ti pre-deposition influences the superconducting film properties with a $T_c$ change as high as 2 K. The effect of the background impurities is so dramatic that an increase in $T_c$ about 1 K is observed even when a Ti pre-deposition cycle carried out on the sample holder prior to the mounting of the sample. This pre-deposition suppresses the degassing from the sample holder. Therefore, every batch starts with a Ti pre-deposition on the sample holder (which also covers the vacuum chamber). That has been one of the important findings in the initial phase of the project, which made it possible to obtain high $T_c$ films at the TU/e by using the existing sputtering system.
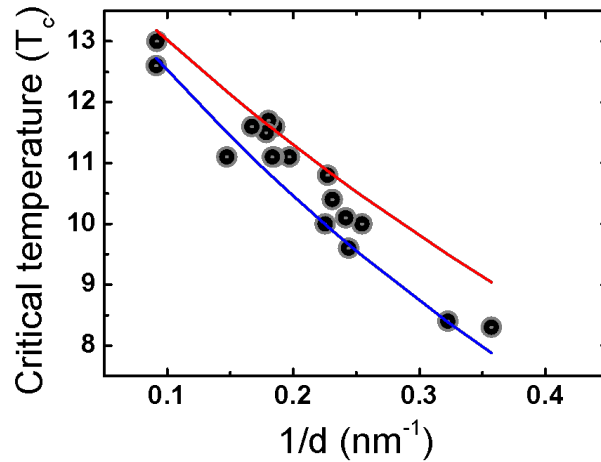
Figure 3.2 – Semi-log plot of the critical temperature $T_c$ measured as a function of 1/d for several NbN thicknesses, from 2.8 to 11 nm (dots). Data is compared with the McMillan model for two values of the parameter $\alpha$ (lines, see the text). Deposition parameters are: $P_{total}$= 2 mTorr and $N_2$ is 10.2 %, with a DC bias of $I_{bias}$= 250 mA and a base pressure $P_{base} < 10^{-9}$ Torr.

### 3.2.3 Reactive gas

For the reproducibility of the films, the initial state of the target plays an important role in the stoichiometry of NbN for sputtering because the nitridisation of the target highly depends on the initial surface conditions (see Ref.[98] and the references therein). For instance, if the growth starts with a highly nitridised target, the resistance of it increases and therefore the voltage drop on the target increases at a given bias current. That changes both the stoichiometry as well as the thickness (as the growth rate changes) of the film. Thus, it is important to have a control on the initial condition of the target to be able to reproduce the same material quality. In the setup, the dependence of the target (Nb) voltage on the nitrogen flow in the chamber is recorded and shown in Figure 3.4. Even though the hysteresis is very small for starting with higher or lower $N_2$ flow (it means that the nitridisation occurs mainly on the surface of the substrate), the strategy taken in this work is to start from a low $N_2$ flow and stabilise it at 1.4 sccm (standard cubic centimeters per minute) to keep the reproducibility. Moreover, at this flow, the bias current ($I_{bias}$) is varied between 150 mA - 350 mA in order to optimise the energy supplied to the positive ions. It is found to be optimum at 250 mA (see the inset in Figure 3.4).

$Nb_x N_{1-x}$ exists in different crystal structures depending on the Nb/N ratio. It shows the best performance in terms of superconductivity when the crystal has a fcc (face-centered cubic) phase, when x is close to 0.5[119]. A lattice parameter of 4.37 Å has been reported for fcc-NbN films as thin as 18 nm[120]. In sputtering, the stoichiometry strongly depends on the $N_2$ pressure introduced into the plasma. In order to attain the optimum
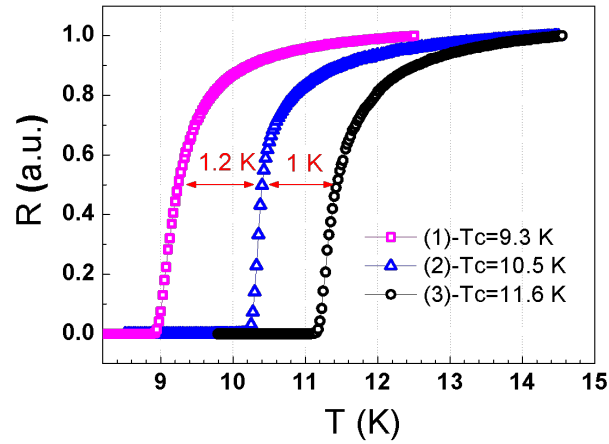
Figure 3.3 – The graph shows the normalised R(T) dependence. It discusses the effect of the chamber conditionings on the film quality. (1, magenta square) is the deposition with no pre-conditioning, (2, blue triangle) the deposition run after the Ti deposition into the deposition chamber prior to the NbN deposition and (3, black circle) after the Ti deposition is performed also on the sample holder. The depositions are performed at $T_{growth}$= 475 °C and $P_{base}$= 2.5 mTorr, and the film thickness is 4.7 nm.



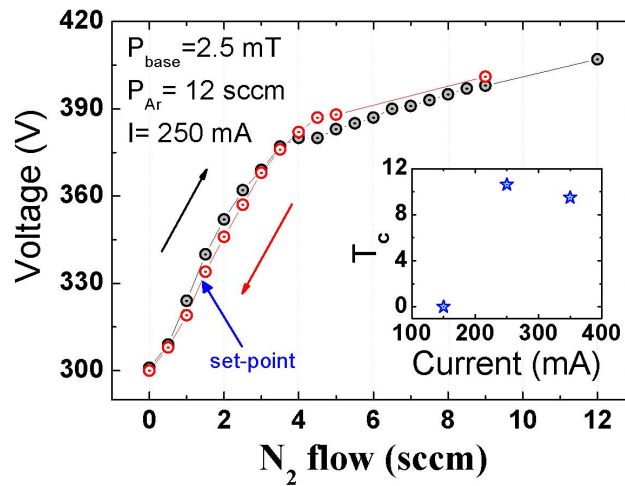Figure 3.4 – Nitridisation level of a Nb target upon varying nitrogen flow introduced into the deposition chamber. The experiment is conducted at 2.5 mTorr base pressure ($P_{total}$), Ar pressure of $P_{Ar}$= 12 sccm and current bias of $I_{bias}$= 250 mA. $N_2$ flow during the deposition is $P_{N_2}$= 1.4 sccm and shown by blue arrow. Inset: For the chosen flow (blue arrow), $T_c$ versus the bias current.

$N_2$ concentration corresponding to a nearly stoichiometric NbN (x $\sim$ 0.5), a range of $N_2$ flow at fixed Ar concentration (12 sccm) is investigated by sweeping the $N_2$ concentration in the gas flow from 33 % down to as low as 0 %[3] for a total base pressure of $P_{total}$= 2.5 mTorr and the results are given in Figure 3.5. It is seen that, the $T_c$ increases when the $N_2$ concentration decreases and then it starts decreasing when $N_2$ concentration overcomes the optimum ($x_{N_2}$= 12 %), probably corresponding to x $\sim$ 0.5 in the $Nb_xN_{1-x}$. In order to minimize the interaction between the sputtered material (Nb) and the plasma, the total pressure is decreased further to 2.0 mTorr (below that level the plasma is difficult to stabilise). Then, the optimum $N_2$ concentration is found to shift from 12 % to 10.2 % for the films in the thickness range of 4.0-4.6 nm as shown in Figure 3.6[4]. The shift could be explained by the different range of the thicknesses as the concentration may vary and also the pump rate for the two different gasses may not be the same.

The similar $T_c$ - $N_2$ dependence is observed also at $P_{total}$= 2.0 mTorr. In Figure 3.6, it is also shown that around the optimum $N_2$ concentration the $T_c$ decreases due to the change in the stoichiometry[5]. $\triangle T_c$ is also observed to decrease with the concentration but it keeps in the range of 0.55 - 0.85 K. The decrease in $\triangle T_c$ could be due to the film thickness that is slightly thicker (t= 4.6 nm) at low-concentration deposition. RRR for the optimised concentration is below 1 as has been observed before[109] and assigned to scattering centers at the grain boundaries.

### 3.2.4 Deposition temperature

It is very essential to preserve the surface quality of the substrate as surface roughness may introduce a shadowing effect during the growth. Moreover, ultrathin films (4-5 nm-thick) mimic the surface of the underlying material. As discussed already in Figure 2.1.2 and section 3.1, As starts to evaporate above 350 °C[99]. Figure 3.7 shows a set of AFM images on bare GaAs (top images) and on NbN/GaAs, and in the figure it is visible that at high temperatures, the surface roughness of GaAs increases (from 0.3 nm to 2.4 nm in rms). From the AFM study, the maximum growth temperature is determined as 450 °C. Figure 3.8 shows the $T_c$ measurement for various nominal deposition temperatures. The $T_c$ clearly increases even above 450 °C. However, the $\triangle T_c$ starts increasing T> 450 °C as the film roughness introduced by the film surface (due to As evaporation) affects the film structure. As discussed later in this chapter, when the films are structured (nanowire meanders), surface roughness may create non-uniformity in the wires and the electro-optical response deteriorates. An optimum growth temperature $T_{growth}^{opt}$= 450 °C is therefore determined as the growth parameter.

Beside the temperature, the baking time[6] is also studied with AFM varying from 10 minutes till 2 hours at 450 °C. The AFM study has shown that while a 15 min of baking time does not introduce any surface roughness (for both non-treated and baked surface it is measured $h_{rms}$= 0.4 nm), after 2h of baking time it is measured $h_{rms}$= 0.6. According

---

[3]Only down to 11% has been shown here as $T_c$ already starts decreasing.

[4]The detectors in chapter 5 and chapter 6 are fabricated at $P_{total}$= 2.0 mTorr with 10.2 % $N_2$.

[5]When there is no $N_2$ (no reactive sputtering), the $T_c$ should go to the critical temperature of Nb (9 K) but this is not observed for $\sim$ 40 nm-thick films.

[6]The time which is required for baking the substrate prior to the deposition of NbN.
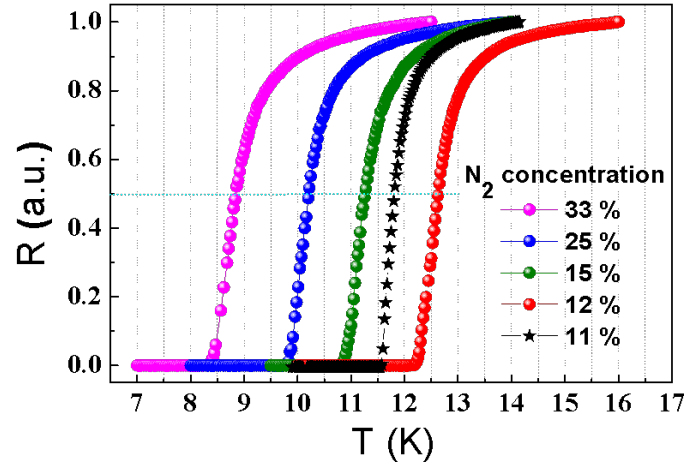
Figure 3.5 – The dependence of R(T) is given for different concentration of $N_2$ (33 % magenta, 25 % blue, 15 % green, 12 % red and 11 % black) introduced during the growth. The parameters of the films are, t= 7-8 nm, T= $T_{growth}$= $T_{growth}^{opt}$= 450 °C), $I_{bias}$= 250 mA and $P_{base}$= 2.5 mTorr. Dashed blue line at R(a.u.)= 0.5 is given to guide the eye for the $T_c$. There is no Ti pre-conditioning.



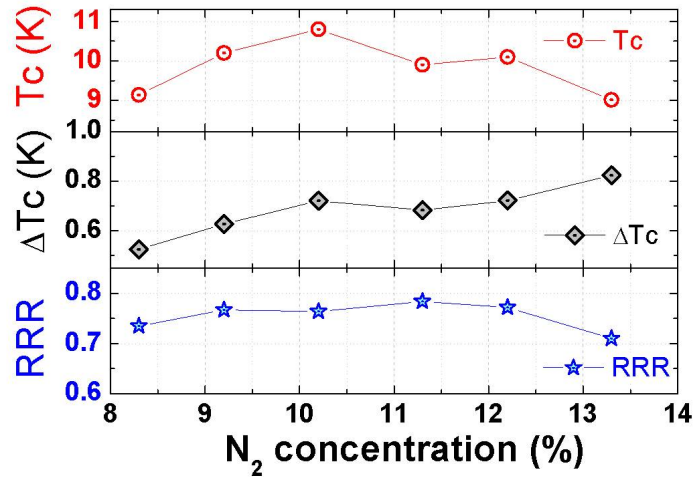Figure 3.6 – From top to bottom $T_c$, $\Delta T_c$ and RRR dependence are plotted as a function of $N_2$ concentration in the plasma. The parameters are: t= 4.0-4.6 nm, $P_{total}$= 2.0 mTorr and $T_{growth}$= $T_{growth}^{opt}$= 450 °C.
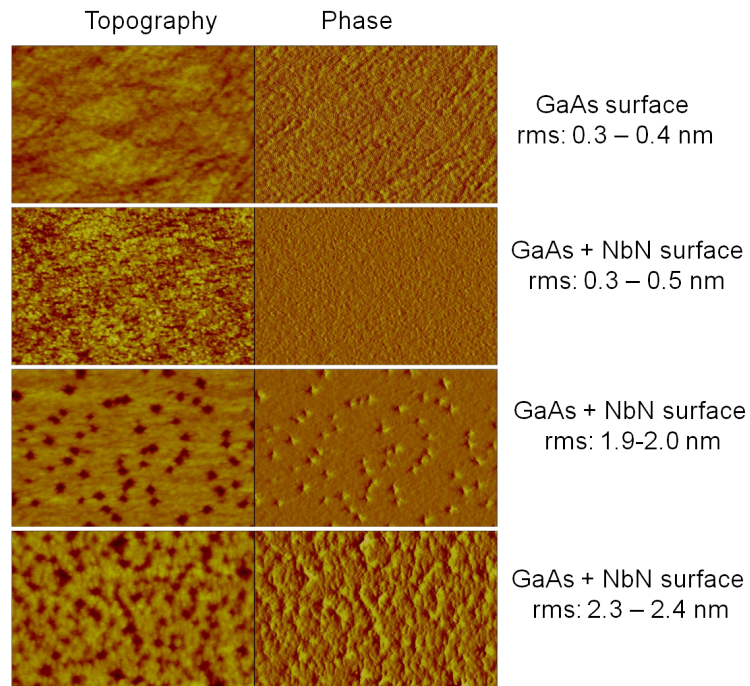
Figure 3.7 – Systematic AFM microscopy study of the surface roughness on films deposited at different temperatures shown as compared to a GaAs substrate (no annealing). From top to bottom: GaAs surface, and films deposited at 450 °C, 500 °C and 550 °C, respectively. The first column shows the surface topography while the second columns show the phase (delay in the oscillation of the cantilever) imaging. For this set of infrared lamps, $T_{growth}^{opt}$ is 450 °C and the films thickness is t $\sim$ 4.5 nm.

to this study, the time is fixed at 15 minutes for the minimum surface roughness and all the films are grown with 15 minutes of baking time (also the results presented in both Figure 3.7 and Figure 3.8).

According to the Thornton zone model[121] (as a universally valid model), the film microstructure is predicted depending on the deposition temperature and the reactive gas. Even though in this model the deposition temperature of this work falls in the quenched growth regime (columnar growth accompanied with voids), the low-pressure reactive gas at low growth rate supports the highly energetic particle bombardment. This clearly shows the need for the magnetron-sputtering technique for NbN film growth. Indeed, the atoms are highly energetic when they are ejected from the target (Nb) and with a very little collision (owing to the low pressure), they can reach to the substrate by retaining most of their kinetic energy (see subsection 2.1.1). Therefore, it is possible to obtain relatively high material quality even at these low growth temperatures[72,122].
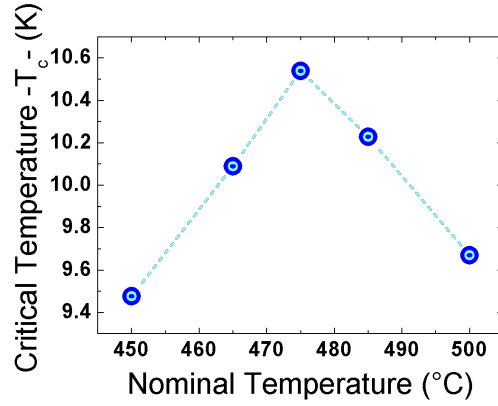
Figure 3.8 – The evolution of the critical temperature, $T_c$ as a function of deposition temperature. The fabrications are performed at $P_{base}$= 2.0 mTorr with a $N_2$ flow of 10.2 %, t= 4-4.5 nm.

### 3.2.5 Device-grade films on GaAs

After varying and adjusting several parameters, from chamber conditioning to deposition temperature, state-of-the-art films are obtained. As a result of the optimization, 4-6 nm-thick NbN films, grown at T= $T_{growth}^{opt}$, 250 mA constant current, 10.2 % $N_2$ partial pressure, and total Ar + N2 flow of 13.4 sccm show very good superconducting properties: $T_c$ in the 10.0 - 11.5 K range and $\triangle T_c < 0.8$ K, see Table 3.1. The superconducting properties of the NbN film depend on the stoichiometry, and therefore the lattice constant and the crystal phase of NbN[119,120]. It is believed that by this $T_c$ optimisation, the stoichiometric NbN has been obtained. The quality of the films obtained in this study is totally comparable with the films grown on standard sapphire[123] and MgO[110] substrates, which have a closer lattice matching with NbN and can be heated up above 500 °C during the deposition.

In order to compare the films on GaAs, in the same deposition run several samples are grown on different substrates (GaAs (001), Si (001 and 111) and $Si_xN_y$ (grown on Si by Mr. M. Swinkels at the TU/e) in order to compare the films. There are two silicon substrates with two different crystal orientations (001-undoped and 111-doped), and two $Si_xN_y$ films deposited on Si with t= 420 nm and t= 600 nm, all with a lattice mismatch of higher than 20 %. The R(T) measurements on these films are shown in Figure 3.9

Table 3.1 – The $T_c$ and $\triangle T_c$ of NbN films on the substrates such as sapphire, MgO and GaAs.

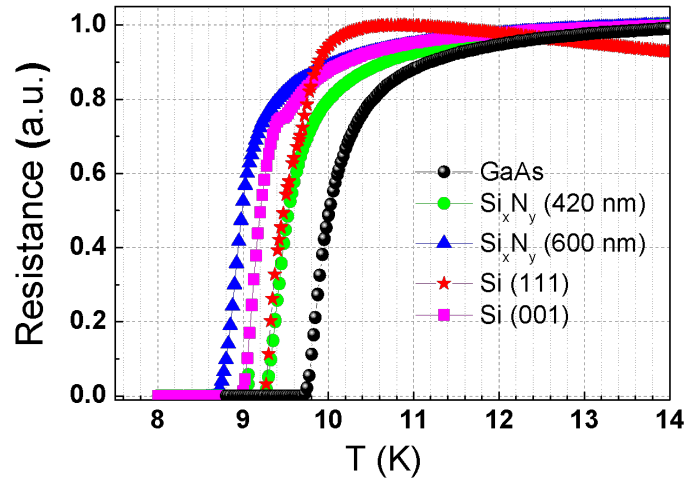| Substrate | $T_c$ (K) | $\triangle T_c$ (K) |
|---|---|---|
| Sapphire | 10.0 - 12.0 | 0.30 - 0.45 |
| MgO | 10.0 - 12.0 | 0.30 - 0.50 |
| GaAs | 10.0 - 11.5 | 0.45 - 0.65 |

Figure 3.9 – R(T) measurement of NbN film on different substrates. GaAs (black solid dots), 420 nm (green solid dots) and 600 nm (blue triangles) thick $Si_xN_y$ on Si, and on bare Si in 111 (red stars) and 001 (magenta squares) orientations. The thickness measured on GaAs is $t = 5.1nm$. The measurements are done under the optimised conditions for GaAs.

and it has been observed that the highest $T_c$ is obtained on GaAs. The subsequent AFM study of those films shows that measured $T_c$ values are not correlated with the surface quality. As Si (111) has smaller lattice mismatch with NbN as compared to Si (001) and the surface roughness measured on it is as low as 0.1 nm, that is most likely the reason for the high $T_c$ obtained. The roughness rises up to 0.6-0.7 nm on $Si_xN_y$ (600 nm-thick). It is known that $Si_xN_y$ grown on Si are stressed. The surface deformations due to stress could be the possible reason for the increase on the measured surface roughness. Thus, thin $Si_xN_y$ with a lower stress possibly gives a higher quality films (see Figure 3.9). This problem is not digged in further but a higher $T_c$ may be achieved as it has been reported elsewhere for $Si_3N_4$ [32] and that may be done by optimising the film surface quality and the depositions conditions (for instance the deposition temperature).

It has been reported that high quality films are obtained on MgO at temperatures down to $\sim$ 295 K [110,122] with state-of-the-arts values of $T_c$. In order to compare the film quality on GaAs with NbN grown on MgO at an elevated temperature, under the optimised conditions two substrates (MgO and GaAs) are mounted in the deposition chamber together. As shown in Figure 3.10, while the film grown on MgO gives a $T_c$ of 11.8 K, on GaAs it decreases to 10.3 K for a film thickness of t= 4.2 nm measured on GaAs by SE (the same thickness is assumed on MgO). Moreover, the $\triangle T_c$ is steeper for the film grown on MgO. A clear difference in the film $T_c$, ($T_c^{MgO} - T_c^{GaAs}$)= 1.5 K is observed. The high $T_c$ of MgO is assigned to a low rms surface roughness of 0.2 nm while it is 0.4 nm for GaAs as well as the lower lattice mismatch between MgO and NbN.
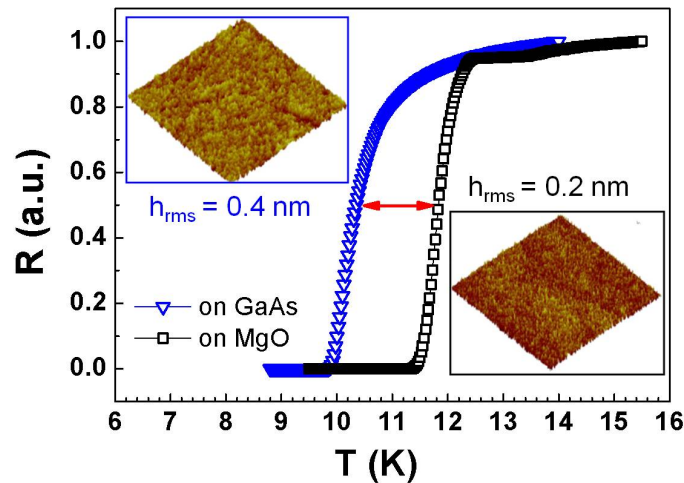
Figure 3.10 – R(T) measurement of NbN ultrathin film on two different substrates, GaAs (blue-open triangle) and MgO (black-open square). The thickness $t = 4.2nm$ is measured on GaAs by SE. Corresponding AFM measurements are shown for a scan range of 1x1 $\mu m^2$ and the surface roughness ($h_{rms}$) of each film is given in the figure.

This study clarifies that the NbN films deposited on GaAs are sufficiently high quality to start the nanofabrication process.

## 3.3 Investigation on TU/e films: NbN single nanowires

In order to separate the problems coming from the SSPD fabrication and/or from the new films, short, single nanowires are fabricated with different widths to study the response of the films electrically. Therefore, four samples are fabricated on the films deposited at different growth temperatures with different thicknesses. The study is done by measuring several properties of the samples, such as the measurement of the room temperature resistances ($R_n$), characteristic IV curves in short- (Figure 3.11) and long-bias range. From the IV curves, the critical current ($I_c$) and the low temperature resistance ($R_{LT}$) are extracted and used for the statistical analysis performed to compare the quality of the NbN films.

The widths of the nanowires are measured by SEM. Even though it is not as accurate as AFM for the measurement of width, it is a quick tool to get a statistic of the widths (see Table 3.2). Lastly, due to the limited time available for these measurements, a very few optical measurements are performed. Therefore, these preliminary optical measurements are not reported as they are not conclusive.

These devices are fabricated in the NanoLab@TU/e facilities except for the last step, reactive-ion-etching, which is done in CNR Rome by Dr. A. Gaggero. The full electrical characterisation of the nanowires is done together with a Bachelor student, Mr. R. op het
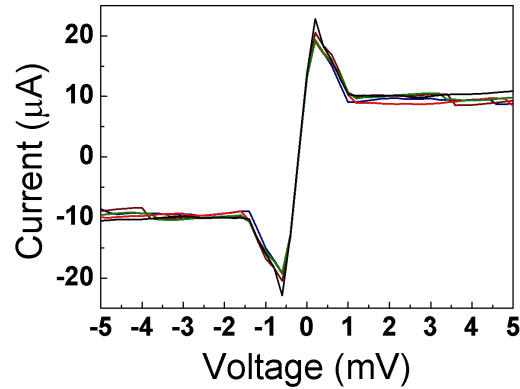
Figure 3.11 – Typical IV curves of five different nanowires with nominal width of 80 nm-wide.

Table 3.2 – The widths of the nanowires measured by SEM. The measurement is done over several nanowires to determine the average and the standard deviation from the nominal width ($w_{nom}$). $w_{nom}$ is the nominal value used in the EBL mask design.

| Sample name | $w_{nom} = 90$ nm $\pm 5$ (nm) | $w_{nom} = 100$ nm $\pm 5$ (nm) | $w_{nom} = 120$ nm $\pm 5$ (nm) | $w_{nom} = 400$ nm $\pm 5$ (nm) |
|---|---|---|---|---|
| GaAs-C152-1t | 90 | 100 | 109 | 403 |
| GaAs-C155-1t | 98 | 116 | 133 | 338 |
| GaAs-C156-1t | 103 | 119 | 136 | 403 |
| GaAs-C157-1t | 107 | 113 | 131 | 380 |

Veld in the $\mu$-PS and a more detailed analysis on the films can be found in his report[124].

## 3.3.1 Design and processing of the single nanowires

The mask design with a dimension of 1.2x1.3 cm$^2$ is used for the contact pads of the nanowire detectors. That mask hosts about 350 devices, each with a contact pad to allow wire-bonding. However, due to the limitation in the size of the sample holder together with the use of copper clamps for a better thermal contact, for each batch only about 100 devices can be characterised in one cooling down. This makes it possible to study about >25 nominally identical nanowires. Due to some processing problems, this value decreases to about the half for GaAs C155 but the number of working devices still allows a statistical study.

In Figure 3.12, the magnified sketch of the devices and the contact pads (GSG configuration) are shown. The nanowires are 17 $\mu$m-long and the width varies from 90 nm to 400 nm. The contact pads and the alignment marks of the detectors are defined by the optical lithography and that is followed by an EBL in order to pattern the nanowires. Table 3.2 summarizes the SEM measurements with the deviations from aimed values. According to the table, there is $\pm$ 5 nm variation from the nominal widths. The dimensions overlap
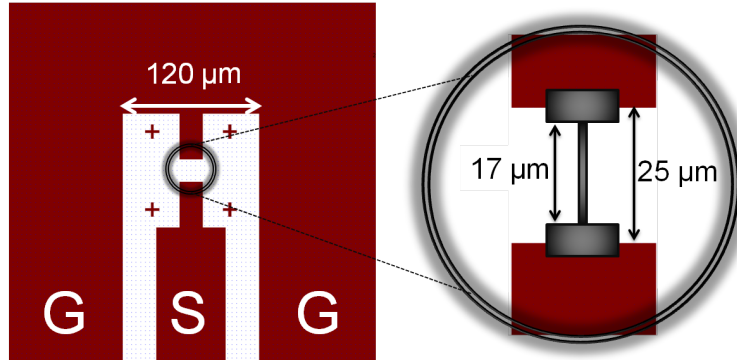
Figure 3.12 – (Left) A sketch of the contact pads and the alignment marks (mask for the optical lithography). The circle shows the area where the devices are defined. (right) A sketch of the nanowires patterned by EBL is shown (not to scale). G; ground, S: signal. The length of the wires is 17 $\mu$m and the width varies between 90 - 400 nm.

with the nominal values better for device GaAs-C152-1t, which has been patterned the last after a slight modification of the dose factors. As the wide wires are not interesting for the single-photon detector fabrication, this large deviation is acceptable only for the electrical characterisation where the calculations consider the variations in width. The fabrication of these devices is widely discussed in subsection 2.1.3.

## 3.3.2  Electrical analysis of single nanowires

By varying the thickness and the growth temperature, four samples have been processed. Two of them (GaAs C155 and C156) are fabricated on a NbN film deposited at an optimum temperature ($T_{growth}^{opt}$= 450 °C) with different thicknesses (5.6 nm for GaAs-C155-1t and 4.9 nm for GaAs-C156-1t). One device is processed on a film with a similar thickness to GaAs-C155-1t but deposited at low temperature (GaAs C152 grown at T= 410 °C) to see whether this has an influence on the performance and the quality of the nanowires as compared to the high temperature growth. Also for the concern of reproducibility among the different growth batches, two samples grown in different batches with nominally the same growth parameters (GaAs C155 and C157) are processed. The details on thickness, $T_c$ and $\triangle T_c$ of the each films are summarised in Table 3.3. As expected, the $T_c$ increases with the deposition temperature and the thickness.

The average critical current (denoted by $\bar{I}_c$ from here on) and the standard deviation ($\sigma$) for every width of each sample are calculated and reported in Table 3.4. In addition, the distribution is calculated for $\sigma/\bar{I}_c$ in percentage (%). For the wider nanowires, the variation is smaller as compared to the narrower wires while the standard deviations measured on the wide wires are larger. It is likely that for wide structures the variation in the width is less dominant due to averaging effect. Therefore, those variations are assigned to the 'constrictions' in the wire due to the fabrication as well as the variations

Table 3.3 – The nanowires fabricated for this set of experiments given with their thickness, critical temperature and growth temperature ($T_{growth}$).

| Sample name | Thickness (nm) | $T_c$ ($\Delta T_c$) | $T_{growth}$ (°C) |
|---|---|---|---|
| GaAs-C152-1t | 5.9 | 10.7 (0.6) | 410 |
| GaAs-C155-1t | 5.6 | 11.6 (0.5) | 450 |
| GaAs-C156-1t | 4.9 | 11.1 (0.7) | 450 |
| GaAs-C157-1t | 5.5 | 11.6 (0.6) | 450 |

in the thickness and/or crystal structure (polycrystalline films)[64] (see Table 3.2). The variations(constrictions) are known to be a limiting factor for the QE since the maximum $I_c$ is determined by the constricted region(s). Therefore, only a single or a few sections of the wire are biased efficiently while the rest of the wire is still biased far from the $I_c$. That means the photon absorbed anywhere along the wire except near the constriction is not registered as a detection event, which is expected to lead to a low efficiency.

In order to verify this conclusion, further analysis has been done. By following the analysis performed in Ref.[64], in order to correct for the small variations in the cross-section area and to compare the all devices of different width, measured $I_c$ of each type is multiplied by its own $R_n$. By this, a number that is independent of the cross section of wire (the width (w) and the thickness ($t_{NW}$)) is determined ($I_c x R_n = J_c x l x \rho$, where $\rho$, $l$ and $J_c$ are the resistivity, length and critical current density of the nanowires, respectively)[125]. The results are plotted in Figure 3.13 and they show that the distribution is wide and asymmetric with a tail at low $I_c R_n$ values, there is a tail in the distribution. This is assigned to the inhomogeneity within the films either because of the thickness or the polycrystalline film. As seen in Table 3.2, the standard deviation of the width around the average does not exceed 5 % for any width. Moreover, from Figure 3.13, it is concluded that the devices fabricated on GaAs-C152 and GaAs-C156 have a wider distribution of the $I_c R_n$ (see also $\sigma$ in Table 3.5) as compared to GaAs-C155 and GaAs-C157. GaAs-C152 [7] is grown at a lower temperature and the reason therefore can be attributed to the crystal structure of the NbN film. Indeed, from HR-XTEM it has been observed that the films deposited at higher temperature tends to have more extending nano-crystallites than ones

---

[7]The distribution of 80 nm wires of GaAs-C152 is slightly less than GaAs-C156 while 400 nm wires are larger

Table 3.4 – The nominal width ($w_{nom}$), average critical current ($\bar{I}_c$), standard deviation ($\sigma$) and the ratio of $\bar{I}_c/\sigma$ are given for every sample with different wire widths.

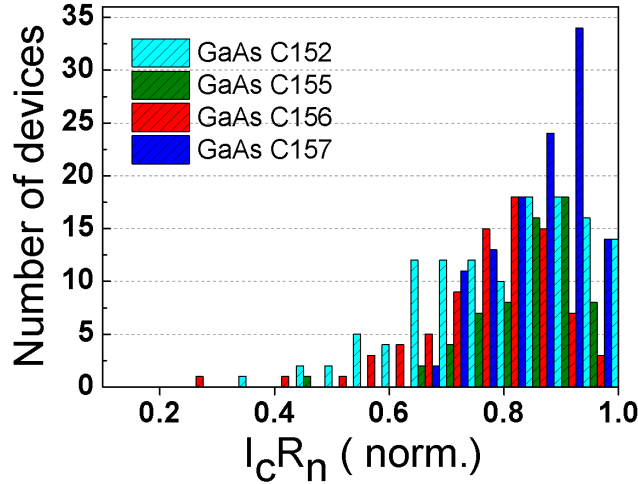| | GaAs C152-1t | | | | GaAs C155-1t | | | | GaAs C156-1t | | | | GaAs C157-1t | | | |
|---|---|---|---|---|---|---|---|---|---|---|---|---|---|---|---|---|
| $w_{nom}$(nm) | 90 | 100 | 120 | 400 | 90 | 100 | 120 | 400 | 90 | 100 | 120 | 400 | 90 | 100 | 120 | 400 |
| $\bar{I}_c$($\mu A$) | 12.3 | 14.4 | 18.9 | 46.7 | 16.4 | 18.6 | 25.2 | 49.8 | 14.1 | 18.2 | 21.7 | 48.9 | 15.7 | 17.4 | 21.2 | 45.6 |
| $\sigma$ | 2.1 | 2.7 | 2.1 | 5.4 | 2.1 | 3.4 | 1.0 | 5.9 | 2.6 | 3.2 | 2.4 | 3.1 | 2.0 | 1.9 | 1.4 | 4.1 |
| $\sigma/\bar{I}_c$ (%) | 17 | 19 | 11 | 11 | 13 | 18 | 4 | 12 | 19 | 18 | 11 | 6 | 13 | 11 | 7 | 9 |

Figure 3.13 – Histogram for the normalised $I_cR_n$ for 17 $\mu$m-long and w= 90 - 400 nm-wide nanowires fabricated on four NbN films with different growth parameters. The normalisation is done by dividing the $I_cR_n$ values by the maximum measured in that particular batch.

deposited at low temperature. In Figure 3.14 the upper image is taken from the films grown at lower temperature (T= 410 °C) while the one at the below is from a higher temperature (T= 475 °C). The micrographs confirms that the temperature supports the larger nanocrystal formation in the quenched-growth regime. This also shows itself in the electrical response of the wires. The $I_c$ values obtained on GaAs-C152 are lower than the rest (see Table 3.4). The batch GaAs-C156 is grown at a nominally optimised temperature, but it is thinner. Thus, that could be the reason of the wider distribution since the variations in the thickness have a relatively larger impact. Moreover, the films grown in different batches with nominal deposition parameters (GaAs-C155 and GaAs-C157) show very similar electrical characteristics and a similar distribution of $I_cR_n$, as shown in Figure 3.13. The variance observed in Table 3.4 is expected to be due to the variation related to the processing between the two batches.

The average RRR is calculated for a few tens of nanowires on each film and averaged in order to compare it with the value obtained on the unprocessed films deposited in the same deposition run. After (before) the processing, they are 0.77 (0.79), 0.84 (0.89), 0.81 (0.85) and 0.74 (0.85) for GaAs-C152, GaAs-C155, GaAs-C156 and GaAs-C157, respectively. It shows that the film quality is not affected much by the processing. These numbers can be improved more with a further optimisation in the processing.

From the $I_c$ measurements, $J_c$ values are derived from $J_c = I_c/(t_{NW} \cdot w)$. The parameters, $t_{NW}$ (thickness of the nanowire) and w are extracted from SE and SEM measurements, respectively. The results are presented in Figure 3.15. While in the literature $J_c$ values from 2 MA/cm$^2$ up to 7 MA/cm$^2$ (on sapphire[126]) have been reported, the values reported
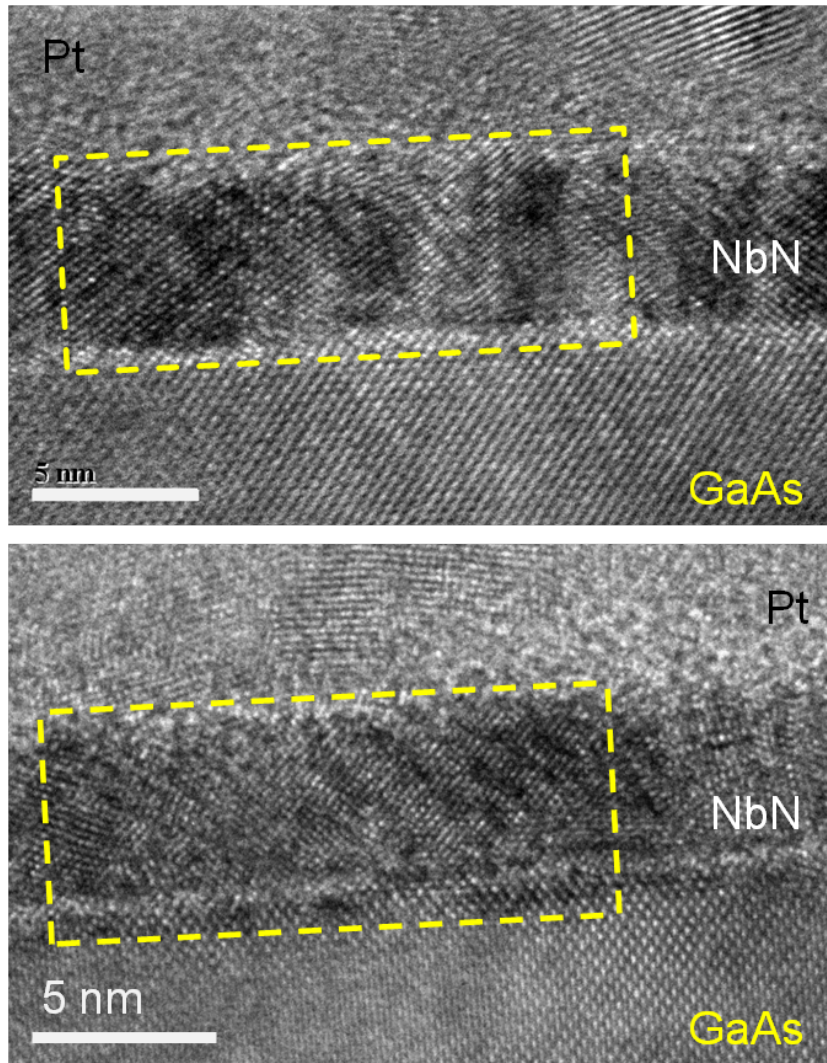
Figure 3.14 – HR-XTEM images of the films deposited at (up) T= 410 °C ($T_{growth}^{opt} = 410°C$) and (down) T= 475 °C ($T_{growth}^{opt} = 450°C$). The samples are prepared by Dr. B. B. Campo and the measurement is done by Dr. M. A. Verheijen.
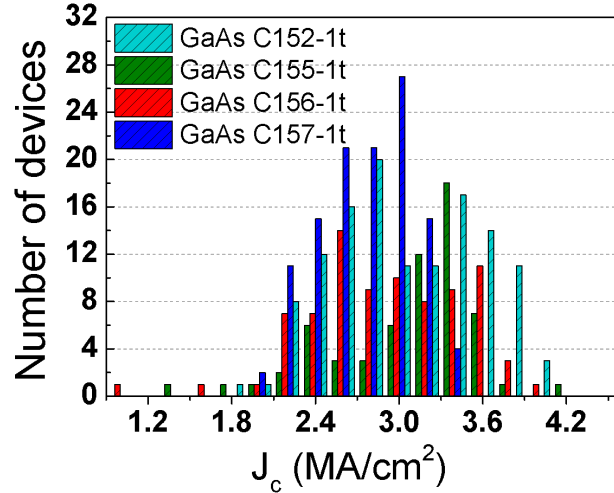
Figure 3.15 – Histogram of the $J_c$ for 17 $\mu$m-long and w= 90 - 400 nm-wide nanowires. $J_c$ varies between roughly 2.0 - 4.0 MA/cm$^2$ and that falls in the range of the values reported in the literature.

here are comparable with the values reported on GaAs[72].

For the completeness of the analysis, in Table 3.5 the summary and the comparison of four devices are given. The samples GaAs-C155 and GaAs-C157 have a higher $J_c$. They also have more uniform $J_c$ and $\bar{I_c}R_n$ (column total in the table). This may be explained by the thicker NbN film. This way, the non uniformity in the NbN nanowires does not influence the current as much as in thinner nanowires. Sample GaAs-C156 has a higher current density than GaAs-C152, but is less uniform than samples GaAs-C155 and GaAs-C157, because the nanowires are thinner. The $\bar{I_c}R_n$ method gives a lower standard deviation compared to the $J_c$. The $I_c R_n$ method reduces slightly the standard deviation compared to $J_c$. This can be because of the local defects which affect $I_c$ and $R_n$ differently. The $J_c$ values are calculated with an average width for all nanowires of the same type on one sample. The real width of several of these wires are measured with SEM. In the $\bar{I_c}R_n$ method however, the $R_n$ is measured for each nanowire separately. This way, the variations in width are more precisely eliminated while in $J_c$ this is not possible because the parameters are defined as average.

## 3.3.3 Summary of electrical analysis

The understanding of the correlation between the films properties and the device response is an important issue in order to improve the efficiency of the single-photon detectors for highly demanding applications as mentioned in section 1.1. This study holds the important findings to direct the studies on the film properties of NbN on GaAs substrate.

To conclude this section, by varying the nominal growth temperature and the thickness

| GaAs | w (nm) → | 90 nm type | | | 100 nm type | | | 120 nm type | | | 400 nm type | | | Total | | |
|------|----------|------|---------|------|------|---------|------|------|---------|------|------|---------|------|------|---------|------|
| | | $\bar{I}_c$ | $\bar{I}_c R_n$ | $J_c$ | $\bar{I}_c$ | $\bar{I}_c R_n$ | $J_c$ | $\bar{I}_c$ | $\bar{I}_c R_n$ | $J_c$ | $\bar{I}_c$ | $\bar{I}_c R_n$ | $J_c$ | $\bar{I}_c$ | $\bar{I}_c R_n$ | $J_c$ |
| **C152** | Average | 12.3 | 0.7 | 23.2 | 14.4 | 0.7 | 24.6 | 18.9 | 0.9 | 29.4 | 46.7 | 0.7 | 19.5 | / | 0.8 | 24.3 |
| | σ | 2.1 | 0.2 | 4.0 | 2.7 | 0.1 | 4.6 | 2.1 | 0.1 | 3.3 | 5.4 | 0.1 | 2.2 | / | 0.1 | 5.2 |
| | % | 17.3 | 16.2 | 17.2 | 18.9 | 20.2 | 18.9 | 11.1 | 15.1 | 11.2 | 11.5 | 19.5 | 11.5 | / | 18.5 | 21.3 |
| **C155** | Average | 16.4 | 0.7 | 29.6 | 18.6 | 0.8 | 28.7 | 25.2 | 0.9 | 33.6 | 49.8 | 0.8 | 23.3 | / | 0.9 | 30.9 |
| | σ | 2.1 | 0.1 | 3.9 | 3.4 | 0.1 | 5.2 | 1.0 | 0.04 | 1.4 | 6.0 | 0.1 | 2.8 | / | 0.1 | 5.1 |
| | % | 13.0 | 10 | 13.0 | 18.1 | 15.1 | 18.1 | 4.1 | 4.1 | 4.1 | 12.0 | 8.2 | 12.0 | / | 11.0 | 16.5 |
| **C156** | Average | 14.1 | 0.7 | 27.9 | 18.2 | 0.8 | 31.5 | 21.7 | 0.8 | 32.6 | 48.9 | 0.8 | 24.8 | / | 0.8 | 29.1 |
| | σ | 2.6 | 0.1 | 5.2 | 3.2 | 0.1 | 5.5 | 2.4 | 0.1 | 3.5 | 3.1 | 0.03 | 1.6 | / | 0.1 | 5.5 |
| | % | 18.8 | 18.0 | 18.8 | 17.6 | 15.6 | 17.6 | 10.8 | 9.9 | 10.8 | 6.4 | 3.8 | 6.4 | / | 15.4 | 18.7 |
| **C157** | Average | 15.7 | 0.8 | 26.6 | 17.4 | 0.9 | 28.2 | 21.2 | 0.9 | 29.4 | 45.6 | 0.9 | 24.5 | / | 0.9 | 27.5 |
| | σ | 2.0 | 0.1 | 3.4 | 1.9 | 0.1 | 3.1 | 1.4 | 0.04 | 2.0 | 4.1 | 0.1 | 2.2 | / | 0.1 | 3.4 |
| | % | 12.9 | 10 | 12.9 | 10.9 | 9.3 | 10.9 | 6.8 | 5.0 | 6.8 | 9.0 | 7.5 | 9.0 | / | 8.8 | 12.2 |

Table 3.5 – For the each type (width (w)), the average critical current ($\bar{I}_c$), $\bar{I}_c R_n$ and $J_c$ are reported with their average and standard deviation (σ) values as well as the ratio of two, $\bar{I}_c / \sigma$. The units of $\bar{I}_c$, $\bar{I}_c R_n$ and $J_c$ are μA, V and $\times 10^5$ A.cm$^2$

of the films, a statistical analysis has been conducted on the nanowires. It has been concluded that the devices fabricated on the films deposited at high temperature (GaAs-C155 and GaAs-C157) are more uniform in terms of their electrical responses as compared to the films deposited at low temperature (GaAs-C152). This can be explained by the crystal quality increasing with the deposition temperature[121]. The uniformity increases with thicker films (GaAs-C155) compared to thinner ones (GaAs-C156) as well and the thick films have high $T_c$. As discussed in subsection 3.2.1, the inter layer formed between a superconducting and non-superconducting (substrate) degrades the superconductivity (due to the effect so called proximity)[115,118] by forming a sub-nanometer layer. This is a likely reason for the observation of improving electrical response for the devices fabricated on thicker films. Lastly, as the wire gets narrower, the small variations in the thickness and/or in the width starts to be more critical. Therefore, the variations decreases with the wire width (see Table 3.5).

## 3.4 Optical constants of NbN extracted from SE measurements

For the films deposited under the optimised conditions, an SE measurement is performed on the same film by ellipsometry in the UV (200 - 1000 nm) and NIR (240 - 1600 nm) spectral ranges. For the film inspected under both spectral ranges, also an HR-XTEM analysis is done. Therefore, that particular sample is the most outstanding candidate for the determination of the optical constants.

In order to compare the optical constants of the NbN films grown on GaAs with the values reported in the literature for 12 nm-thick films[71], first a thick film (t= 10 nm) is measured by a UV ellipsometry. A complex dielectric constant of ñ= 3.8 - i4.4 is reported at 1000 nm for that 10 nm-thick film. This result agrees well with the results on 12 nm film[127]. After being confident with the results of the thick films and seeing that there is a considerable difference between the optical constant of thick and thin films, this study is performed on a thin film in the thickness range that is mostly used for the fabrication of the single-photon detectors. First of all, as for all the measurements performed with UV- SE, the B-spline fitting is used for the measurement of the thickness, which is $t^{SE}$= 4.9 $\pm$ 0.1 nm. The HR-XTEM measurement validates a thickness $t^{TEM}$= 5.4 $\pm$ 0.2 nm. As the data is agreeing quite well, NIR- SE measurement is performed on the same sample in order to extract the optical constants at 1310 nm and 1550 nm. For the NIR- SE measurement, the thickness is fixed to the value determined by UV-SE and used to get the optical constant for the near infrared range of the spectrum. The real (n) and imaginary (k) parts of the dielectric constants (ñ= n - ik) of NbN ultrathin film deposited on GaAs (001) (fitted by B-spline model) are given as a function of wavelength in Figure 3.16. The dielectric constants at the telecom wavelength are reported in Table 3.6 are lower as compared to the values reported in Ref.[71] for a 12 nm-thick film on sapphire, which has been used in the literature in order to simulate the detector structures[8].

---

[8]The dielectric constants of NbN are all reported at room temperature in the literature.

| Wavelength (nm) | 1310 | 1550 |
|---|---|---|
| n | 4.35 | 4.82 |
| k | 4.65 | 4.83 |

Table 3.6 – Optical constants of 4.9 nm NbN on GaAs, measured by SE at room temperature.
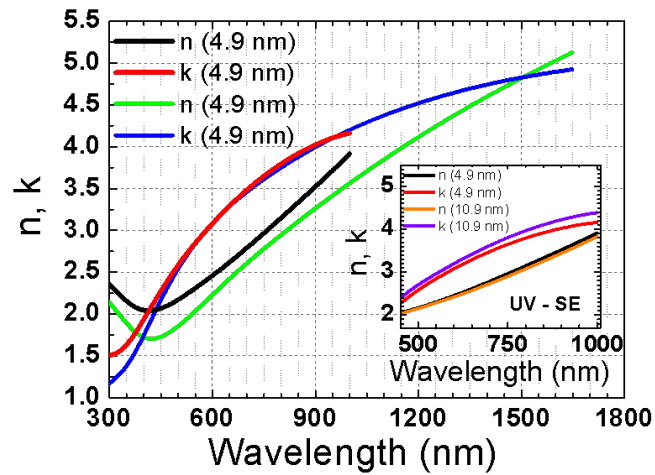


Figure 3.16 – Wavelength dependence of the optical constants for a 4.9 nm-thick NbN film on GaAs (001) substrate in different spectral ranges (see the legend). n is the real part, k is the imaginary part of the refractive index, ñ= n - ik. After comparing two different thicknesses in UV-SE (inset), it has been used to compare the NIR-SE spectral dependence of the thin film as well.

# 4

# Superconducting Waveguide Single Photon Detectors

This chapter[1] introduces a key component for integrated quantum information processing, the superconducting waveguide single-photon detectors (WSPDs). The WSPDs demonstrated in this chapter are fully compatible with the integration of single-photon sources and passive networks on the same material platform (GaAs/ AlGaAs).

In the following, the design, fabrication and the results of the WSPDs are discussed. The detectors are initially optimised for a high absorption in TE mode, therefore they are shown to be polarisation dependent which has been addressed and modified for polarisation-independent detection in later detector designs, used for integrated auto-correlators (chapter 5) and waveguide photon-number-resolving detectors (chapter 6).

## 4.1 Introduction

The monolithic integration of quantum photonic circuits, as needed for scaling to meaningful number of qubits[14], has been limited to passive implementations[19,128], due to the difficulty of integrating sources, waveguides and detectors on the same substrate. Thus, a waveguide single-photon detector is one of the key components of such a quantum integrated photonic circuit. Moreover, the waveguide configuration provides above 90 % absorption in superconducting wires after a few tens of micrometers. That also addresses the absorption-limited quantum efficiency (see Figure 1.5.1) due to very thin films for free-space coupling and provides high efficiencies.

The WSPDs discussed in this chapter[29] are the first demonstration of waveguide single-photon detectors on III-V material system. The detectors, based on superconducting nanowires on GaAs ridge waveguides, provide high efficiency (20 %) at telecom wavelengths, high timing accuracy ($\sim$ 60 ps), dead time in the ns range, and are fully com-

---

[1]The results of this chapter have been partly published in Appl. Phys. Lett. 99, 181110 (2011)
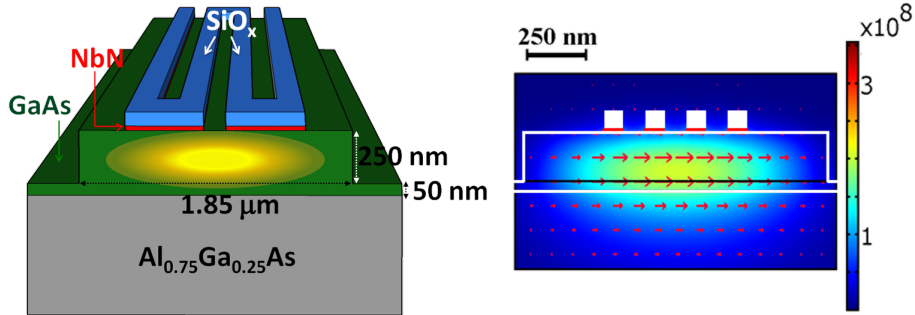
Figure 4.1 – (Left) Schematic view of the waveguide single photon detector structure. (Right) Contour and vector plots of the electrical field for the fundamental quasi-TE mode at $\lambda$=1.3 $\mu$m. The white line emphasizes the borders of GaAs, the red line is showing the NbN wires and the white squares are for SiO$_x$ (see the sketch on the left). The arrows show the direction and amplitude of the electric field.

patible with the integration of single-photon sources and passive photonic networks. In parallel to this work, this essential approach has been realised by other groups as well as ours due to the importance of the concept. The waveguide detectors based on superconducting nanowires are reported on variety of material systems. First reports have appeared in 2011 on materials including GaAs[29], silica[30] and Si[31]. Later on, more work have been reported on similar material systems[32,33,129]. So far, above 90 % device quantum efficiency has been reported on waveguide structures by using NbN nanowires[31].

The work presented in this chapter is a collaboration between CNR, Rome (group of Dr. R. Leoni), University of Würzburg (UW, group of Prof. M. Kamp and Dr. S. Höfling) and Eindhoven University of Technology (TU/e). The heterostructure is grown by molecular-beam epitaxy (MBE) at UW by Mr. M. Lermer and the NbN films are grown by DC-magnetron sputtering at the École Polytechnique Fédérale de Lausanne (EPFL, group of Dr. R. Sanjines) by the author of this thesis together with Dr. A. Gaggero. The processing has been done in CNR by Dr. A. Gaggero and the waveguides are etched by dry-etching at UW by Mr. J. Beetz. The characterisation is done by the author and Dr. J. P. Sprengers at the TU/e.

## 4.2 Concept and design

The WSPDs are based on the principle of photon-induced hot-spot creation in ultranarrow superconducting NbN wires, which is also used in nanowire superconducting single-photon detectors (SSPDs)[48] and can provide high sensitivity at telecommunication wavelengths, high counting rates, broad spectral response and high temporal resolution due to low jitter values (see section 1.3). The NbN wires are deposited and patterned on top of a GaAs ridge waveguide, in order to sense the evanescent field on the surface as pointed in Figure 4.1.

Four NbN nanowires (4 nm-thick, 100 nm-wide and spaced by 150 nm) are placed

on top of a GaAs (300 nm)/$Al_{0.7}Ga_{0.3}As$ waveguide, and a 1.85 $\mu$m-wide, 250 nm-deep ridge is etched to provide 2D confinement for the waveguide mode. A 100 nm-thick $SiO_x$ layer is considered on top of the wires as a residue of the hydrogen silsesquioxane (HSQ) mask used for patterning the wires. The dimensions of the waveguide have been optimized to obtain maximum absorption by the NbN wires while leaving a 0.5 $\mu$m alignment margin between the wires and the side of the ridge. The electric field amplitude and polarisation for the fundamental mode whose polarisation is mainly transverse-electric (TE) is calculated using a finite-element mode solver (COMSOL Multiphysics) and shown in Figure 4.1(right) for $\lambda = 1.3$ $\mu$m. For this quasi-TE mode and the corresponding quasi-transverse-magnetic (TM) mode, the modal absorption coefficients of $\alpha_{TE} = 451$ cm$^{-1}$ and $\alpha_{TM} = 391$ cm$^{-1}$ are calculated for a refractive index of NbN, $n_{NbN} = 5.23 - 5.82i$[71]. The high absorption coefficient in TE polarisation corresponds to 90 % (99 %) absorptance after 51 $\mu$m (102 $\mu$m) propagation length. This very high absorptance in an ultrathin wire is unique to waveguide geometries, which allow an interaction length limited only by extrinsic waveguide losses. Since the NbN wires produce a very small perturbation to the guided mode, the impedance mismatch at the interface between the passive waveguide without wires and the detecting section is negligible (calculated modal reflectivity of 5.84x10$^{-5}$ %), allowing very efficient coupling to the detector. It should be noted that this design with a TE-polarized, tightly-confined mode is optimized for on-chip applications with integrated single-photon sources (quantum dots in waveguides), which emit in the TE polarisation. The TM-polarized mode has a complex spatial profile, which makes the fiber coupling inefficient. By increasing the waveguide thickness by 50 nm, the mode profile is improved and well-confined TM modes with high modal absorption coefficients > 500 cm$^{-1}$ are demonstrated as discussed later, at the end of this chapter. The absorptance of both TE and TM light then approaches $\sim$ 90 % for 50 $\mu$m-long waveguide, resulting in a polarisation-independent quantum efficiency.

## 4.3 Device fabrication

NbN nanowires are placed on top of a GaAs (300 nm)/$Al_{0.75}Ga_{0.25}As$ (1.5 $\mu$m) heterostructure grown by molecular beam epitaxy on an undoped GaAs (001) substrate. A 4.3 nm-thick NbN layer is deposited by dc reactive magnetron sputtering of a Nb target in a $N_2$/Ar plasma at a nominal temperature of 350 °C[2], with deposition parameters optimized for GaAs substrates[72], resulting in a critical temperature $T_c$=10.0 K, and a transition width $\Delta T_c = 0.65$ K. WSPDs are then fabricated using four steps of direct-writing 100 kV electron beam lithography (EBL). In the first step, Ti(10 nm)/Au(60 nm) contact pads (patterned as a 50 $\Omega$ coplanar transmission line) and alignment markers are defined by lift-off using a PMMA-mask as shown in Figure 4.3(a). In the second step, the meander pattern is defined on a 180 nm-thick hydrogen silsesquioxane (HSQ)-mask and then transferred to the NbN film with a $CHF_3$+$SF_6$+Ar reactive ion etching (RIE). Figure 4.3(b) shows a scanning electron microscopy (SEM) image of an etched wire. The

---

[2]This film has been grown in a different system (at EPFL) than the one used for the optimisation described in chapter 3 (at TU/e). Therefore, the deposition temperatures should not be compared.
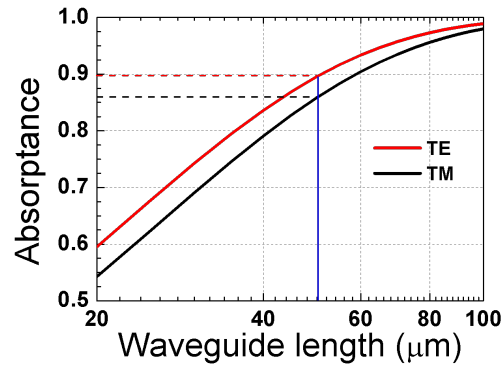
Figure 4.2 – Calculated absorptance of a waveguide single-photon detector with four-wires on a waveguide (see Figure 4.1) for TM (red solid line) and TE (black solid line) polarizations. The straight line shows a 50 $\mu$m-long waveguide with a corresponding absorptance of TE (horizontal, red-dashed line) and TM (horizontal, black dashed line).
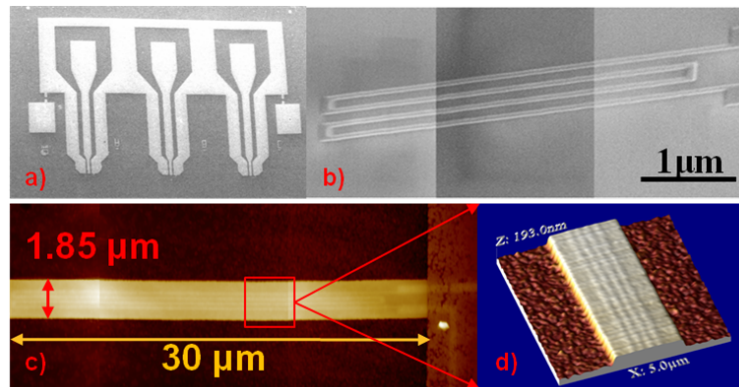


Figure 4.3 – (a) Scanning electron microscope (SEM) micrograph of Ti/Au electric contacts. (b) Collection of three SEM micrographs taken in different regions of a 30 $\mu$m-long WSPD, the nanowires are still covered by the HSQ etching mask. (c) Atomic force microscope (AFM) image of the 1.85 $\mu$m-wide and 30 $\mu$m-long waveguide with an HSQ mask used for the etching of the waveguide, aligned on top of the NbN nanowires. d) Enlarged AFM view of a WSPD after RIE dry etching, showing a realignment accuracy better than 100 nm. The SEM and AFM pictures are taken by Dr. A. Gaggero.

meandered NbN nanowire (100 nm width, 250 nm pitch, 30-100 $\mu$m length), still covered with the HSQ-mask, is very regular with a width uniformity of about 5 %. In the third step, an HSQ-mask for the waveguide patterning is defined by carefully realigning this layer with the previous one. This layer also protects the Ti/Au pads against the subsequent reactive etching process. Figure 4.3(c) shows an atomic force microscopy (AFM) image of the waveguide etch mask aligned to the wires, showing realignment accuracy better than 100 nm (Figure 4.3(d)). Successively, 250 nm of the underlying GaAs layer is etched by an ECR (electron cyclotron resonance) RIE using a chlorine based recipe ($Cl_2$+Ar). Finally, in order to allow the electrical wiring to the TiAu pads, holes through the remaining HSQ-mask are opened using a PMMA mask and RIE in a $CHF_3$ plasma. The waveguides are cleaved leaving a 1 mm-long passive ridge waveguide between the cleaved facet and the WSPD.

## 4.4 Measurement setup

The WSPDs are characterized in the waveguide probe station (w-PS, see subsection 2.2.2) by end-fire coupling light using a polarization-maintaining lensed fiber with a nominal spot diameter of 2.5 $\pm$ 0.5 $\mu$m at full-width-half-maximum (FWHM) and a working distance of 14 $\pm$ 2 $\mu$m. As the setup is already explained in subsection 2.2.2, it is not detailed here. The fiber and a $\mu$-probe are located on the piezo stages at the two opposite sides of the sample holder. The output signal is amplified using a set of low-noise, negative-gain amplifiers from Mini-Circuits (with a bandwidth of 20-6000 MHz).

## 4.5 Performance of waveguide single-photon detectors

The inset of Figure 4.4 displays the current-voltage characteristic measured for a 50 $\mu$m-long WSPD, showing a critical current ($I_c$) of 16.9 $\mu$A. The electro-optical response is measured by end-fire coupling a continuous wave 1310 nm diode laser through the lensed fiber in the TE polarization. The detector count rate has been observed to be extremely sensitive to the fiber-waveguide alignment and to their distance, confirming that the detector responds to guided photons and not to stray light propagating along the surface or in the substrate. The count rate is measured to be proportional to the laser power (Figure 4.4), proving operation in the single-photon regime.

The measured quantum efficiency (QE) (1310 nm, TE polarization) is plotted in Figure 4.5 (left axis) as a function of the normalized bias current $I_b/I_c$. The system quantum efficiency (SQE, blue dots), defined as the number of counts divided by the average photon number in the fiber at the input of the cryostat (see Figure 2.10), reaches 3.4 % for a 50 $\mu$m-long device. For determining the number of photons coupled into the waveguide, a transmission measurement is performed on a sample containing only 3 mm-long ridge waveguides, without NbN wires and contact pads. The transmission of a tunable laser through the entire system including fibers and waveguide is measured by replacing the $\mu$-probe with another lensed fiber (nominally it is the same as the other lensed fiber) on the second piezo tower. From the measured Fabry-Perot fringes (see Figure 4.8), and par-
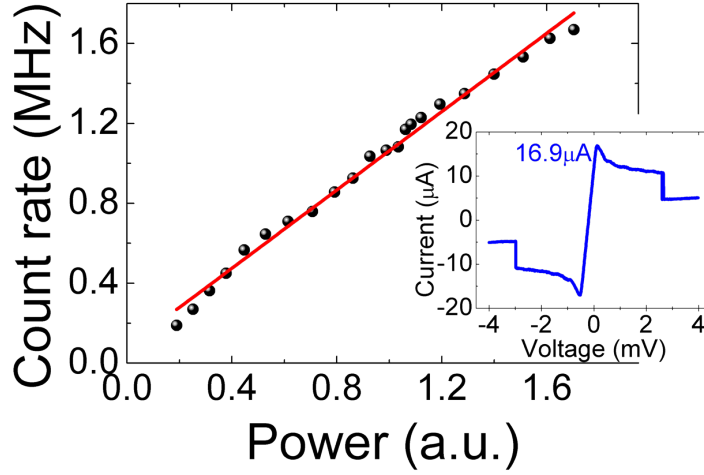
Figure 4.4 – Count rate as a function of laser power ($\lambda$= 1310 nm, TE polarization, $I_b$= 9.9 $\mu$A), showing a linear behaviour and hence operation in the single-photon regime. Inset: Current-voltage characteristic of the WSPD, showing a critical current of 16.9 $\mu$A.

ticularly from the maximum and minimum transmission (in TE polarisation), $T_{max}$=6.1 % and $T_{min}$=1.8 %, the propagation loss over a 3 mm waveguide length is deduced using the equation [130],

$$\alpha_{abs} = -\frac{1}{L} ln\left(\frac{1}{R}\frac{T+1}{T-1}\right) \tag{4.1}$$

and

$$T = \sqrt{\frac{T_{max}}{T_{min}}} \tag{4.2}$$

where $\alpha_{abs}$ is the absorption coefficient, L is the propagation length, R= 0.27 is the reflectance and $T^2$ is the visibility. The absorption coefficient is calculated to be negligible for our devices.

Then, assuming symmetric input/output coupling and using the standard expression for the Fabry-Perot transmission [131],

$$\eta_c e^{-\frac{L}{2}} = \frac{2\sqrt{T_{max}T_{min}}}{\sqrt{T_{max}} + \sqrt{T_{min}}} \tag{4.3}$$

where $\eta_c$ is the coupling efficiency, a coupling efficiency (from fiber input to waveguide) of 17.4 % is derived for the TE polarisation. The corresponding device quantum efficiency (DQE), defined with respect to the number of photons coupled to the waveguide, is plotted (red dots) in Figure 4.5, and reaches 19.7 % at the maximum bias current.

This value is still lower than the calculated absorptance (90 % in the 50 $\mu$m-long WSPD) as depicted in Figure 4.2 which is mainly attributed to a limited internal quantum
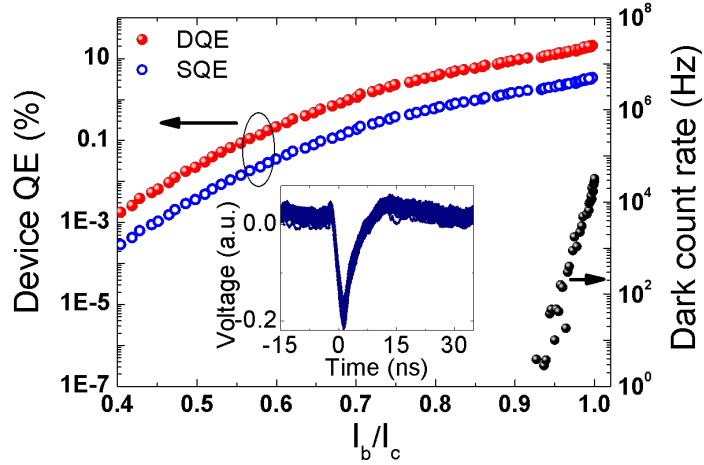
Figure 4.5 – System QE (blue dots) and device QE (red dots) of a 50 $\mu$m-long WSPD under illumination at 1310 nm in the TE polarization (left axis) and dark count rate (black dots, right axis) as a function of the normalized bias current. Inset: Photoresponse of a WSPD after 48 dB amplification.

efficiency (detection probability upon absorption of a photon), and further improvements of film quality and wire etching process may result in notably improved values. Another potential cause for limited efficiency may be extrinsic loss (e.g. scattering) due to the nanowires, which is however believed to be small as compared to nanowire absorption. The dark count rate (DCR) is measured in another cryostat (VeriCold, see[104]) without optical windows at 1.2 K and is presented on the right axis of Figure 4.5, showing the usual exponential dependence as a function of the bias current. The DCR measured in the w-PS on this device has already been reported in Figure 2.12 and are much higher due to the blackbody radiation.

The inset in Figure 4.5 shows a photoresponse pulse of a WSPD, showing a pulse duration (full-width-half-maximum) of 3.2 ns and a 1/e decay time of 3.6 ns, which corresponds very well to the expected time constant $\tau_{1/e}=$ $L_{kin}/R=$ 3.6 ns, where $L_{kin}=$ 180 nH is the wire kinetic inductance (as calculated from the kinetic inductance per square for similar NbN wires, $L_{\square}=$ 90 pH/$\square$[132]), where R= 50 $\Omega$ is the load resistance. Considering that it takes a time $\approx 3\tau$ to recover 95 % of the bias current after detection, a maximum counting rate close to 100 MHz is estimated. By illuminating the device with a pulsed diode laser, a total jitter of 73 ps is measured on the WSPD output pulse, corresponding to a 61 ps intrinsic detector jitter after correcting for the 40 ps jitter from the laser pulse.
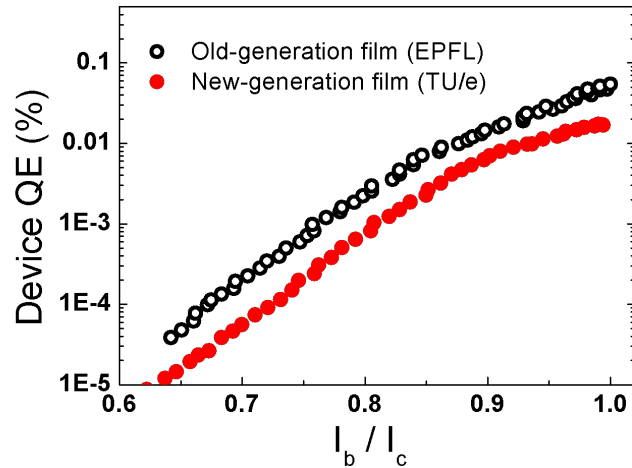
Figure 4.6 – Comparison of the device quantum efficiency (QE) of the two films for the top coupling. The films are deposited on the waveguide heterostructures at TU/e (red filled circle, new generation films) and at EPFL (black open circles, old generation films). The measurement is taken with a continuous-wave diode laser at $\lambda = 1310$ nm.

## 4.5.1 Comparison of the WSPD performances on TU/e grown films

As the optimisation of the film process on GaAs started at TU/e with this work, the results discussed in this chapter are obtained with the films grown in EPFL. After the optimisation process, described in chapter 3, in order to compare the quality of films grown at the TU/e to those grown at EPFL, WSPD has been fabricated using the TU/e films with a similar process (see section 4.3). The measurements are only performed in the $\mu$-PS (described in chapter 2) with coupling from the top. As shown in Figure 4.6, the top coupling device quantum efficiency[3] of TU/e grown samples are comparable with the films grown in EPFL except that the critical current is lower for the TU/e grown sample. While the $I_c$ of the WSPD fabricated on EPFL grown film is 16.9 $\mu$A, the $I_c$ of the WSPD fabricated on TU/e grown film is only 7.8 $\mu$A in this experiment. The difference in efficiency among the two films (about a factor of less than 3) is in the range of typical variations observed among nominally identical films and devices, and it is therefore not considered significant. Indeed, films grown at the TU/e have been used for the detectors presented in chapter 6 resulting in DQE above 20 % for some devices.

---

[3]The light is not coupled into the waveguide but it is focused on the detectors from the top. Therefore, the efficiencies reported in this particular case are lower than the results presented previously.
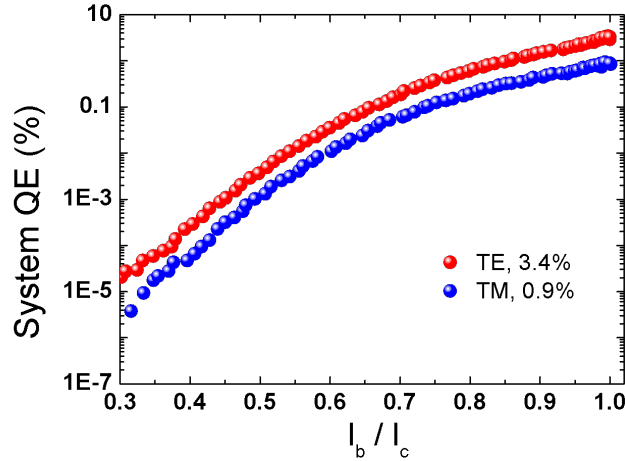
Figure 4.7 – The system quantum efficiency (QE) of a WSPD measured at both TE (red dots) and TM (blue dots) polarisations.

## 4.6 Polarisation dependence of WSPDs

As it has been already mentioned, the WSPDs presented in this chapter are optimised only for the TE polarisation and they are polarisation dependent. Figure 4.7 presents the SQE measured for TE (3.4 %) and TM (0.9 %) polarisations and the efficiency in TM polarisation is lower compared to TM polarisation. It is known that the difference is not due to the absorption (see Figure 4.2) as the modal absorption coefficients in TE polarisation $\alpha_{TE} = 451$ cm$^{-1}$ and TM polarisation $\alpha_{TM} = 391$ cm$^{-1}$ are high and does not support about 4 times high SQE in TE mode.

Figure 4.8 shows the transmission measurement for a waveguide with no NbN nanowire on top, which is performed with a tunable laser working around 1300 nm (from *Hewlett Packard*, 8167A). It is clear that the transmission of the TM polarised light is less than the TE polarised light. That is caused partly by the poor matching of the beam produced by the lensed fiber with the complex field pattern of the quasi-TM mode and must be due to coupling. Moreover, the visibility of the fringes is not constant and that is apparently caused by the beating of the two modes (TE and TM). The beating (with a period of 4.4 nm) is related to periodic power exchange between the two modes. While it is not fully understood the origin of this mode conversion, it is related to the complex polarisation pattern of the TM mode (which has also E-field components in the plane).

In order to get a polarisation-independent coupling efficiency and QE, the WSPD design is slightly modified by increasing the thickness of the GaAs ridge waveguide by 50 nm. This changes the profile of the quasi-TM mode, reducing the in-plane component, as presented in Figure 4.9 (bottom). A nearly equal transmission for the TE and TM polarisations is obtained for a GaAs (350 nm)/Al$_{0.75}$Ga$_{0.25}$As (1.5 $\mu$m) waveguide with a 1.85 $\mu$m-wide,
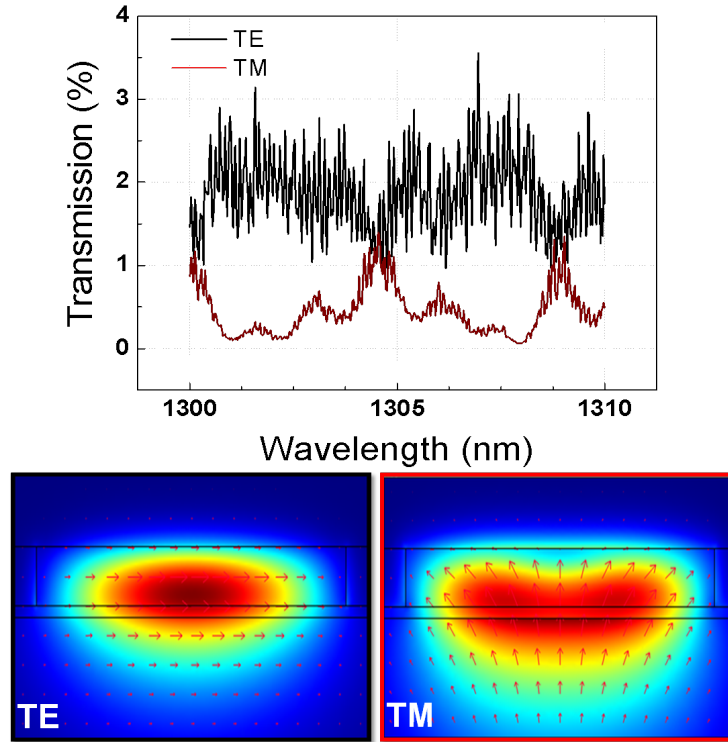
Figure 4.8 – (Top) Transmission spectra of the waveguides used for WSPD design, measured as a function of wavelength in TE and TM polarisations. (Bottom) The corresponding mode profiles for each polarisation mode are given.

300 nm-deep ridge. The modal absorption coefficients of $\alpha_{TE} = 424$ cm$^{-1}$ for the TE mode and $\alpha_{TM} = 574$ cm$^{-1}$ for the TM mode are calculated for a 5 nm-thick NbN wires with the similar dimensions are reported in section 4.2. Additionally, the TE/TM beating is not observed any more (see Figure 4.9 (top))

Figure 4.10 shows the SQE of an autocorrelator detector (see section 5.6) fabricated on the new design. The waveguide is 50 $\mu$m-long and the new design with the given dimensions provides a very high absorptance with a modal absorptance coefficient of $\alpha > 500$ cm$^{-1}$) for both polarisations for a film thickness, t= 5.9 nm. The nearly equal efficiency is assigned to the equal coupling.

## 4.7 Conclusions

Integrated single-photon detectors based on superconducting nanowires are demonstrated on GaAs/AlGaAs material system. These detectors provide a system (device) quantum efficiency of 3.4 % ($\approx$ 20 %) at 1310 nm, a timing resolution $\sim$ 60 ps and a dead time of few ns. Further optimization of the film deposition and the device fabrication is
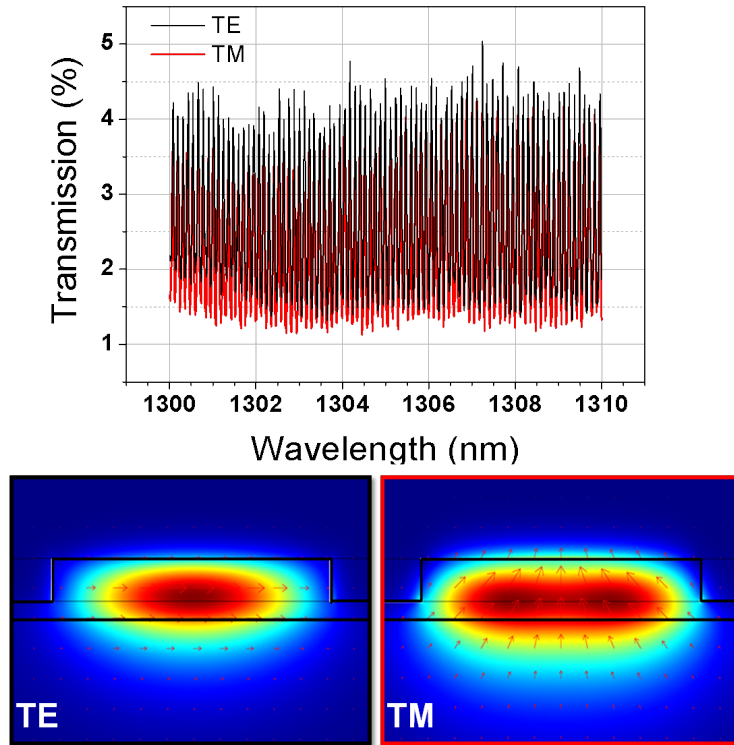
Figure 4.9 – (Top) Transmission spectra of the new design measured as a function of wavelength in TE and TM polarisations. The design is optimised for the polarisation-independent waveguides. (Bottom) The corresponding mode profiles of each polarisation are given.

expected to result in efficiencies approaching 100 % due to the high absorptance allowed by the waveguide geometry. The polarization-independence is obtained by a waveguide design providing a more extended and symmetric mode profile. The WPSDs presented here are fully compatible with the fabrication of the passive quantum circuits on GaAs waveguides, and with single-photon sources based on InAs quantum dots in waveguides. Their realisation on III-V material system makes the scaling of quantum photonics to meaningful number of qubits possible, which has been limited to passive implementations so far. Therefore, WSPDs opens the way to fully integrated quantum photonic circuits.
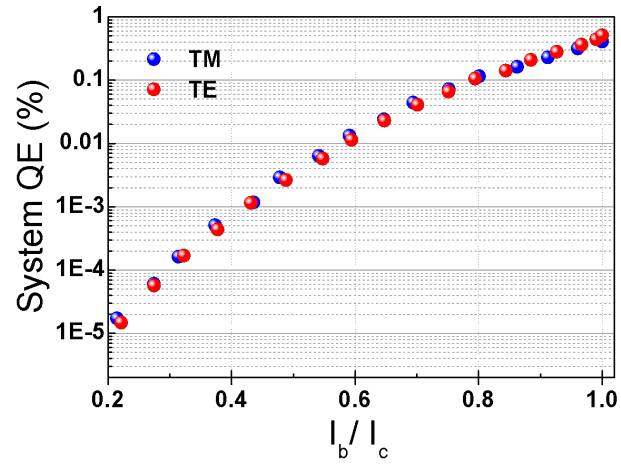
Figure 4.10 – System QE of a 50 $\mu$m-long autocorrelator under illumination at 1300 nm in the TE (red dots) and TM (blue dots) polarization as a function of the normalized bias current.

# Chapter 5

# Integrated Autocorrelators

## 5.1 Introduction

As discussed in detail in chapter 1, advancing the quantum photonics within a QPIC is required to increase the functionality of the photonic circuit. The measurement of the second-order correlation function $g^{(2)}(\tau)$ is a key functionality, allowing for example the characterization of single- and entangled- photon states[22]. The second-order autocorrelation function is usually measured in free space or fiber-optics with a Hanbury-Brown and Twiss (HBT) interferometer[133]. Figure 5.1 shows the configuration of a free-space HBT interferometer for the characterisation of a single-photon source that is based on using a 50:50 beamsplitter and two distinct detectors on the two output arms. $g^{(2)}(\tau)$ is measured by combining the electrical output of the two detectors in a correlation card (counter). Indeed, using two single-photon detectors (SPDs) allows overcoming the dead-time limitation of SPDs. An alternative but equivalent approach is to illuminate two or more detectors with the optical beam under test, as demonstrated in free-space optics using superconducting nanowire single-photon detectors[134].
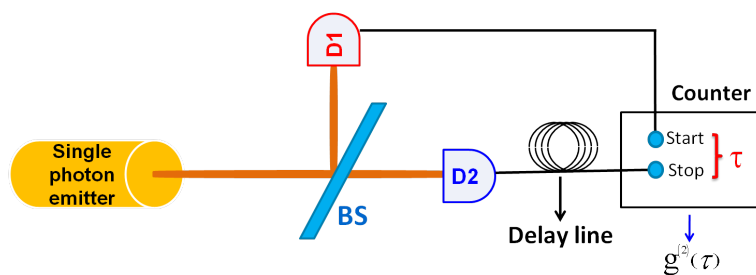


Figure 5.1 – Schematic of the free space Hanbury-Brown and Twiss (HBT) interferometer with two single-photon detectors (D1 and D2), and a counter (correlation card) for the $g^{(2)}(\tau)$ measurements.

This chapter[1] discusses novel devices using similar concepts in an integrated platform which enable the measurement of the $g^{(2)}(\tau)$ with compact integrated devices. These devices are called *integrated autocorrelators*. They are based on two, electrically separated superconducting single-photon detectors (SSPDs), patterned on top of GaAs/Al$_{0.75}$Ga$_{0.25}$ ridge waveguides. Thus, each detector can be referred as a waveguide single-photon detectors (WSPDs) (see chapter 4).

Two different approaches have been pursued in this direction. In the first design, two distinct WSPDs are patterned on each output arm of a multi-mode interference coupler (MMI), where the MMI is optimised for 50:50 splitting ratio, in order to operate as a 50:50 beamsplitter. This type of device is referred as 'waveguide HBT' or WHBT in short in the rest of the text. The MMI is a key building block for integrated photonic circuits as it can split, combine and reroute the photons on a chip. This approach is a straightforward implementation of the $g^{(2)}(\tau)$ measurements on a chip using an MMI instead of a beam splitter and two WSPDs as an integrated counterpart of an HBT interferometer (see Figure 5.1). In the second approach, by simplifying and miniaturising the design, two WSPDs are put on a single waveguide on which both WSPDs sense the same waveguide mode. This device is referred as 'waveguide autocorrelator'. These two approaches, in particular waveguide autocorrelators, enable the measurement of the $g^{(2)}(\tau)$ in a very *compact*, *integrated* device. Besides, the polarization-independent response of the integrated nanowires are reported, which is different than the WSPDs reported in chapter 4. In view of the use of multi-wire structures for waveguide PNRDs (described in chapter 6), a detailed study of the mutual coupling of the nanowires is performed.

This chapter discusses the design, fabrication and experimental demonstrations of integrated autocorrelators. This work is a collaboration between CNR, Rome (group of Dr. R. Leoni), University of Würzburg (UW, group of Prof. M. Kamp and Dr. S. Höfling), University of Bristol (UB, group of Dr. M. Thompson) and Eindhoven University of Technology (TU/e). For both devices, the heterostructures are grown by molecular-beam epitaxy (MBE) at UW by Mr. M. Lermer and the NbN films are grown by DC-magnetron sputtering at the TU/e. The processing has been done in CNR by Dr. A. Gaggero and the waveguides are etched by dry-etching at UW by Mr. J. Beetz. All the low-temperature characterisations have been done at the TU/e. The design of the MMI has been studied and optimised by using FIMMWAVE and first fabrication and characterisation tests are done at UB by Dr. P. Jiang. Dr. G. Frucci for her help in polarisation dependent efficiency measurements of integrated autocorrelators and Dr. T. B. Hoang for his help with the operation of the PicoHarp300 correlation card which is employed for the $g^{(2)}(\tau)$ measurements are acknowledged.

## 5.2 Concept and design

The schematics of the integrated autocorrelators of the both type are shown in Figure 5.2 on a GaAs (0.35 $\mu$m)/Al$_{0.75}$Ga$_{0.25}$As (1.5 $\mu$m) waveguide heterostructure. For the waveguide autocorrelator, there are two pairs of equidistant, electrically-separated NbN

---

[1]The content of this chapter partly appears in Opt. Express 21(9), 11162–11170 (2013) & in Proc. SPIE OPTO 8635, 86351B (2013).

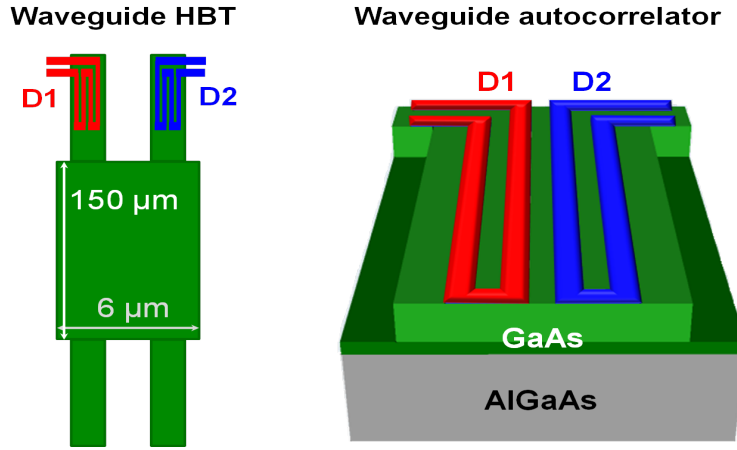**Waveguide HBT**          **Waveguide autocorrelator**



Figure 5.2 – Schematic diagrams of the integrated autocorrelators with two, electrically-separated single-photon detectors (left) one on each arm of a multi-mode interference (MMI) coupler and (right) both on top of the same GaAs ridge waveguide. D1: detector 1 and D2: detector 2. The sketches are not to scale.

nanowires on top of the waveguide, each with a width of 100 nm, a length of 50 $\mu$m and a spacing of 150 nm. On the other hand, the two wires are on the separate waveguides for the WHBT. Each wire is separately connected to a bias and amplification circuit (see the SEM picture in Figure 5.5(right) for a representative image). Thus, the two pairs constitute two independent WSPDs. The detectors exploit the hotspot mechanism for photon detection[48]. A single absorbed infrared photon disturbs the superconductivity and creates a non-equilibrium population of quasi-particles (see the detection mechanism in section 1.4). The resulting perturbation can produce a resistive cross-section in the wire, which diverts the bias current to a parallel load resistor, producing a voltage pulse.

A NxM MMI is a passive circuit element[2], consisting of single-mode waveguides at the inputs (N) and the outputs (M), and a multi-mode waveguide. The field introduced into the MMI at z=0 is defined as,

$$E(x, y, z = 0) = \sum_{\nu=0}^{m-1} C_\nu \phi_\nu(x, y) \qquad (5.1)$$

where $C_\nu$ are the excitation coefficient of the corresponding modes, defined by the integral overlap of the input field and the mode profile, and $\phi_\nu(x, y)$ are the orthogonal modes of the waveguide.

As each mode travels with a different phase velocity, at z$\neq$ 0 the field is the superposition of all the modal fields with different phases,

---

[2]It can also be actively tuned by adding the contact pads in order to tune the phase of the field (E(x,y,z)).

$$E(x, y, z) = \sum_{\nu=0}^{m-1} C_\nu \phi_\nu(x, y) e^{-i\beta_\nu z} \tag{5.2}$$

where $\beta_\nu$ is the propagation constant. The propagation constant depends on the mode number and determines the interference pattern. Depending on the dimensions of the MMI, the relative output from its different ports is determined. In Figure 5.3 (a) the interference pattern is shown for a 2x2 MMI with a dimension of 6$\mu$m-wide and 150 $\mu$m-long. More information on MMIs can be found in Ref. [135].

The WHBT design is optimised for the 50:50 splitting ratio at $\lambda=$ 1550 nm for the MMI in UB using Fimmwave (Fimmprop module) and optimised for the WSPDs at the TU/e using Comsol Multiphysics. For the design, the MMIs of 6 $\mu$m-wide and 7 $\mu$m-wide are studied. In order to achieve a 50:50 (r:t) split for the MMIs with 6 (7) $\mu$m-wide, a length of 159 (213) $\mu$m is required. Moreover, in the simulation the values are tuned around the optimum to estimate the processing tolerance. It is calculated that the tolerance is less for the variations in the width than for the thickness of the waveguide (etching depth). If the etching depth varies $\pm$ 50 nm, the MMI length varies by about $\pm$ 4 $\mu$m if the width changes $\pm$ 15 nm, the MMI length varies by about $\pm$ 9 $\mu$m to obtain a 50:50 splitting ratio in the MMI. The MMI is coupled into two waveguides which are optimised for a high absorptance by the detector. The first test results performed on MMI structures in UB have confirmed the numerical studies.

The detectors are simulated for polarisation-independent mode profiles (see Figure 5.3(b) and (c)) and the thickness of the waveguide and its etching depth are modified slightly as compared to design of the first generation WSPDs (section 4.2). The waveguide dimensions are exactly the same in the waveguide autocorrelators and the WHBT. The only difference is the length of the wires located on the waveguides. For an WHBT, each wire is folded into four and it is 200 $\mu$m-long whilst for a waveguide autocorrelator, each wire is folded into two and it is 100 $\mu$m-long (see Figure 5.1). As the total cross-section of the nanowires and the waveguide is the same for both cases, the total absorptance along a waveguide does not change. Therefore, the design of the detectors is explained in the following over the waveguide autocorrelators.

The symmetric design of the waveguide autocorrelators assures the equal coupling of the waveguide mode with the two pairs of nanowires on top of it. The dimensions of the waveguide and the position of the wires are optimized to obtain polarization-independent coupling efficiency as well as to keep the absorption as high as possible. The GaAs core layer is etched down by 300 nm to create a 1.85 $\mu$m-wide ridge waveguide that confines the quasi-transverse electric (TE) and transverse magnetic (TM) modes as shown in Figure 5.3(b) and (c), respectively.

In the simulations, a 100 nm-thick $SiO_x$ layer is taken into account as a residue of the hydrogen silsesquioxane (HSQ) left on top of the NbN nanowires after the patterning of the nanowires. The modal absorption coefficients calculated with a finite-element solver (Comsol Multiphysics) for the two wires are $\alpha_{TE}=$ 542 $cm^{-1}$ and $\alpha_{TM}=$ 758 $cm^{-1}$ for the lowest-order quasi-TE and quasi-TM modes (assuming a 5.9 nm-thick NbN layer and a refractive index $n_{NbN}=$ 5.23 - 5.82i[71]), respectively. That allows 93 % TE (black solid line) and 98 % TM (red solid line) mode absorptance along a 50 $\mu$m-long waveguide as
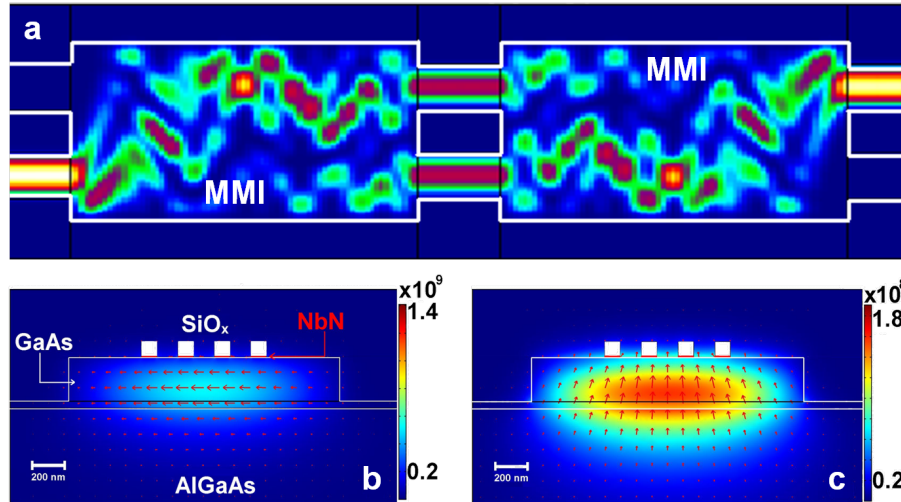
Figure 5.3 – (a) The electric field for the fundamental quasi-TE mode in 7 $\mu$m-wide and 213 $\mu$m-long MMIs at $\lambda=$ 1550 nm. The vector plots of the electric field of 1.85 $\mu$m-wide and 350 nm-thick ridge waveguide at $\lambda=$ 1550 nm for (b) quasi-TE and (c) quasi-TM modes. The white line emphasizes the borders of GaAs, the red line is showing the NbN wires and the white squares are for $SiO_x$. The arrows show the field directions.

shown in Figure 5.4.

## 5.3 Sample preparation

The fabrication steps of both the WHBT and the waveguide autocorrelators are the same except that the detectors are located either on the distinct waveguides or on the same waveguide (see Figure 5.2) and that does not change the process flow. A GaAs /$Al_{0.75}Ga_{0.25}$As heterostructure is grown by molecular beam epitaxy on top of an undoped GaAs (001) substrate. On the GaAs epi-layer, a 5.9 nm-thick NbN superconducting film is grown by a DC magnetron reactive sputtering technique in an Ar + $N_2$ ambient at a nominal temperature of 415 °C with a critical temperature of $T_c=$ 10.1 K and a transition width of $\Delta T_c=$ 0.5 K[72]. The autocorrelators are fabricated using four steps of direct-writing electron beam lithography (EBL). In the first step Ti(10 nm)/Au(60 nm) contact pads (patterned as a 50 $\Omega$ coplanar transmission line) and alignment markers are defined on positive tone PMMA electronic resist by lift-off. In the second step, the meander pattern is defined on a 140 nm-thick HSQ mask. The pattern is then transferred to the NbN film with a ($CHF_3+SF_6+Ar$) reactive ion etching (RIE). The patterning of the NbN nanowires (width of 100 nm, pitch of 250 nm), covered with the HSQ mask, shows very regular width uniformity of about 5 %. In the third step, HSQ-mask is defined for the waveguide etching. This step requires a carefully realigning of this layer with the
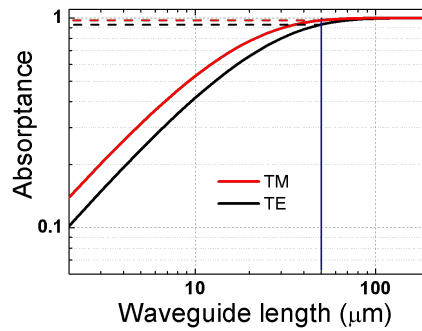
Figure 5.4 – Calculated absorptance of a waveguide autocorrelator with four-wires on a waveguide (see Figure 5.3) for TM (red solid line) and TE (black solid line) polarizations.

previous one. Successively, 300 nm of the underlying GaAs layer is etched with a $Cl_2+Ar$ electron cyclotron resonance (ECR) technique. Finally, in order to allow the wiring to the TiAu electric contacts, holes through the residual HSQ-mask are opened using a PMMA-mask and RIE in $CHF_3$ plasma. The scanning electron microscope (SEM) images of the fabricated integrated autocorrelators are shown in Figure 5.5. The critical current density $J_c$ at $< 4$ K measured varies between 3.4 - 3.9 $MA/cm^2$ for waveguide autocorrelators and between 1.6 - 2.3 $MA/cm^2$ for WHBT for 100 $\mu$m-long nanowires (2x50 $\mu$m).
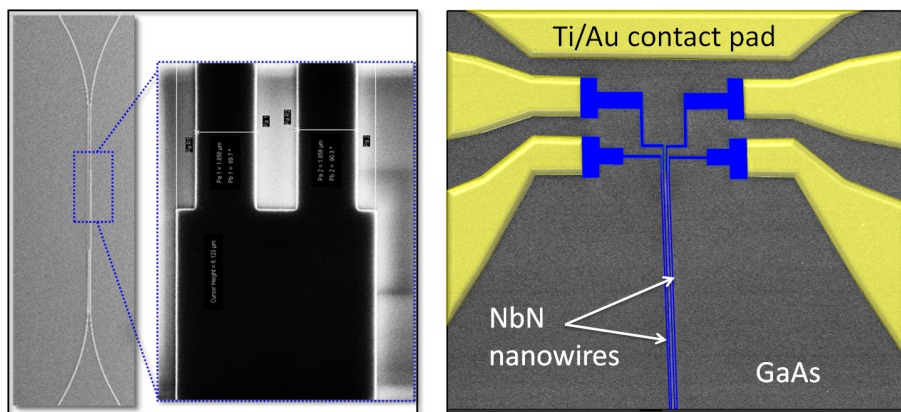


Figure 5.5 – (Left) 2x2 MMI on GaAs chip with its blow-up image on MMI (blue-dotted square) given on the right. (Right) False-colour scanning electron microscope image of two-element waveguide detectors with contact-pads (yellow) and NbN wires (blue).

## 5.4 Setup configuration

The experiments on waveguide autocorrelators are also performed in waveguide-probe station (w-PS, described in subsection 2.2.2) with a base temperature of $T_{base}$= 2.1 K on the sample holder. A lensed fiber with a spot size of $2 \pm 0.5$ $\mu$m is used to couple the light into the waveguide by the end-fire coupling method. The electrical connection to each nanowire is provided by two, identical rf $\mu$-probes, mounted on the piezo towers. Electrical contacts are interfaced to room temperature electronics with 50 $\Omega$-matched feedthrough. The signal is led through a bias tee and amplified either by 60 dB for each of the channels before being sent to the pulse counter or by 45 dB before being sent to the oscilloscope or the time-correlated single photon counting (TCSPC) module for intensity correlation measurements.

## 5.5 Performance of waveguide Hanbury-Brown and Twiss

The detectors are first characterised in terms of their current-voltage (IV) characteristic curves. Two detectors show similar IV behaviours with a critical current of $I_c^{D1}$= 9.1 $\mu$A and $I_c^{D2}$= 8.6 $\mu$A as given in Figure 5.6 at the measurement base temperature.
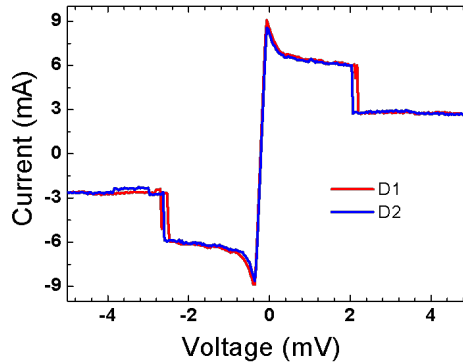


Figure 5.6 – Current-voltage (IV) curve of the two detectors (D1 and D2) on two output arms of an MMI.

Figure 5.7 shows the system quantum efficiency (SQE) of the detectors D1 and D2 measured using a continuous-wave laser at 1300 nm in the TM polarization. The two detectors show very similar efficiency versus bias current dependences, and the peak QE value reaches to 0.28 % (D1) and 0.25 % (D2) at their maximum bias currents, and measured $\sim$ 0.15 % at $I_b$= 7.5 $\mu$A for both. The slightly lower efficiency of D2 is due to its slightly lower $I_c$ as compared to D1. The SQE of two detectors are fully overlapping. The efficiency measurement is repeated for each input waveguides of the MMI (R (right waveguide input) and L (left waveguide input) see Figure 5.8) and they are shown for
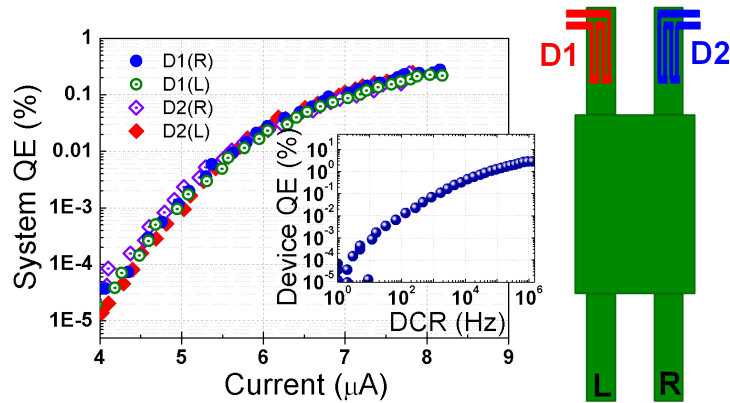
Figure 5.7 – (Left) System quantum efficiency (SQE) of each detector measured with TM-polarized CW light at 1300 nm. The different overlapping curves corresponds to detector 1 (D1) and detector 2 (D2) for the light coupled from the input L and R (see Figure 5.8). Inset plot: Device QE of D1 as a function of dark count rate (DCR) for the light coupled from the right input of the MMI D1(R). (Right) Sketch of an MMI with two input arms (R and L) and two detectors (D1 and D2).

both detectors in the plot that the two results are the same for the light coupled from each input. The SQE value has been derived by dividing the number of counts (after subtracting the dark counts) by the number of photons coupled to the system.

It has been noted that the nearly equal values of the SQE of D1 and D2 do not, in principle, guarantee that the detectors have equal performance since the SQE is also influenced by the splitting ratio of the MMI, which may be different than 50:50 in this particular device. Therefore, the SQE measurements in Figure 5.7 are used to separately determine the efficiency ratio and the splitting ratio in the following.

As the MMI is the equivalent of the beam splitter, it is treated in the same way in order to determine the splitting ratio of the MMI. For a configuration given in Figure 5.8, the SQE of any detector can be written in terms of the detector efficiencies is given by $\eta_1$ or
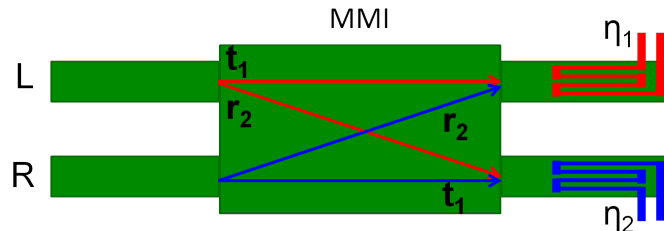


Figure 5.8 – Schematic diagram of the device layout with the coupling scheme and the measurements of efficiency. Light is coupled from the input arms (L and R) and either transmitted from the bar port (t) or the cross port (r) (where r=1-t).

$\eta_2$ for D1 and D2, respectively. Then, SQE can be written as,

$$SQE_1^L = e^{-\alpha\Lambda}\eta_1^L t_1 \qquad (5.3)$$

$$SQE_1^R = e^{-\alpha\Lambda}\eta_1^R r_1 \qquad (5.4)$$

$$SQE_2^L = e^{-\alpha\Lambda}\eta_2^L r_2 \qquad (5.5)$$

$$SQE_2^R = e^{-\alpha\Lambda}\eta_2^R t_2 \qquad (5.6)$$

where the superscripts indicate the coupling at the waveguide input of the light, right (R) and left (L) while the subscripts are assigned to the detector (1: D1 and 2: D2). $\alpha$ is the loss coefficient and assumed to be the same for all, $\Lambda$ is the propagation length, $r_1 = r_2 = r$, $t_1 = t_2 = t$ (see also Figure 5.8) and $\eta_1^L = \eta_1^R$.

If the ratio of SQE$_1$s is taken,

$$\frac{SQE_1^L}{SQE_1^R} = \frac{\eta_1^L t}{\eta_1^R r} \qquad (5.7)$$

where r= 1-t.

At a bias current I$_b$= 8.0 $\mu$A, $SQE_1^L/SQE_1^R$= t/(1-t)= 0.23/0.24= 0.958 is calculated. By applying the same ratio as in eqn.5.7 for D2 at I$_b$= 7.4 $\mu$A, $SQE_2^L/SQE_2^R$= (t/(t-1))$^{-1}$= (0.24/0.25)$^{-1}$= 1.04 (t/(t-1)= 0.96) is obtained. That number agrees very well with the one obtained from D1 and they are both very close to 1. That shows that the MMI does have a slight unbalance between two arms but it is only 0.2 % off from 50:50 splitting ratio.

From eqn.5.3-5.6, the efficiency ratio of any couple can also be calculated. For instance, at I$_{b1}$= I$_{b2}$= 7.5 $\mu$A an SQE of 0.16 and 0.15 is measured for the D1 and D2, respectively and that corresponds to $\eta_1/\eta_2$= 1.07. In order to confirm the equal efficiencies in this MMI, the detectors are measured by top-coupling in a free-space configuration and a system quantum efficiency of 8.3x10$^{-5}$ and 5.4x10$^{-5}$ are measured for the same bias current (I$_b$= 7.5 $\mu$A), respectively. This further confirms that the detectors are nearly equally efficient and the MMI splitting ratio is close to 50:50 in this WHBT.

After showing the 50:50 splitting, the device quantum efficiency (DQE) has been reported for both detectors as $\sim$ 2 % at I$_b$= 7.5 $\mu$A (not shown). It has been derived by dividing the number of counts (after subtracting the dark counts) by the number of photons coupled to the input waveguide, taking into account the measured coupling efficiency $\eta_{TM}$= 19 % for the quasi-TM mode and the equal splitting ratio. Coupling efficiencies are determined by measuring the spectral fringes in the transmission spectra of test waveguides without NbN nanowires as described in subsection 2.2.2. The dark count rate is relatively high as given in the inset of Figure 5.7 ($\sim$10 kHz for 1 % DQE) in this measurement set-up. However, that is due to the non-ideal temperature and infrared background radiation but it can be reduced to <10 Hz by lowering the temperature to $\sim$1 K and better shielding of the infrared background (see section 2.2).
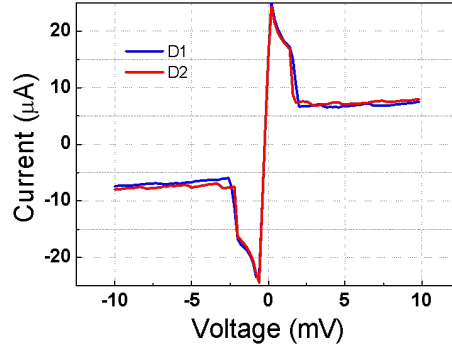
Figure 5.9 – Current-voltage (IV) curve of the detectors (D1 and D2) on the same waveguide.

## 5.6 Performance of waveguide autocorrelators

Now, the performance of the waveguide autocorrelators are presented (see Figure 5.2(right)). As depicted in Figure 5.9, the detectors have a critical current $I_c$= 23 $\mu$A with a very similar IV curves at $T_{base}$= 2.1 K.

The electro-optical response to a continuous wave (CW) 1300 nm diode laser is measured for each element of the autocorrelators. In order to prove that the detectors respond to the single photons, the count rate is measured to be proportional to the laser power as shown in Figure 5.10. The inset in Figure 5.10 shows a voltage output of D1 (representing the pulse shape for a 50 $\mu$m-long detector), with a 1/e pulse decay time of 1.5 ns. This value is approximately in agreement with the calculated value $\tau_{1/e} = L_{kin}/R_{out}$= 1.8 ns[85], based on the kinetic inductance per square reported ($L_k$= 90 pH/$\square$[132]). The difference is assigned to the different film thicknesses which is higher for these detectors as compared to the Ref.[132] and the kinetic inductance decreases inversely with the thickness. Considering that it takes $3\tau$ to recover the bias current to its 95 % after a detection event, a maximum count rate of $>$ 200 MHz is estimated. The short recovery time of the waveguide autocorrelator as the WHBT shows the advantage of integrating two wires on top of the same waveguide.

Figure 5.11 shows the device quantum efficiency (QE) of both detectors measured using a continuous-wave laser at 1300 nm in the TE polarization. The two detectors show very similar QE vs bias current dependences at high-bias currents, and the peak QE value reaches to 0.5 % (D1) and 0.9 % (D2) at $I_b$= 0.99$I_c$. This value has been derived by dividing the number of counts (after subtracting the dark counts) by the number of photons coupled to the waveguide, taking into account the measured coupling efficiency $\eta$= 16.6 % and 19 % for the quasi-TE and quasi-TM modes, respectively. Coupling efficiencies are determined by measuring the spectral fringes in the transmission spectra of test waveguides without NbN nanowires as described in subsection 2.2.2. The dark count rate (not shown) is relatively high ($\sim$80 kHz at $I_b$= 0.95$I_c$) but it can be reduced
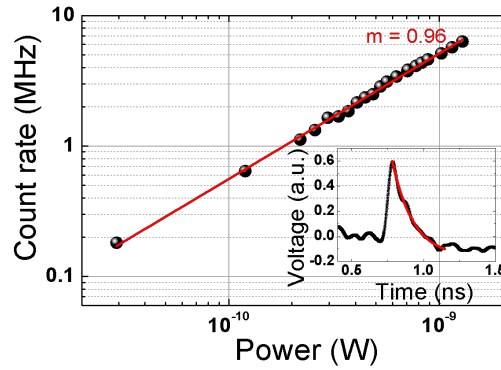
Figure 5.10 – Count rate (dots) as a function of laser power at 1300 nm for a 50 $\mu$m-long detector, TE polarization and bias current $I_b = 0.98I_c$ and a linear fit (red line) in log-log scale with a slope of 0.96. Inset: A voltage output of a single detector, D1, and exponential fit (red line) with a decay time $\tau_{1/e} = 1.5$ ns.

to $<100$ Hz at $I_b = 0.95I_c$ by lowering the temperature to $\sim$1 K and better shielding of the infrared background[29].

Moreover, as shown in Figure 5.12, the detectors are polarization-independent which can be attributed to the very high absorptance of the 50 $\mu$m-long wires for both polarizations and to the very initial coupling efficiencies. The relatively low value of the device QE (of both the waveguide autocorrelator and the WHBT), despite the high absorptance, is attributed to the limited internal QE (ratio of detected to absorbed photons) as also indicated by the unsaturated bias dependence of the DQE. This is probably related to the
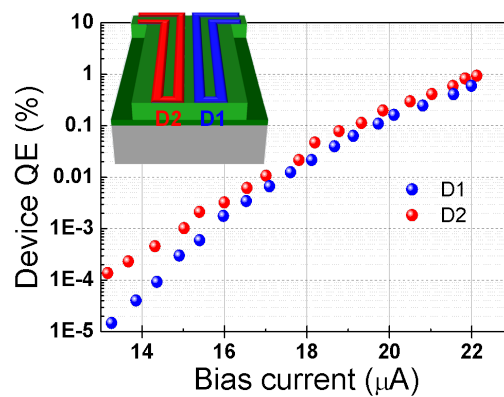


Figure 5.11 – Device quantum efficiency of each detector measured with TE-polarized CW light at 1300 nm (TE mode). The sketch shows the locations of the detectors.
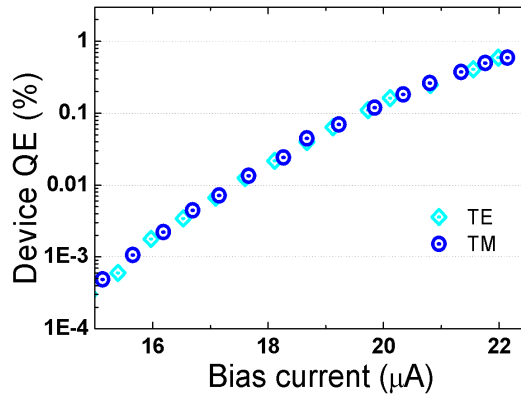
Figure 5.12 – Device QE of detector D1 (see Figure 5.11 for D1) for TE and TM polarizations at 1300 nm.

film thickness (5.9 nm), larger than the conventional thickness used in nanowire detectors (4-5 nm). Moreover, the quality of this NbN film is also not optimized, as indicated by the $T_c$, lower than previous demonstrations of NbN SSPDs on GaAs[72]. It is anticipated that the QE may also be increased using narrower wires[32,66].

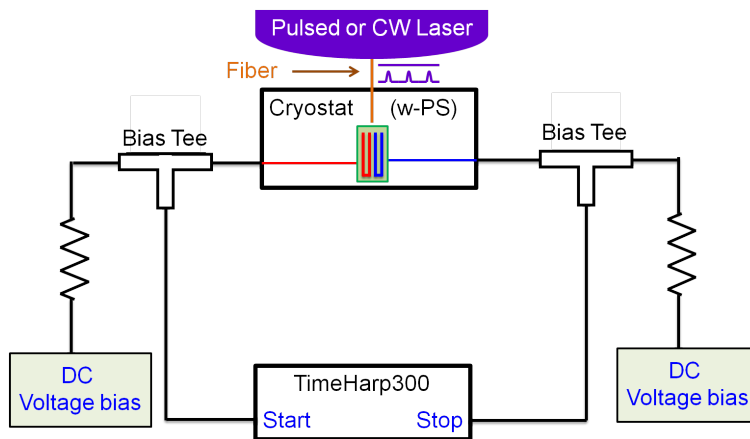## 5.7  Crosstalk analysis of waveguide autocorrelators



Figure 5.13 – Sketch of the measurement setup with the waveguide autocorrelator for the $g^{(2)}(\tau)$ measurements.

The close packing of the nanowires, needed to ensure equal coupling to the guided light

and high absorptance, may produce electrical, magnetic or thermal coupling between the two detectors. That potentially leads to either a false detection or a decreased detection probability in one wire after the other has fired. Such coupling, which is referred to as crosstalk in the following, would introduce spurious correlations at and around zero delays and affect the measurement of the second-order correlation function. In an ideal autocorrelator, the detectors should work independently without causing any modified/ false response arising from the firing adjacent detector[134,136]. Therefore, it is of utmost importance to investigate any possible crosstalk-related limitation of the waveguide auto-correlator.

Several tests are performed in order to investigate the possible crosstalk between two adjacent detectors on a single ridge waveguide. A first series of tests is performed in static conditions, to determine whether the bias condition of one detector has an influence on the electro-optical response of the other. The second series is in dynamic conditions in order to investigate any temporal variation of the detection probability of one detector due to the firing of the other detector. The dynamic analysis of the detectors is performed by measuring the intensity correlation function $g^{(2)}(\tau)$ of both CW (1310 nm) and pulsed lasers (1064 nm) coupled to the waveguide. The setup used for the measurement is given in Figure 5.13. Both detectors are biased with identical electrical bias-circuit configuration.

## 5.7.1 Static crosstalk analysis

Static coupling would mainly result from the thermal or magnetic interaction (intrinsic) as well as the coupling of two detectors due to the shared ground (extrinsic). The electrical and optical response of one detector is studied as a function of the bias of the adjacent detector. Figure 5.14(a) shows the IV characteristic of D1 (see Figure 5.11) while D2 is unbiased. Figure 5.14 (b) and Figure 5.14 (c) show the IV characteristics of D2 measured with D1 biased at the points indicated with the open squares in Figure 5.14 (a). In Figure 5.14 (b), all the curves are superposed whilst in the blow-up of Figure 5.14 (c) only small fluctuations ($\sim 0.10~\mu$A) in the critical current are observed and reported in Figure 5.14 (d) as a function of the bias voltage of D1. It can be seen that even when the neighbouring detector D1 becomes resistive, where it dissipates Joule heating to the GaAs lattice, no change of the Ic of D2 is observed within the uncertainty (0.2 %) due to stability of the experiment (see Figure 5.14 (d)). The same behaviour is observed when sweeping the bias voltage of D2 while measuring the IV for D1. Therefore, no static coupling between the detectors is evidenced. This is different than the results obtained on sapphire[134] where biasing one detector in the resistive state led to a 10 % decrease in the critical current of the other detector. This may be related to the higher thermal conductivity of GaAs with respect to sapphire, leading to an efficient heat transport to the substrate.

Similarly, considering the fact that the dark count rate (DCR) is very sensitive to any change, the DCR was measured for the detector D1 at several bias conditions by sweeping the bias of D2 in the superconducting and unstable region (green dots and black stars in the inset of Figure 5.15 that shows the IV curve of D2 when amplifiers are connected). If switching of D2 resulted in any false counts on D1, the dark count rate of D1 would change when D2 is biased in the unstable region. Figure 5.15 shows the DCR of D1, biased
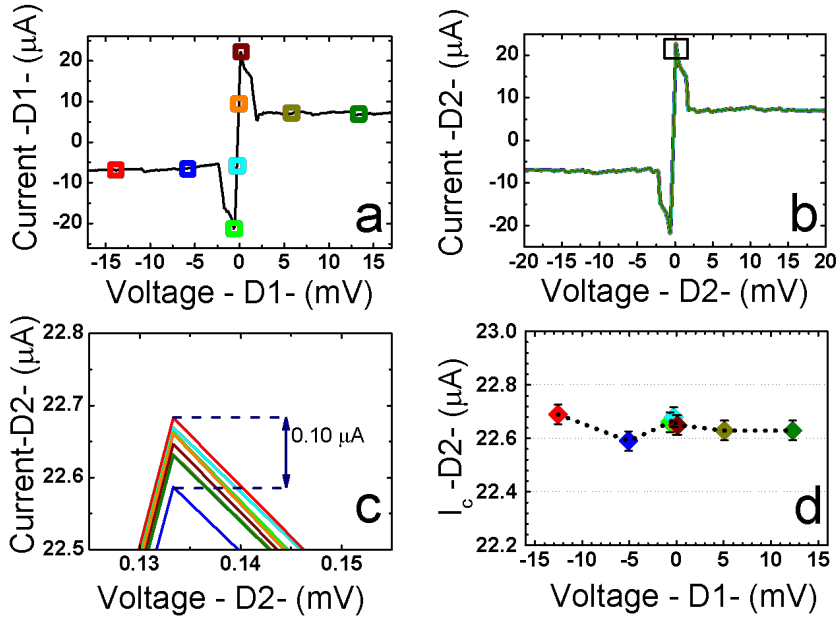
Figure 5.14 – (a) IV curve of the detector D1 while D2 is unbiased (see Figure 5.11 for D1 and D2). (b) IV characteristic of the detector D2 at different bias conditions of D1. (c) IV curve of D2, zoomed around Ic, each curve corresponds to the bias points indicated with a square of the same colour in Figure 5.14(a). (d) Fluctuations in Ic of D2 while D1 is biased at several different bias conditions. The Ic is independent of the bias voltage of D1 within the error bars.

at constant current Ib= 0.95-0.99$I_c$ while the bias of D2 is swept. There is no measurable variation of the DCR with the bias of the other detector. That confirms that there is no measurable static coupling between two integrated WSPDs.

## 5.7.2 Dynamic crosstalk analysis and second-order intensity correlation measurement

As a coherent beam has a constant $g^{(2)}(\tau)$[3], any variation observed at small delays would indicate a spurious increase or decrease of the detection probability upon firing of the adjacent detector. The expected time range for crosstalk is within a few ns delay because the relevant timescales are the time for the formation and the decay of the hotspot (tens of ps)[60,137] the recovery time of the detector ($\sim$5 ns)[29], the electromagnetic wave travelling time between the nanowires and along the waveguide ($<$1 ps) as well as the propagation time of phonons across the entire detector length and between the adjacent pairs (up to a few ps).

---

[3]$g^{(2)}(\tau)$= 1 for a coherent beam and $g^{(2)}(0)$= 0 for any single-photon source.
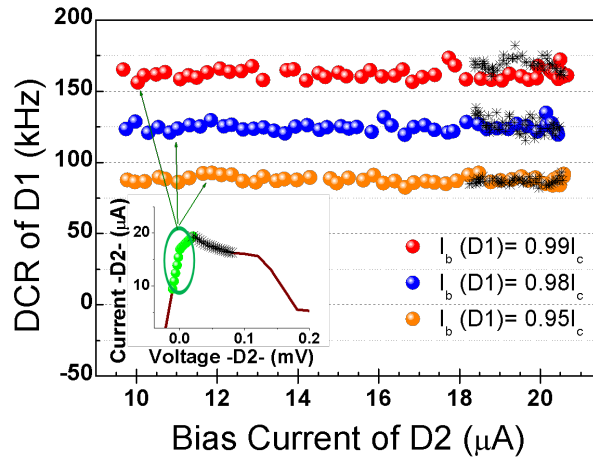
Figure 5.15 – Measured intensity correlation histograms for a 1300 nm CW laser with 77 pW excitation power. The detectors are biased at 99 % (green line) and 97 % (blue line) of their critical current. The black lines show the averaging of the data over 1 ns..

The coincidence counts between the two detectors are measured by sending their outputs to the inputs of a correlation card (PicoHarp 300). The zero delay is calibrated in a subsequent experiment by measuring the zero-crossing of a single detector, using the same delay line. In Figure 5.16, the coincidence counts are shown as a function of the delay time between the start and the stop channels for a CW light with an excitation power of 77 pW at 1300 nm at $I_b= 0.97I_c$ (blue line) and $I_b= 0.99I_c$ (green line). The change in the bias current modifies the number of coincidences due to the varying efficiency of the detectors (see Figure 5.11). In order to improve the signal to noise ratio and to clearly observe the coincidences around zero delay, the data is averaged over a 1 ns temporal window (black lines). Even when the bias current of each detector is brought very close to $I_c$, no trace of crosstalk has been observed in the vicinity of zero delay.

As a further test, the same experiment is carried out with a pulsed laser at 1064 nm and with 5.6 ps-long pulses and a $63 \pm 0.5$ MHz repetition rate. Figure 5.17 presents the coincidence rate as a function of time delay, measured at varying bias conditions of the two detectors. The detectors are biased with a current from $0.95I_c$ to $0.99I_c$ and data is collected for long enough to provide a high number of coincidences for the analysis and then divided by integration time to obtain the coincidence rate. In this situation, coincidences are observed only at delays multiple of the repetition period of the laser ($15.9 \pm 0.1$ ns). The total coincidences with a 2 ns ($\pm 1$ ns for each side) time window around each peak are calculated and shown in Figure 5.17 on the right axis and fitted with a linear curve (dashed lines). The linear fit is an approximation for the exponential decay due to the expected saturation of the coincidences vs delay, related to the relatively high
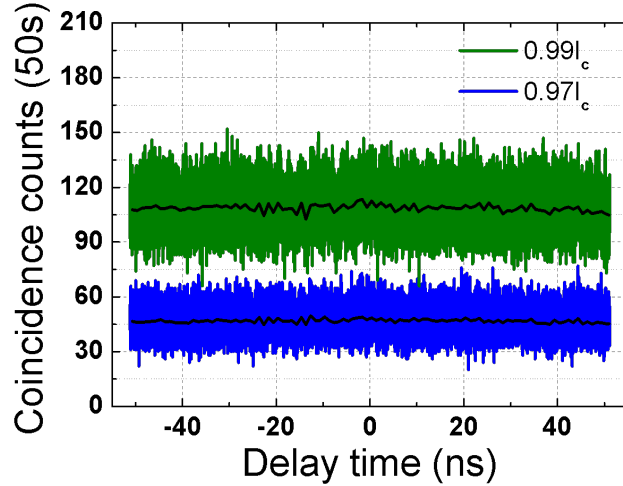
Figure 5.16 – Measured intensity correlation histograms for a 1300 nm CW laser with 77 pW excitation power. The detectors are biased at 99 % (green line) and 97 % (blue line) of their critical current. The black lines show the averaging of the data over 1 ns..

count rate in this experimental condition. In order to estimate the error bar the standard deviation of the data points are calculated at delays different than zero with respect to the value given by the linear fit. For all currents, the measured coincidences at zero delay fall within the expected interval as defined by the linear fit and the error bar, showing the absence of crosstalk within the experimental accuracy of maximum of $\sim$4 % at 0.97 - 0.99$I_c$.

Finally, the timing resolution (jitter) can be determined from the second-order intensity correlation measurements on a pulsed laser ($\lambda=$ 1064 nm, $\sim$6 ps-wide pulse width). Figure 5.18 displays the coincidence peak at the zero delay for two different bias currents ($I_b=$ 0.90$I_c$ (red diamonds) and $I_b=$ 0.99$I_c$ (blue circles)), showing a Gaussian distribution with a full-width-half-maximum (FWHM) of 125 ps. The jitter is the convolution of all the jitters in the measurement set-up. As the jitter of the laser and the correlation card are negligible as compared to the detectors, only the two detectors are considered with an equal timing jitter (amplifiers and the cabling are not excluded)[138]. A jitter of 88 ps (FWHM) is obtained for each detector with no change depending on the bias current within the accuracy of the experiment.

It is possible that the time resolution of the HBT may impact the measured-dip of a single-photon emitter at $g^{(2)}(0)$. If the time resolution of an HBT is lower than the decay time of the single-photon emitter (in the order of ns), $g^{(2)}(0)$ will not go to zero. However, as the waveguide autocorrelators have a sub-ns jitter time with a Gaussian distribution, no artefact is anticipated.
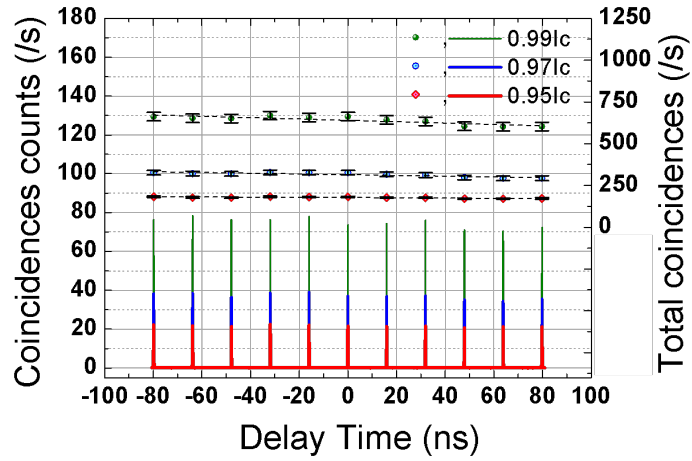
Figure 5.17 – Left axis: Coincidence rate under illumination with a 63 MHz pulsed laser at 1064 nm with an average power of 34 pW. The detectors are biased at 0.99 (green line), 0.97 (blue line), and 0.95 (red line) of the critical current. Right axis: Total coincidence rate at each peak points (integrated over the peak, $\pm$ 1 ns). The black dash lines are linear fits to the data.
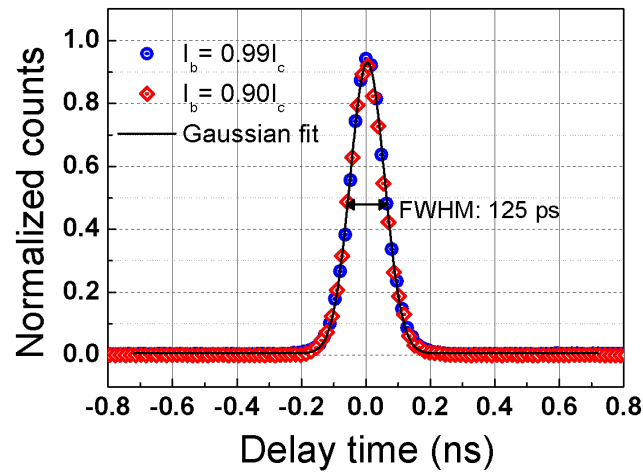


Figure 5.18 – Histogram of the jitter time of one detector relative to the other for two different bias conditions; $0.90I_c$ (red diamonds), $0.99I_c$ (blue circles) and the Gaussian-fit to the data (black solid line).

## 5.8 Conclusions

The measurement of the second-order correlation function $g^{(2)}(\tau)$ and of the photon number is a key functionality for quantum photonics, allowing for example the characterization of single-photon states. To this aim, the first waveguide autocorrelators have been demonstrated by exploiting two different designs, WHBT and waveguide autocorrelators. As discussed widely in the text, waveguide autocorrelators are also studied for crosstalk in both static and dynamic regimes. No crosstalk has been evidenced within the measurement accuracy, which makes them promising candidates for on-chip autocorrelators. That allows successfully performing on-chip second-order intensity correlation measurements. As a proof of principle, the $g^{(2)}(\tau)$ of CW and pulsed light sources is measured with total temporal resolution of 125 ps (FWHM). Moreover, the detectors are shown to be polarization independent. These waveguide autocorrelators are also the first step towards integrated photon number resolving (PNR) detectors which could be realized by connecting the different wires together in a parallel[79] or series[87] configuration, which is discussed in detail in the following chapter. The absence of crosstalk is an essential feature for PNR detectors whose fidelity would otherwise be affected.

# Chapter 6

# Waveguide Photon–Number–Resolving Detectors

After demonstrating waveguide detectors with single-photon capability in chapter 4 and the waveguide single-photon detectors with more functionality such as autocorrelators in chapter 5, the last missing piece of the puzzle is the photon-number-resolving detectors which is presented in this chapter.

## 6.1 Introduction

Whilst integrated single-photon detectors are powerful components for a QPIC, detectors providing photon-number resolution are important in quantum communication and linear-optics quantum computing[139]. Recently, there has been a considerable effort to realize photon-number-resolving detectors (PNRDs) for free-space coupling using the transition-edge sensors (TESs)[92], silicon photomultipliers[90] and avalanche photodiodes (APDs)[45], as well as time-multiplexing using Si-APDs[89] and SSPDs[88], and spatial multiplexing with APDs[140] and SSPDs[77,79,86,87,141]. Up to date, only transition-edge sensor PNRDs have been reported in a waveguide configuration[92,93]. Nevertheless, TESs are thermal detectors therefore they are relatively slow and unsuited for high-speed quantum information processing.

This chapter[1] describes the experimental results of waveguide photon-number-resolving detectors (WPNRDs) on GaAs/$Al_{0.75}Ga_{0.25}$As ridge waveguides based on a series connection of nanowires. The detection of 0-4 photons has been demonstrated with a four-wire WPNRD, having a single electrical read-out. By combining the benefits of the superconducting nanowires such as low dark count rates, excellent timing resolution and short

---

[1]The results in this chapter have been partly published in Appl. Phys. Lett. 103, 111116 (2013)

dead time[48] and benefits from the high modal absorption of the guided mode that allows unity absorptance with waveguide lengths of a few tens of micrometers, a WPNRD with a device quantum efficiency $\sim$24 % and 22% has been reported at 1310 nm for the TE and TM polarisations, respectively.

The work is a collaboration of CNR, Rome (group of Dr. R. Leoni), Würzburg University (WU, group of Prof. M. Kamp and Dr. S. Höfling) and Eindhoven University of Technology (TU/e). The films are grown at the TU/e, the processing has mainly been done in CNR by Dr. A. Gaggero and Dr. F. Mattioli except for the waveguide etching, which is done at WU. The sample then goes back to CNR in order to open the vias for the probing. It has been measured and characterised in TU/e. The contributions of Mr. Z. Zhou for sharing his experience on PNRDs in the lab is also acknowledged.

## 6.2 Concept and design

Figure 6.1 shows a schematic of a waveguide photon-number-resolving detector (WP-NRD). The detector is based on four NbN superconducting nanowires on top of a GaAs/Al$_{0.75}$Ga$_{0.25}$As (0.35 $\mu$m/1.5 $\mu$m-thick) waveguide heterostructure. The nanowires represent distinct detecting elements sensing different parts of the same waveguide mode and the number of switching wires can be determined from the output voltage as described below. A 3.85 $\mu$m-wide and 350 nm-thick ridge GaAs waveguide with an etching depth of 260 nm on top of Al$_{0.75}$Ga$_{0.25}$ (cladding layer) is simulated with a finite-element solver (Comsol Multiphysics). The wires are 5 nm thick and 100 nm-wide with a spacing of 150 nm and a total length of 60 (2x30) $\mu$m as shown in Figure 6.1. In the simulation, a 100 nm-thick SiO$_x$ layer is taken into account left as a residue of the hydrogen silsesquioxane (HSQ) resist on top of the NbN nanowires after the patterning (see Figure 6.2). The structure is optimized for nearly-equal absorption by the different wires along the lateral direction of the waveguide. The symmetric configuration with a wider waveguide than WSPDs[29] is appropriately engineered to alleviate the difference in the absorption of the guided light by the central and lateral wires, while maintaining the absorptance of the quasi-transverse electric (TE) and transverse magnetic (TM) modes high (see Figure 6.2). Moreover, the design is tolerant to the variation of the etching depth between 250 and 300 nm.

The total absorptance for the lowest-order TE and TM modes is calculated with the respective modal absorption coefficients of $\alpha_{tot}^{TE} = 478$ cm$^{-1}$ and $\alpha_{tot}^{TM} = 654$ cm$^{-1}$ (assuming n$_{NbN}$ = 5.23 - 5.82i[71]) and plotted in Figure 6.3. As depicted in the figure, that allows 76 % TE and 86 % TM absorptance along a 30 $\mu$m-long waveguide. The modal absorption coefficient by only the two central wires $\alpha_{cent}^{TE} = 282$ cm$^{-1}$, $\alpha_{cent}^{TM} = 380$ cm$^{-1}$ is higher than the corresponding absorption by the two lateral wires $\alpha_{lat}^{TE} = 198$ cm$^{-1}$, $\alpha_{lat}^{TM}$ = 276 cm$^{-1}$ for both polarisations due to the confinement profile of the mode as shown in Figure 6.2. The probability of absorption after propagating over a length L (P(L)) for central (P$_{cent}$) and lateral (P$_{lat}$) wires is easily derived as,

$$P_{cent(lat)}(L) = \frac{\alpha_{cent(lat)}}{\alpha_{tot}}(1 - e^{-\alpha_{tot}L}) \tag{6.1}$$

and it is plotted for both TE and TM polarisations for the two central (circles) and

Figure 6.1 – Schematic of a waveguide photon-number-resolving detector (WPNRD) consisting of four wires in series with a resistance ($R_p$) in parallel to each wire (contact pads are not shown).

lateral (diamonds) wires in Figure 6.3. The situation is analogous to an imbalanced N-port splitter[142] followed by single-photon detectors. The corresponding unbalance in detection probability does not significantly limit the fidelity of the PNR measurement, as discussed later in this chapter.

The electrical structure of WPNRDs is based on the series connection of four wires, each shunted by a resistance (see Figure 6.1 for the sketch and Figure 6.4 for the circuit diagram)[77]. The photon detection mechanism in each wire is the same as in SSPDs[48]. The wire is biased with a current close to its critical current ($I_c$), and upon absorption of a single photon, a resistive region is formed across it. While in SSPDs the bias current ($I_b$) is diverted to the external load resistance, in these series-nanowire detectors $I_b$ is redirected to the resistance integrated in parallel to each wire, producing a voltage pulse. The circuit diagram in Figure 6.4 depicts the equivalent electrical circuit (showing only two wires for simplicity). Each wire can be modelled as a variable resistance ($R_n$) and an inductance (kinetic inductance, $L_k$) and it is connected in parallel to an integrated resistance ($R_p$) and in series to the other wires. If several wires switch simultaneously, a voltage approximately proportional to the number of switching wires is read on the load resistance[77].

## 6.3 Sample fabrication

WPNRDs integrated on a GaAs waveguide are defined using five steps of direct-writing electron beam lithography (EBL). A high resolution Vistec EBPG 5HR system equipped with a field emission gun with acceleration voltage 100 kV is used for EBL. In the first step, Ti(10 nm)/Au(60 nm) electrical contact pads (patterned as a 50 $\Omega$ coplanar transmission line) and alignment marks are defined using a positive tone polymethyl methacrylate
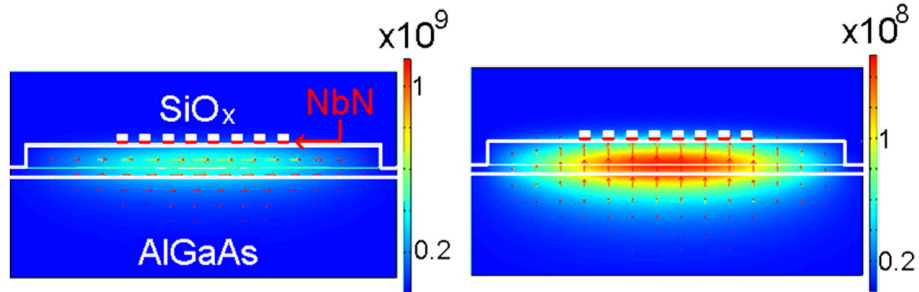
Figure 6.2 – Vector plots of the electric field for the fundamental (left) quasi TE mode and (right) quasi TM mode of the WPNRDs at $\lambda$=1300nm. The nanowires sensing the same mode of the waveguide do not introduce any perturbation to the travelling mode. Red arrows show the electric field direction. In order to guide the eye, white lines are drawn around the GaAs layer and white squares and red lines for $SiO_x$ and NbN wires, respectively.

(PMMA) electronic resist, evaporation and lift-off. In the second step, additional Ti (5 nm)/Au (20 nm) pads are defined by electron beam lithography on PMMA, evaporation and lift-off. These pads are needed to allow the electrical connection between the nanowires and the parallel resistances ($R_p$, light green-coloured pads in the inset (right) of Figure 6.5). In the third step, the 100 nm-wide meandered nanowires are defined on
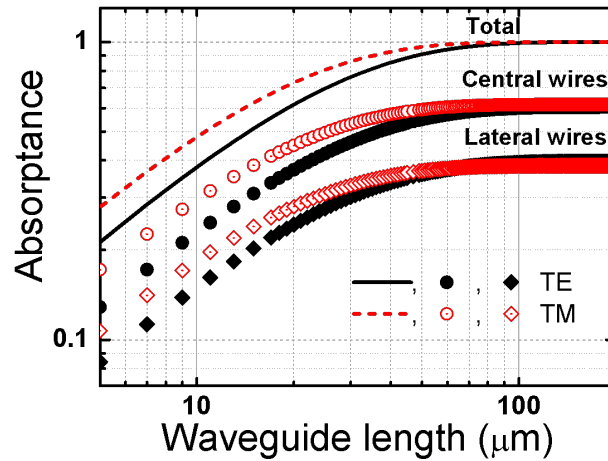


Figure 6.3 – Calculated absorptance of a WPNRD for TM (red, dashed line and empty symbols) and TE (black, continuous line and filled symbols) polarisations. The absorptance is calculated for the four wires (lines), the two central (circles) and the two lateral wires (diamonds).

a 140 nm-thick HSQ mask using an e-beam process optimized for GaAs substrates. The pattern is then transferred to the NbN film with a $(CHF_3 + SF_6 + Ar)$ reactive ion etching. The left inset of Figure 6.5 shows a scanning electron microscope (SEM) image of nanowires. In the fourth step, the Ti(10 nm)/AuPd(50 nm) resistances are fabricated. Each resistance is 500 nm-wide and 3.5 $\mu$m-long corresponding to a design value of $R_p$= 49 $\Omega$. The right inset in Figure 6.5 shows a magnified micrograph of the resistances. In the next step, the 180 nm-thick and 3.85 $\mu$m-wide HSQ mask is defined for the waveguide patterning by carefully realigning this layer with the previous one. This layer also protects the Ti/Au pads and the Ti/AuPd resistances during the GaAs etching process. Successively, 260 nm of the underlying GaAs layer is etched with a $Cl_2 + Ar$ electron cyclotron resonance etching. Finally, to allow probing the pads, holes are opened in the HSQ layer using a PMMA mask and reactive ion etching in $CHF_3$ plasma.

## 6.4 Results and discussions

The experiments are performed by end-fire coupling near-infrared light from a lensed fiber to the waveguide, using the waveguide probe station as described in subsection 2.2.2. Figure 6.6 shows a characteristic current-voltage (IV) curve of a four-wire WPNRD. A critical current of $I_c$= 10 $\mu$A is measured at the base cold-plate temperature T= 2.1 K. The linear slope observed in the IV curve after reaching $I_c$ is related to the series connection of the four resistances, $4 \times R_p$= 152 $\Omega$ (38 $\Omega$/each). There is a sharp drop in the IV curve followed with a plateau (so called hotspot plateau) after all the wires (four wires connected in series) become resistive (see Figure 6.1)

The system quantum efficiency (SQE) is defined as the number of counts (after subtracting the dark counts) divided by the number of photons at the fiber input of the cryostat. The SQE is measured by using a continuous-wave laser attenuated to the single photon level at 1310 nm and reaches 4 % and 3.3 % in the TE and TM polarisations, respectively. Figure 6.7 shows the device quantum efficiency (DQE) of a WPNRD, defined
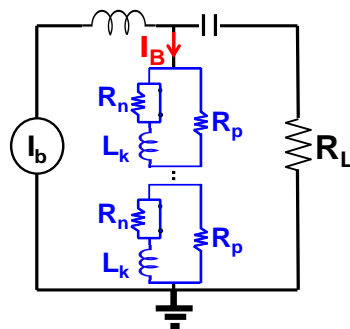


Figure 6.4 – The equivalent circuit of the series connected nanowires (modelled with a normal resistance ($R_n$) and an inductance ($L_k$)), each shunted by an integrated resistance ($R_p$).
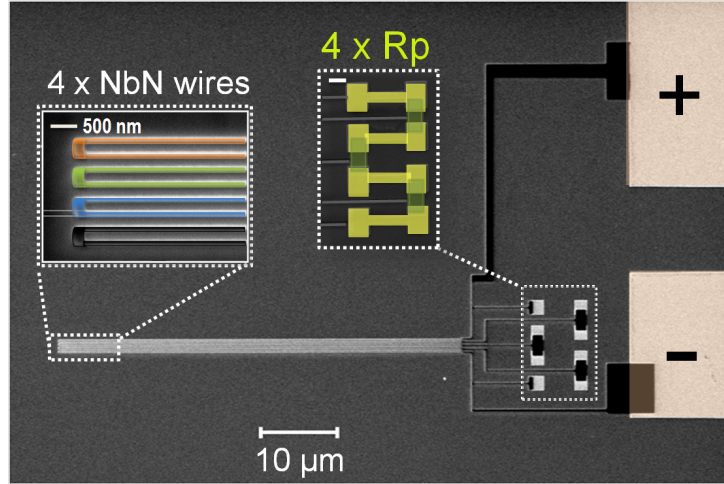
Figure 6.5 – Scanning electron microscope image of a WPNRD. Inset on the upper left: a blow-up image of the four wires before the waveguide etching step, where the wires have been coloured for clarity. Inset on the upper right: a close-up, false-coloured image of four AuPd parallel resistances ($4 \times R_p$). The scale bar of both the insets is 500 nm. The SEM images have been taken by Dr. A. Gaggero at CNR.

as the number of photocounts divided by the number of photons coupled in the waveguide. The DQE reaches to 24±2 % for TE and 22±1 % for TM polarisation at a bias current $I_b = 9.3$ $\mu$A and has been determined from the measured SQE and the coupling efficiency ($\eta$) of the photons from the fiber into the waveguide, $\eta_{TE} = 17\pm1$ % and $\eta_{TM} = 14.8\pm0.6$ % (SQE= DQEx$\eta$). The value of $\eta$ is approximately determined from the spectral average
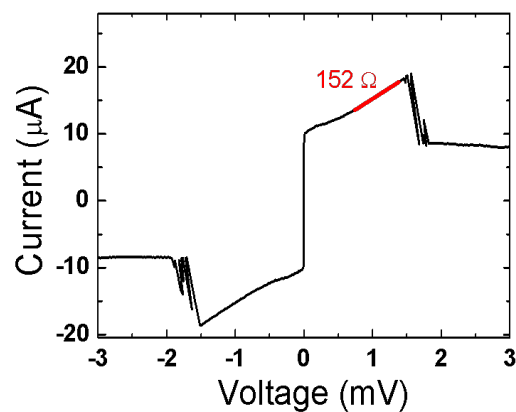


Figure 6.6 – IV characteristic of a four-element WPNRD, with $R_p = 38$ $\Omega$.

of the Fabry-Perot (FP) fringes measured on four, nominally identical waveguides (with no wires on top) by using a tunable laser around 1310 nm and its error bar is defined as the standard deviation among the four waveguides. For the TM polarisation, this value of $\eta$ ($\eta_{TM}$= 14±1 %) corresponds well to the one determined from the fringe contrast (as explained in subsection 2.2.2). For the TE polarisation, coupling to multiple lateral modes produces a complex fringe pattern, motivating our use of the spectral average. To date, this is the highest DQE reported for superconducting nanowire detectors with a single electrical output proportional to the photon number. The non-unity QE is attributed to the following reasons: 1- The absorptance of the 30 $\mu$m-long waveguides is calculated as 76 % and 85 % for the TE and TM polarisations, respectively. Longer wires may allow a higher DQE. 2- The deposition of very uniform NbN films is relatively difficult on GaAs[72] compared to the traditional substrates $Al_2O_3$[48,86] and MgO[110] as already discussed in chapter 3. Whilst the sputtering requires high temperature to promote the surface diffusion of the sputtered particles and obtain a high quality film, the GaAs surface starts to become rough above 350 °C[72]. Therefore, the film quality might also play a role in the quantum efficiency. Moreover, a change in the ratio of the TE and TM efficiencies is observed at low bias current, which seems to indicate a polarisation dependent internal quantum efficiency (probability of detection once a photon is absorbed), as previously observed also in Ref.[71].

The temporal response of the WPNRD is probed with a TE polarized pulsed laser-diode (10 MHz) at 1310 nm using a sampling oscilloscope with the detector biased at $I_b$= 8.8 $\mu$A. A photoresponse pulse corresponding to four-photon absorption is shown in the inset of Figure 6.7. After performing a moving average over 10 data points (green line), a 1/e decay time of $\tau_{1/e}$= 6.2 ns is calculated. That value agrees well with the value of $\tau_{1/e}$= 5.6 ns obtained from the simulation using the electro-thermal model (see[77] and it is plotted together in the same graph (red line). The deadtime (3x$\tau$) corresponds to an estimated maximum count rate of > 50 MHz.

In order to show the proof of PNR capability, the device is tested under illumination with a pulsed laser-diode ($\sim$ 100 ps pulse width, 2 MHz repetition rate), whose photon number distribution is described by Poissonian statistics, using a 40 GHz bandwidth sampling oscilloscope (from *Agilent Technologies*, 86100 C Infiniium DCA-j) after amplification by three amplifiers with a total gain of 43 dBm. Figure 6.8 shows an example of a photoresponse of the detector in TE polarization for a photon flux of 12 photons/pulse in the waveguide, corresponding to an average number of detected photons $\mu_{av} \sim$ 2.3 /pulse at $I_b$= 8.8 $\mu$A, with a DQE of 19 %. Five distinct detection levels in the figure correspond to the detection of 0-4 photons. The slow rise time of the photoresponse is due to the low-pass filter (LPF: DC - 80 MHz) added to the circuit to remove the high frequency noise (see the inset in Figure 6.7 for the photoresponse of four-photon absorption without LPF.).

After measuring the count rate at a fixed bias current, $I_b$= 8.8 $\mu$A, as a function of the threshold voltage ($V_{th}$) of a frequency counter at different powers (12 MHz repetition rate, TE polarization), the plateaus corresponding to the different photon levels are determined. By setting the threshold levels in the counter according to the different photon levels, the detection probability relative to $\geq$1- (red), $\geq$2- (green), $\geq$3- (blue) and $\geq$4- (purple) photon absorption events is measured as a function of the power in the waveguide and
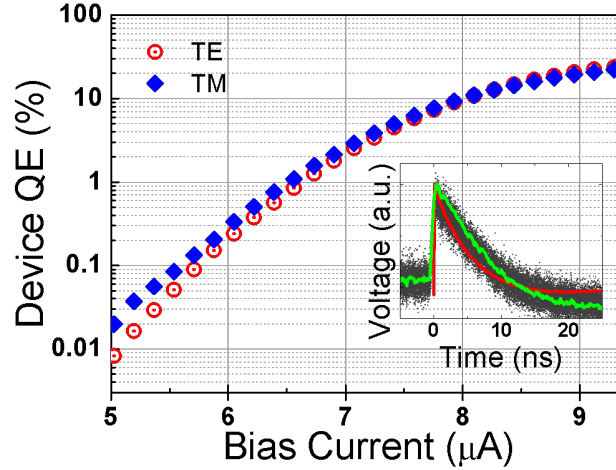
Figure 6.7 – Device quantum efficiency (device QE) of a WPNRD measured with TE and TM-polarized continuous-wave light at 1310 nm. Inset: Photoresponse pulse when four photons are detected. The green curve is the moving average of 10 data points showing a decay time of $\tau_{1/e}$= 6.2 ns and the red curve is the calculation from an electro-thermal simulation[77] after correcting for the filtering effect of the amplifiers (20 MHz - 6 GHz) when four photons are detected, giving a decay time of $\tau_{1/e}$= 5.6 ns.

plotted in Figure 6.9. The results are in a good agreement with the expected detection probability for a Poissonian source in the regime where detected average photon number $\mu$ is $\mu \ll 1$, as shown by the $\mu^x$ fits (black lines) in the figure for each photon level. The inset in Figure 6.9 shows the peak amplitudes ($V_{out}$) as a function of the detected photon numbers, together with a linear fit, showing the excellent linearity of the output voltage. The error bars represent the full-width-half-maximum (FWHM) of each peak which is nearly independent of the photon number, showing only about 20 % increase from 0- to 4- photon level.

In order to compare the WPNRDs with the first demonstration of a series-nanowire PNRD also called SND[87], further analysis is done on the noise. If there is no noise, when only one photon is absorbed, a Dirac-delta ($\delta$) like detection event is expected at a certain voltage and the voltage output is expected to increase linearly corresponding to the detected photon number. However, due to the electrical noise, there is a finite distribution of output voltages for each peak, as shown by the Gaussian fits in Figure 6.10 (top). Any increase of the width of the distribution with the photon level is denoted as *excess noise*. Excess noise is detrimental in PNRDs as it limits the signal-to-noise(S/N) ratio at high photon numbers and may limit the dynamic range. As previously depicted in the inset of Figure 6.9, the width of the Gaussian-peaks increases slightly from zero- to four-photon events and that shows the presence of an excess noise. The comparison of it with the SNDs previously demonstrated in a fiber-coupled configuration[87] is shown in Figure 6.10
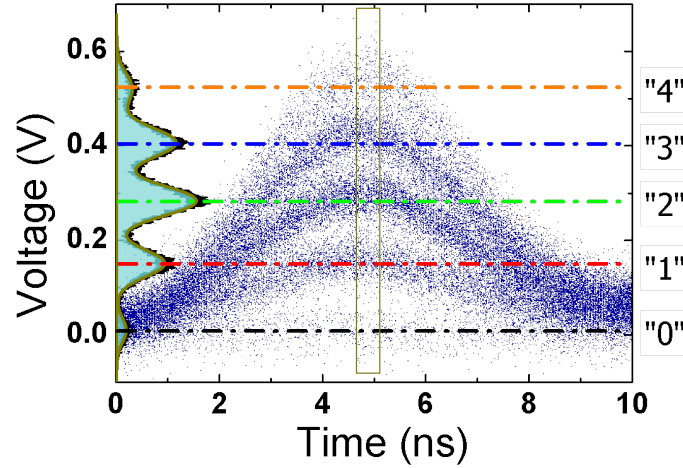
Figure 6.8 – An oscilloscope persistence map for a photon flux of 12 photons/pulse in the waveguide (3.7 pW average power), and corresponding measured (dark blue) pulse height distribution of one-to-four photon detection events (laser repetition rate of 2 MHz). A time window of 50 ps (dark-yellow rectangle) around the voltage peak is used to make a histogram as shown on the left axis (black line) with the corresponding multi-Gaussian fit (dark yellow line, area underneath filled with light blue). Distinct levels are observed corresponding to the detection of 0-4 photons as indicated on the right axis.

(bottom). In order to make the comparison independent of the differences in bias current and amplifier gain, the FWHM of the peaks are normalised by the average value of the 1-photon peak, which also scales proportionally to the bias current and gain. It is evident from Figure 6.10(bottom left) that the WPNRD represents similar S/N performance as the SND for the 1-photon level, but a much lower excess noise. The normalised excess noise, defined as $\sqrt{\Omega_n^2 - \Omega_0^2}$, where $\Omega_n = \sigma/V_{peak}^1$ is the standard deviation of the Gaussian fit of the $n-^{th}$ peak, is shown in Figure 6.10(bottom right).

In order to understand the origin of the noise, the possible sources of the excess noise are discussed in the following. As it has been discussed in Ref.[87], the *excess noise* can originate from three main sources. The first one is the non-uniformity in the wires, which appears as a variation of the resistance of the normal section. As the output voltage ($V_{out}$) is proportional to $nR_p x (I_b - I_{b\prime})$ (where $I_b$ is the bias current and $I_{b\prime}$ is the current flowing through the nanowire when the hotspot is formed (which depends on the resistance of the hotspot)), the changes in the resistance of the wire contributes to the spread of the voltage output amplitudes and accumulates for increasing number of switching wires. As the contributions of the different wires are uncorrelated, it scales as $\sqrt{n}$. This noise is intrinsic and can be improved by fabricating more uniform wires. The second source of
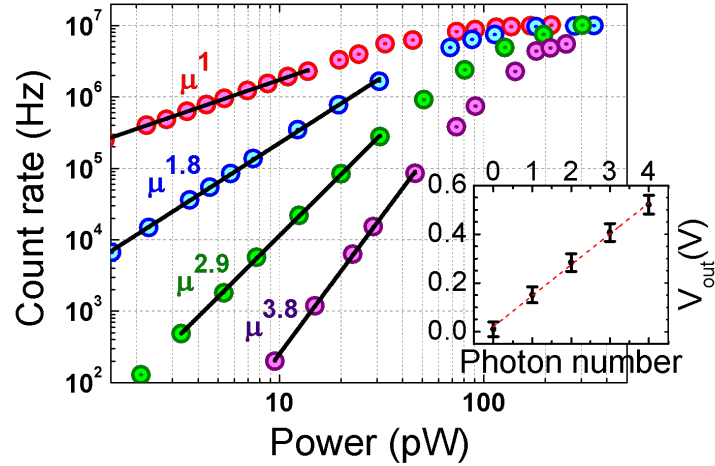
Figure 6.9 – Count rate measured with a pulsed laser (repetition rate of 12 MHz), corresponding to different photon counting levels: 1-photon (red), 2-photon (blue), 3-photon (green) and 4-photon (purple) and power-law fittings (black lines). The measurements in both figures are done at $I_b=$ 8.8 $\mu$A with a pulsed diode-laser in the TE polarization at 1310 nm. Inset: The signal amplitude as a function of the detected photon number, together with a linear fit (red dashed line). The black dots represent the peak voltage and the bars correspond to the full-width-half-maximum (FWHM) of each peak.

the noise is the thermal noise of the amplifiers[2][143], which can be modelled with equivalent current and voltage noise generators. The contribution of the current noise generator to the output voltage scales as the impedance seen by it, which is equal to the parallel of the detector impedance ($\propto nR_p$ when n photons are detected) and the 50 $\Omega$ input impedance of the amplifier. This noise contribution is therefore expected to scale proportionally to n for $nR_p<$ 50 $\Omega$, and then saturate for higher n. In Figure 6.10 (bottom), both plots have a signature of excess noise with the increasing photon number. The third noise source can be due to the spread in the parallel resistances as the amplitude of the voltage pulses scale proportionally[144]. The figure on the left shows that already at zero-photon level there is a large broadening and the value is very similar for a WPNRD and an SND. The noise at zero-level is mainly attributed to the amplifier chains used in the experiments. While the noise almost linearly increases for an SND, it tends to saturate for an WPNRD. As a consequence, the broadening of the WPNRD does not increase more than 20 % up to four-photon detection for a WPNRD while it is more than 100 % for the SND. As the technology used for fabricating the wires is nearly the same, the difference between the two detectors is tentatively attributed to the different chain of amplifiers used. The linear behaviour of the excess noise for SND indeed suggests that the noise is related to

---

[2]The thermal noise of the wires are negligible because of the low temperature operation.

the thermal noise of the amplifiers although the expected saturation for large n is not clearly observed in the case of the SND. It is noted however that the limited number of photon levels does not allow a clear discrimination between the dependences predicted for the three possible noise sources. For the future experiments, when the number of wires increases beyond four, a cold-stage pre-amplifier may be used in order to solve this issue to reduce the effect of the thermal noise of the amplifiers[145]. Another approach can be to implement the single-flux quantum (SFQ) circuit technology that is compatible with the NbN-based SSPD technology[146,147] as they are very promising due to their low-jitter and high-frequency performances[136].

The fidelity (a measure of how precisely a PNRD can reconstruct the photon number) of WPNRDs is potentially affected by five factors: 1- the limited number of wires, 2- the different absorption by the central and lateral wires, 3- the limited efficiency, 4- the signal-to-noise (S/N) ratio and 5- the crosstalk (spurious switching of a wire after photon absorption in an adjacent one). According to our previous study on closely-packed wires in a similar configuration (chapter 5 and [35]), crosstalk is negligible. The fidelity is studied in the following in the case of two photons incident on the 4-wire WPNRD and defined as P(2|2), i.e. probability of measuring the two incident photons. The four-element WPNRD is equivalent to a splitter with one input and four outputs connected to four single-photon detectors with splitting functions, $T_i$ ($\sum_{i=1}^{4} T_i = 1$) (see Figure 6.11). Here, the absorption probability in wire 'i' is denoted with $A_i$ and $A_{tot} = \sum A_i$. The internal quantum efficiency $\eta$ is assumed to be equal for all the wires. The WPNRD is then equivalent to the splitter of Figure 6.11 with $T_i = A_i/A_{tot}$ and the efficiency of detector $D_i$ is $\eta_{Di} = \eta A_{tot} \equiv \eta_D$. Then, the probability of two photons being directed to the $i^{th}$ detector producing an error is written as,

$$P_2^{(i)} = T_i^2 \tag{6.2}$$

Therefore, the probability of measuring the two photons in a pulse correctly ($P_{det} = P(2|2)$) is calculated by,

$$P(2|2) = \eta_D^2(1 - T_1^2 - T_2^2 - T_3^2 - T_4^2) \tag{6.3}$$

As shown in Figure 6.2, the fundamental modes are symmetric around the centre of the waveguide. That assures the equal mode overlap between the two central wires and also between the two lateral wires. Thus, eqn. 6.3 can be rewritten by simplifying for $T_1 = T_4$ and $T_2 = T_3$ as,

$$P(2|2) = \eta_D^2(1 - 2T_1^2 - 2T_2^2) \tag{6.4}$$

Therefore, using eqn. 6.4, the probability of measuring two photons P(2|2) arriving at the same time on an ideal four-element PNRD , having an equal splitting $T_1 = T_2 = 0.25$ and a unity efficiency, $\eta_D = 1$ is

$$P(2|2) = 1 - 4(0.25)^2 = 0.75 \tag{6.5}$$

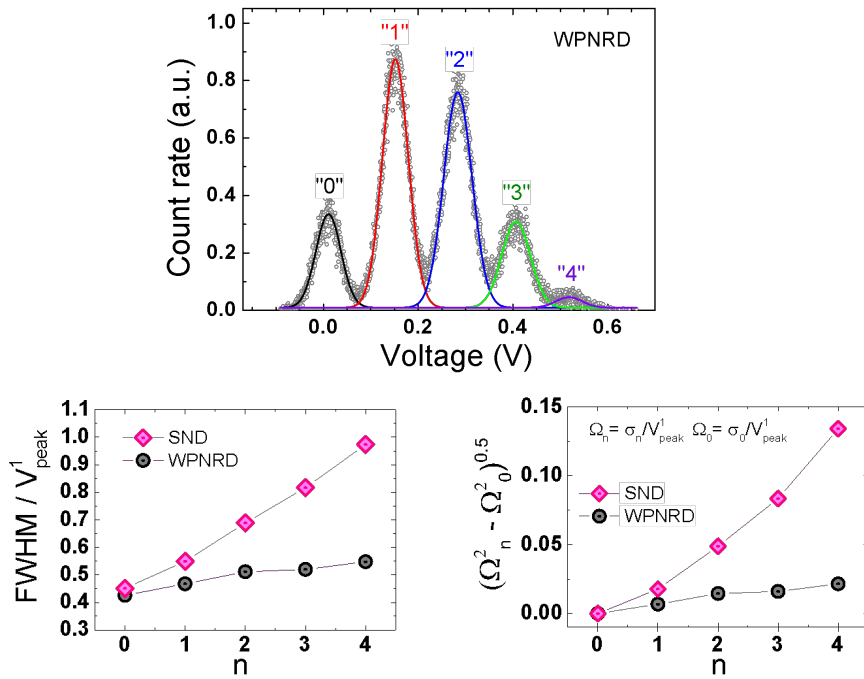which is due to the limited number of elements as also reported in Ref.[86].

Figure 6.10 – (Top)Measured (grey open circles) and fitted (multi-Gaussian fit lines in colour) pulse height distribution of a WPNRD with corresponding photon levels up to 4-photons (colour coded). (Bottom) Noise analysis of a WPNRD and its comparison with a series nanowire detector (SND). An SND also resolves up to 4-photons with the same configuration but exploits free-space coupling. The excess noise is analysed over (left) the full-width-half-maximum (FWHM) of each peak and each curve is divided by their 1-photon signal amplitudes and (right) the increase in the width of photon detection levels as a function of the detected number of photons. Both experiments are conducted at $\lambda = 1300$ nm with a pulsed laser-diode . The repetition rate of the laser is 2 MHz for the WPNRD and 10 MHz for the SND.
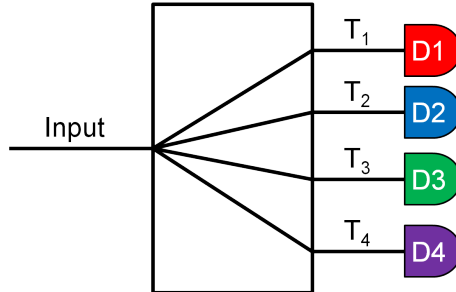
Figure 6.11 – A WPNRD is equivalent to a splitter with an input and a 4-port output.

In the waveguide design reported here with an unbalanced absorptance in the central and the lateral wires, P(2|2) given by eqn. 6.4 will be slightly reduced to 0.74 by considering a total absorptance for a 250 $\mu$m-long waveguide, $T_1$= 0.2 and $T_2$= 0.3 (see Figure 6.3), and $\eta_D$= 1.

Due to the limited efficiency (DQE = 0.24), the calculated probability of detecting two photons in the reported WPNRD device is P(2|2)= 0.058.

Finally, the limited S/N ratio results in a limitation in the fidelity related to the overlap between the adjacent photon levels (1-photon and 3-photon for a 2-photon detection). The P(2|2) related to this overlap only, assuming an infinite number of wires and unity efficiency, would be 0.97 (see the pulse-height distribution in Figure 6.8).

By calculating all the possible limitations, it has been concluded that the fidelity in the present device is mainly limited by the efficiency as previously concluded in Ref.[86] and it could be increased to 0.74 by increasing the length (ensuring the maximum absorptance) and the internal efficiency. Further improvements require an increase in the number of wires and a more uniform absorption probability.

## 6.5 Conclusions

In conclusion, WPNRDs based on NbN superconducting nanowires are demonstrated on a GaAs ridge waveguide. The detectors can resolve up to four photons and show device quantum efficiencies of 24 % and 22 % at 1310 nm for TE and TM polarized input light with an estimated maximum count rate of > 50 MHz. The efficiency can be maximized by further optimizing the film quality and the fabrication process. Moreover, fabricating longer wires as compared to the ones studied here (30 $\mu$m wires) may satisfy the total absorption and therefore increase the efficiency. Another way to increase the efficiency of the detectors may be to replace NbN with another material, such as $W_xSi_{1-x}$, which has been shown to have an internal efficiency approaching unity[69]. The fidelity is one of the major measurement parameters of a PNRD and it has been shown that with this WPNRD structure, the maximum fidelity for the measurement of two photons can be increased up to 0.74. These WPNRDs represent a substantial step towards the integration of highly-functional detectors in quantum photonic circuits.

# Chapter 7

# Conclusions and Outlook

In order to overcome the limitation of the operations with quantum bits (qubits) in quantum photonic experiments, the monolithic integration of the optical circuit elements is needed in so-called quantum photonic integrated circuits (QPICs). The monolithic integration has been challenging due to the difficulty of integrating sources, waveguides and detectors on the same substrate.

In view of the realisation of QPICs, a variety of aspects of the waveguide photon-detectors have been addressed within this thesis. The design, realisation and characterisation of single-photon and photon-number-resolving detectors based on superconducting nanowires integrated with GaAs waveguides are presented. The following conclusions can be drawn from this study:

- The optimisation of the challenging growth technology of ultrathin NbN films (4-6 nm-thick) on a GaAs substrate has been achieved by a dc magnetron sputtering technique. Due to the low growth rate, the importance of the impurity level in the deposition chamber has been evidenced and a Ti pre-deposition technique has been established. This allowed us to produce the majority of the data in this thesis as well as other results that have been reported with these films.

- The processing of superconducting NbN films has been developed using the facilities of the NanoLab@TU/e. This processing has been also used to fabricate single nanowires in order to study the film quality of the TU/e grown films. The processing presents a route to fabricate more complex structure using the same recipe.

- The waveguide single-photon detectors (WSPDs) realised on GaAs/AlGaAs ridge waveguide enable on-chip detection in QPIC. WSPDs benefit from high efficiency, high timing accuracy and short dead time enabled by the properties of the superconducting nanowires and demonstrated also in free-space coupled SSPDs. A device quantum efficiency of $\sim 20$ % has been reported on WSPDs with an estimated maximum count rate of $> 100$ MHz. The detectors are reported to be polarisation dependent for this specific design. It is also possible to obtain polarisation-independent detectors by modifying the waveguide dimensions.
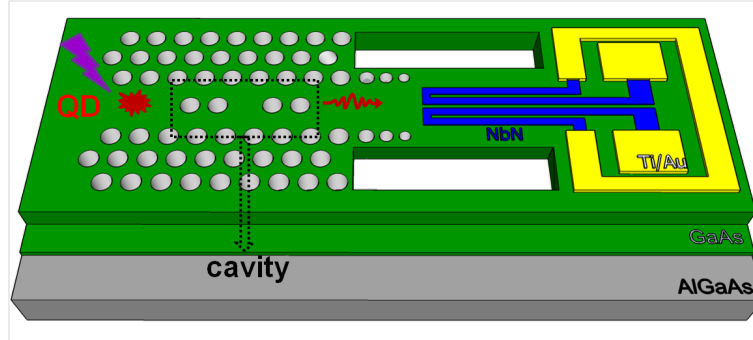
Figure 7.1 – Sketch of a fully integrated antibunching experiment.

- A 2x2 multi-mode interference (MMI) coupler is integrated with two detectors as an equivalent of a free-space Hanbury-Brown and Twiss interferometer with a beamsplitter and two detectors. Furthermore, an integrated autocorrelator is presented in a more compact geometry than the waveguide HBT by putting two detectors on the same waveguide. It has been demonstrated that the integrated autocorrelators enable the measurement of the second-order correlation function $g^{(2)}(\tau)$, which is a key functionality for a QPIC, allowing for example the characterization of single-photon states on-chip.

  Additionally, no crosstalk between the nanowires has been evidenced, despite their close proximity.

- Waveguide photon-number-resolving detectors (WPNRDs) resolving up to 4-photon have been demonstrated. WPNRDs are based on the series connection of the nanowires. A device quantum efficiency of $\sim 24$ % with a maximum estimated count rate of $> 50$ MHz have been demonstrated by using these detectors.

There is still room to improve the performance and the functionality in this exciting study, which has not been possible due to the limited time of this PhD work. The limited device quantum efficiency of the devices is one of them. This can be done by improving the film quality further, patterning narrower wires (60-80 nm)[31,70] and/or using low-gap superconducting films[32,69]. The yield[1] is low and needs to be improved because it is an important parameter for the integration.

Furthermore, more functional, fully integrated quantum photonic circuits are the next step to be realised. Figure 7.1 shows a schematic view of such an integration demonstrator, which is an autocorrelator integrated with a single-photon source and a cavity on the chip. However, this schematic is not very straight forward to realise as the processing of the WSPDs and the PhC has to be combined without deteriorating the properties of each other. In this direction, there has been some preliminary work done for the demonstration

---

[1]There has been only a systematic study on the electrical response of the detectors deposited on a single chip. Even though there is a small variation in the critical current across a chip, there is a wide variation in terms of efficiency.

of a fully integrated circuit. In order to understand if the NbN film deposition at high deposition temperature (nominally above 400 °C) changes the properties of the quantum dots (QDs) present in the heterostructure or if the photonic crystal fabrication introduces any degradation in the superconducting film quality, the fabrication steps needs to be checked carefully. As this thesis concentrates on the waveguide detectors, the possible scenarios from the film deposition point of view have been partly investigated. For instance, the high temperature annealing during the film sputtering may quench the photoluminescence of the QDs or it may broaden the emission line by changing the size and/or the interface states of the QDs. This, however, has not been evidenced. The width of QD single-exciton lines before and after the heat treatment is measured as $65 \pm 20$ $\mu$eV and $68 \pm 20$ $\mu$eV at full-width-half-maximum (FWHM). Moreover, there is no quenching observed in the PL intensity. Further research on these devices is ongoing.

# Bibliography

[1] G. N. Lewis, "The conservation of photons," *Nature*, vol. 118, pp. 874–875, 1926.

[2] T. D. Ladd, F. Jelezko, R. Laflamme, Y. Nakamura, C. Monroe, and J. L. O'Brien, "Quantum computers," *Nature*, vol. 464, no. 7285, pp. 45–53, 2010.

[3] N. Gisin, G. Ribordy, W. Tittel, and H. Zbinden, "Quantum cryptography," *Reviews of Modern Physics*, vol. 74, no. 1, pp. 145–195, 2002.

[4] J. L. O'Brien, "Optical quantum computing," *Science*, vol. 318, no. 5856, pp. 1567–1570, 2007.

[5] G. Brassard, "Brief history of quantum cryptography: A personal perspective," in *Theory and Practice in Information-Theoretic Security, 2005. IEEE Information Theory Workshop on*, pp. 19–23, IEEE, 2005.

[6] C. H. Bennett, F. Bessette, G. Brassard, L. Salvail, and J. Smolin, "Experimental quantum cryptography," *Journal of Cryptology*, vol. 5, no. 1, pp. 3–28, 1992.

[7] E. Waks, C. Santori, and Y. Yamamoto, "Security aspects of quantum key distribution with sub-poisson light," *Physical Review A*, vol. 66, no. 4, p. 042315, 2002.

[8] H.-K. Lo, X. Ma, and K. Chen, "Decoy state quantum key distribution," *Physical Review Letters*, vol. 94, no. 23, p. 230504, 2005.

[9] G. Brassard, N. Lütkenhaus, T. Mor, and B. C. Sanders, "Limitations on practical quantum cryptography," *Physical Review Letters*, vol. 85, no. 6, p. 1330, 2000.

[10] H. Takesue, S. W. Nam, Q. Zhang, R. H. Hadfield, T. Honjo, K. Tamaki, and Y. Yamamoto, "Quantum key distribution over a 40-db channel loss using superconducting single-photon detectors," *Nature Photonics*, vol. 1, no. 6, pp. 343–348, 2007.

[11] H. Shibata, K. Shimizu, H. Takesue, and Y. Tokura, "Superconducting nanowire single-photon detector with ultralow dark count rate using cold optical filters," *arXiv preprint arXiv:1307.0893*, 2013.

[12] R. P. Feynman, "Simulating physics with computers," *International Journal of Theoretical Physics*, vol. 21, no. 6, pp. 467–488, 1982.

[13] `http://www.orrerymaker.com/`. Last accessed: October 2013.

[14] A. Aspuru-Guzik and P. Walther, "Photonic quantum simulators," *Nature Physics*, vol. 8, no. 4, pp. 285–291, 2012.

[15] J. L. O'Brien, A. Furusawa, and J. Vučković, "Photonic quantum technologies," *Nature Photonics*, vol. 3, no. 12, pp. 687–695, 2009.

[16] A. Peruzzo, M. Lobino, J. C. Matthews, N. Matsuda, A. Politi, K. Poulios, X.-Q. Zhou, Y. Lahini, N. Ismail, K. Wörhoff, Y. Bromberg, Y. Silberberg, M. G. Thompson, and J. L. O'Brien, "Quantum walks of correlated photons," *Science*, vol. 329, no. 5998, pp. 1500–1503, 2010.

[17] B. J. Metcalf, N. Thomas-Peter, J. B. Spring, D. Kundys, M. A. Broome, P. C. Humphreys, X.-M. Jin, M. Barbieri, W. S. Kolthammer, J. C. Gates, B. J. Smith, N. K. Langford, P. G. Smith, and I. A. Walmsley, "Multiphoton quantum interference in a multiport integrated photonic device," *Nature Communications*, vol. 4, p. 1356, 2013.

[18] A. Crespi, R. Osellame, R. Ramponi, D. J. Brod, E. F. Galvão, N. Spagnolo, C. Vitelli, E. Maiorino, P. Mataloni, and F. Sciarrino, "Integrated multimode interferometers with arbitrary designs for photonic boson sampling," *Nature Photonics*, 2013.

[19] A. Politi, M. J. Cryan, J. G. Rarity, S. Yu, and J. L. O'Brien, "Silica-on-silicon waveguide quantum circuits," *Science*, vol. 320, no. 5876, pp. 646–649, 2008.

[20] D. Bonneau, E. Engin, K. Ohira, N. Suzuki, H. Yoshida, N. Iizuka, M. Ezaki, C. M. Natarajan, M. G. Tanner, R. H. Hadfield, *et al.*, "Quantum interference and manipulation of entanglement in silicon wire waveguide quantum circuits," *New Journal of Physics*, vol. 14, no. 4, p. 045003, 2012.

[21] E. Knill, R. Laflamme, and G. J. Milburn, "A scheme for efficient quantum computation with linear optics," *Nature*, vol. 409, no. 6816, pp. 46–52, 2001.

[22] A. J. Shields, "Semiconductor quantum light sources," *Nature Photonics*, vol. 1, no. 4, pp. 215–223, 2007.

[23] D. Englund, A. Faraon, B. Zhang, Y. Yamamoto, and J. Vučković, "Generation and transfer of single photons on a photonic crystal chip," *Optics Express*, vol. 15, no. 9, pp. 5550–5558, 2007.

[24] A. Schwagmann, S. Kalliakos, I. Farrer, J. P. Griffiths, G. A. C. Jones, D. A. Ritchie, and A. J. Shields, "On-chip single photon emission from an integrated semiconductor quantum dot into a photonic crystal waveguide," *Applied Physics Letters*, vol. 99, no. 26, pp. 261108–261108, 2011.

[25] T. B. Hoang, J. Beetz, M. Lermer, L. Midolo, M. Kamp, S. Höfling, and A. Fiore, "Widely tunable, efficient on-chip single photon sources at telecommunication wavelengths," *Optics Express*, vol. 20, no. 19, pp. 21758–21765, 2012.

[26] A. Laucht, S. Pütz, T. Günthner, N. Hauke, R. Saive, S. Frédérick, M. Bichler, M.-C. Amann, A. W. Holleitner, M. Kaniber, and J. J. Finley, "A waveguide-coupled on-chip single-photon source," *Physical Review X*, vol. 2, no. 1, p. 011014, 2012.

[27] S. Tanzilli, H. De Riedmatten, H. Zbinden, P. Baldi, M. De Micheli, D. B. Ostrowsky, and N. Gisin, "Highly efficient photon-pair source using periodically poled lithium niobate waveguide," *Electronics Letters*, vol. 37, no. 1, pp. 26–28, 2001.

[28] J. E. Sharping, K. F. Lee, M. A. Foster, A. C. Turner, B. S. Schmidt, M. Lipson, A. L. Gaeta, and P. Kumar, "Generation of correlated photons in nanoscale silicon waveguides," *Optics Express*, vol. 14, no. 25, pp. 12388–12393, 2006.

[29] J. P. Sprengers, A. Gaggero, D. Sahin, S. Jahanmirinejad, G. Frucci, F. Mattioli, R. Leoni, J. Beetz, M. Lermer, M. Kamp, S. Höfling, and A. Fiore, "Waveguide superconducting single-photon detectors for integrated quantum photonic circuits," *Applied Physics Letters*, vol. 99, no. 18, pp. 181110–181110, 2011.

[30] T. Gerrits, N. Thomas-Peter, J. C. Gates, A. E. Lita, B. J. Metcalf, B. Calkins, N. A. Tomlin, A. E. Fox, A. L. Linares, J. B. Spring, N. K. Langford, R. P. Mirin, P. G. R. Smith, I. A. Walmsley, and S. W. Nam, "On-chip, photon-number-resolving, telecommunication-band detectors for scalable photonic information processing," *Physical Review A*, vol. 84, no. 6, p. 060301, 2011.

[31] W. H. P. Pernice, C. Schuck, O. Minaeva, M. Li, G. N. Goltsman, A. V. Sergienko, and H. X. Tang, "High-speed and high-efficiency travelling wave single-photon detectors embedded in nanophotonic circuits," *Nature Communications*, vol. 3, p. 1325, 2012.

[32] C. Schuck, W. H. P. Pernice, and H. X. Tang, "Waveguide integrated low noise nbtin nanowire single-photon detectors with milli-hz dark count rate," *Scientific Reports*, vol. 3, 2013.

[33] G. Reithmaier, S. Lichtmannecker, T. Reichert, P. Hasch, K. Müller, M. Bichler, R. Gross, and J. J. Finley, "On-chip time resolved detection of quantum dot emission using integrated superconducting single photon detectors," *Scientific Reports*, vol. 3, 2013.

[34] S. Fattah poor, T. B. Hoang, L. Midolo, C. P. Dietrich, L. Li, E. H. Linfield, J. F. P. Schouwenberg, T. Xia, F. M. Pagliano, F. W. M. van Otten, and A. Fiore, "Efficient coupling of single photons to ridge-waveguide photonic integrated circuits," *Applied Physics Letters*, vol. 102, no. 13, pp. 131105–131105, 2013.

[35] D. Sahin, A. Gaggero, T. B. Hoang, G. Frucci, F. Mattioli, R. Leoni, J. Beetz, M. Lermer, M. Kamp, S. Höfling, and A. Fiore, "Integrated autocorrelator based on superconducting nanowires," *Optics Express*, vol. 21, no. 9, pp. 11162–11170, 2013.

[36] D. Sahin, A. Gaggero, Z. Zhou, S. Jahanmirinejad, F. Mattioli, R. Leoni, J. Beetz, M. Lermer, M. Kamp, S. Höfling, *et al.*, "Waveguide photon-number-resolving detectors for quantum photonic integrated circuits," *Applied Physics Letters*, vol. 103, no. 11, pp. 111116–111116, 2013.

[37] R. H. Hadfield, "Single-photon detectors for optical quantum information applications," *Nature Photonics*, vol. 3, no. 12, pp. 696–705, 2009.

[38] G. S. Buller and R. J. Collins, "Single-photon generation and detection," *Measurement Science and Technology*, vol. 21, no. 1, p. 012002, 2010.

[39] M. D. Eisaman, J. Fan, A. Migdall, and S. V. Polyakov, "Invited review article: Single-photon sources and detectors," *Review of Scientific Instruments*, vol. 82, no. 7, pp. 071101–071101, 2011.

[40] C. M. Natarajan, M. G. Tanner, and R. H. Hadfield, "Superconducting nanowire single-photon detectors: physics and applications," *Superconductor Science and Technology*, vol. 25, no. 6, p. 063001, 2012.

[41] http://www.hamamatsu.com/jp/en/index.html. Last accessed: July 2013.

[42] http://www.idquantique.com/instrumentation/product.html. Last accessed: November 2013.

[43] http://www.princetonlightwave.com. Last accessed: July 2013.

[44] G. Ribordy, N. Gisin, O. Guinnard, D. Stuck, M. Wegmuller, and H. Zbinden, "Photon counting at telecom wavelengths with commercial ingaas/inp avalanche photodiodes: current performance," *Journal of Modern Optics*, vol. 51, no. 9-10, pp. 1381–1398, 2004.

[45] B. E. Kardynał, Z. L. Yuan, and A. J. Shields, "An avalanche-photodiode-based photon-number-resolving detector," *Nature Photonics*, vol. 2, no. 7, pp. 425–428, 2008.

[46] A. E. Lita, A. J. Miller, and S. W. Nam, "Counting near-infrared single-photons with 95% efficiency," *Optics Express*, vol. 16, no. 5, pp. 3032–3040, 2008.

[47] K. D. Irwin and G. C. Hilton, "Transition-edge sensors," in *Cryogenic Particle Detection*, pp. 63–150, Springer, 2005.

[48] G. N. Goltsman, O. Okunev, G. Chulkova, A. Lipatov, A. Semenov, K. Smirnov, B. Voronov, A. Dzardanov, C. Williams, and R. Sobolewski, "Picosecond superconducting single-photon optical detector," *Applied Physics Letters*, vol. 79, no. 6, pp. 705–707, 2001.

[49] A. D. Semenov, G. N. GolâĂŹtsman, and A. A. Korneev, "Quantum detection by current carrying superconducting film," *Physica C: Superconductivity*, vol. 351, no. 4, pp. 349–356, 2001.

[50] A. Semenov, A. Engel, H.-W. Huebers, and M. Siegel, "Spectral cut-off in the efficiency of the resistive state formation caused by absorption of a single-photon in current-carrying superconducting nano-strips," *The European Physical Journal B-Condensed Matter and Complex Systems*, vol. 47, no. 4, pp. 495–501, 2005.

[51] A. Shoji, S. Kiryu, and S. Kohjiro, "Superconducting properties and normal-state resistivity of single-crystal nbn films prepared by a reactive rf-magnetron sputtering method," *Applied physics letters*, vol. 60, no. 13, pp. 1624–1626, 1992.

[52] P. Fabbricatore, G. Gemme, R. Musenich, R. Parodi, M. Viviani, B. Zhang, and V. Buscaglia, "Niobium and niobium-titanium nitrides for rf applications," *Applied Superconductivity, IEEE Transactions on*, vol. 3, no. 1, pp. 1761–1764, 1993.

[53] A. D. Semenov, P. Haas, H.-W. Hübers, K. Ilin, M. Siegel, A. Kirste, T. Schurig, and A. Engel, "Vortex-based single-photon response in nanostructured superconducting detectors," *Physica C: Superconductivity*, vol. 468, no. 7, pp. 627–630, 2008.

[54] J. Kitaygorsky, *Photon and dark counts in NbN superconducting single-photon detectors and nanostripes.* PhD thesis, University of Rochester, 2008.

[55] H. Bartolf, A. Engel, A. Schilling, K. Il'in, M. Siegel, H.-W. Hübers, and A. Semenov, "Current-assisted thermally activated flux liberation in ultrathin nanopatterned nbn superconducting meander structures," *Physical Review B*, vol. 81, p. 024502, Jan 2010.

[56] T. Yamashita, S. Miki, K. Makise, W. Qiu, H. Terai, M. Fujiwara, M. Sasaki, and Z. Wang, "Origin of intrinsic dark count in superconducting nanowire single-photon detectors," *Applied Physics Letters*, vol. 99, no. 16, p. 161105, 2011.

[57] A. Engel and A. Schilling, "Numerical analysis of detection-mechanism models of snspd," *arXiv preprint arXiv:1308.5781*, 2013.

[58] L. N. Bulaevskii, M. J. Graf, C. D. Batista, and V. G. Kogan, "Vortex-induced dissipation in narrow current-biased thin-film superconducting strips," *Physical Review B*, vol. 83, no. 14, p. 144526, 2011. PRB.

[59] L. N. Bulaevskii, M. J. Graf, and V. G. Kogan, "Vortex-assisted photon counts and their magnetic field dependence in single-photon superconducting detectors," *Physical Review B*, vol. 85, no. 1, p. 014505, 2012. PRB.

[60] Z. Zhou, G. Frucci, F. Mattioli, A. Gaggero, R. Leoni, S. Jahanmirinejad, T. B. Hoang, and A. Fiore, "Ultrasensitive n-photon interferometric autocorrelator," *Physical Review Letters*, vol. 110, no. 13, p. 133605, 2013.

[61] J. K. W. Yang, A. J. Kerman, E. A. Dauler, V. Anant, K. M. Rosfjord, and K. K. Berggren, "Modeling the electrical and thermal response of superconducting nanowire single-photon detectors," *Applied Superconductivity, IEEE Transactions on*, vol. 17, no. 2, pp. 581–585, 2007.

[62] F. Marsili, *Single-photon and photon-number-resolving detectors based on superconducting nanowires.* PhD thesis, École Polytechnique Fédérale de Lausanne, 2009.

[63] L. Maingault, M. Tarkhov, I. Florya, A. Semenov, R. Espiau de Lamaestre, P. Cavalier, G. Goltsman, J.-P. Poizat, and J.-C. Villégier, "Spectral dependency of superconducting single photon detectors," *Journal of Applied Physics*, vol. 107, no. 11, pp. 116103–116103, 2010.

[64] A. J. Kerman, E. A. Dauler, J. K. W. Yang, K. M. Rosfjord, V. Anant, K. K. Berggren, G. N. Goltsman, and B. M. Voronov, "Constriction-limited detection efficiency of superconducting nanowire single-photon detectors," *Applied Physics Letters*, vol. 90, no. 10, pp. 101110–101110, 2007.

[65] F. Marsili, F. Bellei, F. Najafi, A. E. Dane, E. A. Dauler, R. J. Molnar, and K. K. Berggren, "Efficient single photon detection from 500 nm to 5 $\mu$m wavelength," *Nano Letters*, vol. 12, no. 9, pp. 4799–4804, 2012.

[66] F. Marsili, F. Najafi, E. Dauler, F. Bellei, X. Hu, M. Csete, R. J. Molnar, and K. K. Berggren, "Single-photon detectors based on ultranarrow superconducting nanowires," *Nano Letters*, vol. 11, no. 5, pp. 2048–2053, 2011.

[67] S. N. Dorenbos, P. Forn-Díaz, T. Fuse, A. Verbruggen, T. Zijlstra, T. M. Klapwijk, and V. Zwiller, "Low gap superconducting single photon detectors for infrared sensitivity," *Applied Physics Letters*, vol. 98, no. 25, pp. 251102–251102, 2011.

[68] A. Engel, A. Aeschbacher, K. Inderbitzin, A. Schilling, K. Ilín, M. Hofherr, M. Siegel, A. Semenov, and H.-W. Hubers, "Tantalum nitride superconducting single-photon detectors with low cut-off energy," *Applied Physics Letters*, vol. 100, no. 6, pp. 062601–062601, 2012.

[69] F. Marsili, V. B. Verma, J. A. Stern, S. Harrington, A. E. Lita, T. Gerrits, I. Vayshenker, B. Baek, M. D. Shaw, R. P. Mirin, and S. W. Nam, "Detecting single infrared photons with 93% system efficiency," *Nature Photonics*, vol. 7, no. 3, pp. 210–214, 2013.

[70] T. Yamashita, S. Miki, H. Terai, and Z. Wang, "Low-filling-factor superconducting single photon detector with high system detection efficiency," *arXiv preprint arXiv:1305.2672*.

[71] V. Anant, A. J. Kerman, E. A. Dauler, J. K. Yang, K. M. Rosfjord, and K. K. Berggren, "Optical properties of superconducting nanowire single-photon detectors.," *Optics Express*, vol. 16, no. 14, pp. 10750–10761, 2008.

[72] A. Gaggero, S. J. Nejad, F. Marsili, F. Mattioli, R. Leoni, D. Bitauld, D. Sahin, G. J. Hamhuis, R. Nötzel, R. Sanjines, and A. Fiore, "Nanowire superconducting single-photon detectors on gaas for integrated quantum photonic applications," *Applied Physics Letters*, vol. 97, no. 15, pp. 151108–151108, 2010.

[73] E. F. C. Driessen, F. R. Braakman, E. M. Reiger, S. N. Dorenbos, V. Zwiller, and M. J. A. De Dood, "Impedance model for the polarization-dependent optical absorption of superconducting single-photon detectors," *The European Physical Journal Applied physics*, vol. 47, no. 1, p. 705, 2009.

[74] K. M. Rosfjord, J. K. W. Yang, E. A. Dauler, A. J. Kerman, V. Anant, B. M. Voronov, G. N. Gol'Tsman, and K. K. Berggren, "Nanowire single-photon detector with an integrated optical cavity and anti-reflection coating," *Optics Express*, vol. 14, no. 2, pp. 527–534, 2006.

[75] Y. Korneeva, I. Florya, A. Semenov, A. Korneev, and G. Goltsman, "New generation of nanowire nbn superconducting single-photon detector for mid-infrared," *Applied Superconductivity, IEEE Transactions on*, vol. 21, no. 3, pp. 323–326, 2011.

[76] A. J. Kerman, J. K. W. Yang, R. J. Molnar, E. A. Dauler, and K. K. Berggren, "Electrothermal feedback in superconducting nanowire single-photon detectors," *Physical Review B*, vol. 79, no. 10, p. 100509, 2009.

[77] S. Jahanmirinejad and A. Fiore, "Proposal for a superconducting photon number resolving detector with large dynamic range," *Optics Express*, vol. 20, no. 5, pp. 5017–5028, 2012.

[78] A. J. Kerman, E. A. Dauler, W. E. Keicher, J. K. W. Yang, K. K. Berggren, G. Gol'tsman, and B. Voronov, "Kinetic-inductance-limited reset time of superconducting nanowire photon counters," *Applied Physics Letters*, vol. 88, no. 11, p. 111116, 2006.

[79] A. Divochiy, F. Marsili, D. Bitauld, A. Gaggero, R. Leoni, F. Mattioli, A. Korneev, V. Seleznev, N. Kaurova, O. Minaeva, G. Gol'tsman, K. G. Lagoudakis, M. Benkhaoul, F. Lévy, and A. Fiore, "Superconducting nanowire photon-number-resolving detector at telecommunication wavelengths," *Nature Photonics*, vol. 2, no. 5, pp. 302–306, 2008.

[80] A. R. Dixon, Z. L. Yuan, J. F. Dynes, A. W. Sharpe, and A. J. Shields, "Gigahertz decoy quantum key distribution with 1 mbit/s secure key rate," *arXiv preprint arXiv:0810.1069*, 2008.

[81] D. Fukuda, G. Fujii, T. Numata, A. Yoshizawa, H. Tsuchida, H. Fujino, H. Ishii, T. Itatani, S. Inoue, and T. Zama, "Photon number resolving detection with high speed and high quantum efficiency," *Metrologia*, vol. 46, no. 4, p. S288, 2009.

[82] M. J. Stevens, R. H. Hadfield, R. E. Schwall, S. W. Nam, R. P. Mirin, and J. A. Gupta, "Fast lifetime measurements of infrared emitters using a low-jitter superconducting single-photon detector," *Applied Physics Letters*, vol. 89, no. 3, pp. 031109–031109, 2006.

[83] J. Zhang, W. Slysz, A. Verevkin, O. Okunev, G. Chulkova, A. Korneev, A. Lipatov, G. N. Gol'tsman, and R. Sobolewski, "Response time characterization of nbn superconducting single-photon detectors," *Applied Superconductivity, IEEE Transactions on*, vol. 13, no. 2, pp. 180–183, 2003.

[84] L. You, X. Yang, Y. He, W. Zhang, D. Liu, W. Zhang, L. Zhang, L. Zhang, X. Liu, S. Chen, Z. Wang, and X. Xie, "Jitter analysis of a superconducting nanowire single photon detector," *AIP Advances*, vol. 3, no. 7, pp. 072135–072135, 2013.

[85] D. Sahin, A. Gaggero, G. Frucci, S. Jahanmirinejad, J. P. Sprengers, F. Mattioli, R. Leoni, J. Beetz, M. Lermer, M. Kamp, , S. Höfling, and A. Fiore, "Waveguide superconducting single-photon autocorrelators for quantum photonic applications," in *SPIE OPTO*, pp. 86351B–86351B, International Society for Optics and Photonics, 2013.

[86] E. A. Dauler, A. J. Kerman, B. S. Robinson, J. K. W. Yang, B. Voronov, G. Goltsman, S. A. Hamilton, and K. K. Berggren, "Photon-number-resolution with sub-30-ps timing using multi-element superconducting nanowire single photon detectors," *Journal of Modern Optics*, vol. 56, no. 2-3, pp. 364–373, 2009.

[87] S. Jahanmirinejad, G. Frucci, F. Mattioli, D. Sahin, A. Gaggero, R. Leoni, and A. Fiore, "Photon-number resolving detector based on a series array of superconducting nanowires," *Applied Physics Letters*, vol. 101, no. 7, pp. 072602–072602, 2012.

[88] C. M. Natarajan, L. Zhang, H. Coldenstrodt-Ronge, G. Donati, S. N. Dorenbos, V. Zwiller, I. A. Walmsley, and R. Hadfield, "Quantum detector tomography of a time-multiplexed superconducting nanowire single-photon detector at telecom wavelengths," *Optics Express*, vol. 21, no. 1, pp. 893–902, 2013.

[89] M. J. Fitch, B. C. Jacobs, T. B. Pittman, and J. D. Franson, "Photon-number resolution using time-multiplexed single-photon detectors," *Physical Review A*, vol. 68, no. 4, p. 043814, 2003.

[90] E. Pomarico, B. Sanguinetti, R. Thew, and H. Zbinden, "Room temperature photon number resolving detector for infared wavelengths," *Optics Express*, vol. 18, no. 10, pp. 10750–10759, 2010.

[91] M. Fujiwara and M. Sasaki, "Direct measurement of photon number statistics at telecom wavelengths using a charge integration photon detector," *Applied Optics*, vol. 46, no. 16, pp. 3069–3074, 2007.

[92] D. Rosenberg, A. E. Lita, A. J. Miller, and S. W. Nam, "Noise-free high-efficiency photon-number-resolving detectors," *Physical Review A*, vol. 71, no. 6, p. 061803, 2005.

[93] B. Calkins, P. L. Mennea, A. E. Lita, B. J. Metcalf, W. S. Kolthammer, A. L. Linares, J. B. Spring, P. C. Humphreys, R. P. Mirin, J. C. Gates, P. G. Smith, I. A. Walmsley, and S. W. Nam, "High quantum-efficiency photon-number-resolving detector for photonic on-chip information processing," *Optics Express*, vol. 21.

[94] D. Sahin, I. Yildiz, A. I. Gencer, G. Aygun, A. Slaoui, and R. Turan, "Evolution of $sio_2$/ge/$hfo_2$ (ge) multilayer structure during high temperature annealing," *Thin Solid Films*, vol. 518, no. 9, pp. 2365–2369, 2010.

[95] F. Marsili, *Single-photon and photon-number-resolving detectors based on superconducting nanowires-Chapter 3*. PhD thesis, École Polytechnique Fédérale de Lausanne, 2009.

[96] D. M. Mattox, "The good vacuum (low pressure) processing environment - chapter 3,"

[97] `http://www.gammavacuum.com/productnc.asp?typeid=23&gclid=` `CLPXq6uq37gCFXMQtAod7xsAIw`. Last accessed: August 2013.

[98] F. Marsili, *Single-photon and photon-number-resolving detectors based on superconducting nanowires - Chapter 2*. PhD thesis, École Polytechnique Fédérale de Lausanne, 2009.

[99] A. Guillén-Cervantes, Z. Rivera-Alvarez, M. López-López, E. López-Luna, and I. Hernández-Calderón, "Gaas surface oxide desorption by annealing in ultra high vacuum," *Thin Solid Films*, vol. 373, no. 1, pp. 159–163, 2000.

[100] J.-W. Weber, T. Hansen, M. Van de Sanden, and R. Engeln, "B-spline parametrization of the dielectric function applied to spectroscopic ellipsometry on amorphous carbon," *Journal of Applied Physics*, vol. 106, no. 12, pp. 123503–123503, 2009.

[101] L. Midolo, *Electromechanical tuning of photonic crystal cavities - Chapter 2*. PhD thesis, Eindhoven University of Technology, 2013.

[102] D. Bitauld, F. Marsili, A. Gaggero, F. Mattioli, R. Leoni, S. J. Nejad, F. Lévy, and A. Fiore, "Nanoscale optical detector with single-photon and multiphoton sensitivity," *Nano Letters*, vol. 10, no. 8, pp. 2977–2981, 2010.

[103] W. J. Skocpol, M. R. Beasley, and M. Tinkham, "Self-heating hotspots in superconducting thin-film microbridges," *Journal of Applied Physics*, vol. 45, no. 9, pp. 4054–4066, 1974.

[104] S. Jahanmirinejad, *Superconducting Single-Photon and Photon-Number-Resolving Detectors-Chapter 2*. PhD thesis, Eindhoven University of Technology, 2012.

[105] A. M. Fox, *Optical properties of solids*, vol. 3. Oxford university press, 2001.

[106] S. Miki, Y. Uzawa, A. Kawakami, and Z. Wang, "Fabrication and if bandwidth measurements of nbn hot-electron bolometers," *Electronics and Communications in Japan (Part II: Electronics)*, vol. 85, no. 7, pp. 77–83, 2002.

[107] J.-C. Villégier, N. Hadacek, S. Monso, B. Delnet, A. Roussy, P. Febvre, G. Lamura, and J.-Y. Laval, "Nbn multilayer technology on r-plane sapphire," *Applied Superconductivity, IEEE Transactions on*, vol. 11, no. 1, pp. 68–71, 2001.

[108] S. Miki, T. Yamashita, H. Terai, and Z. Wang, "High performance fiber-coupled nbtin superconducting nanowire single photon detectors with gifford-mcmahon cryocooler," *Optics Express*, vol. 21, p. 10208, 2013.

[109] F. Marsili, A. Gaggero, L. H. Li, A. Surrente, R. Leoni, F. Lévy, and A. Fiore, "High quality superconducting nbn thin films on gaas," *Superconductor Science and Technology*, vol. 22, no. 9, p. 095013, 2009.

[110] F. Marsili, D. Bitauld, A. Fiore, A. Gaggero, F. Mattioli, R. Leoni, M. Benkahoul, and F. Lévy, "High efficiency nbn nanowire superconducting single photon detectors fabricated on mgo substrates from a low temperature process," *OptÄścs Express*, vol. 16, no. 5, pp. 3191–3196, 2008.

[111] A. Semenov, B. Günther, U. Böttger, H.-W. Hübers, H. Bartolf, A. Engel, A. Schilling, K. Ilin, M. Siegel, R. Schneider, D. Gerthsen, and N. A. Gippius, "Optical and transport properties of ultrathin nbn films and nanostructures," *Physical Review B*, vol. 80, no. 5, p. 054510, 2009.

[112] L. N. Cooper, "Superconductivity in the neighborhood of metallic contacts," *Physical Review Letters*, vol. 6, 1961.

[113] K. Ilin, R. Schneider, D. Gerthsen, A. Engel, H. Bartolf, A. Schilling, A. Semenov, H. Huebers, B. Freitag, and M. Siegel, "Ultra-thin nbn films on si: crystalline and superconducting properties," in *Journal of Physics: Conference Series*, vol. 97, p. 012045, IOP Publishing, 2008.

[114] J. J. Zhang, X. Su, L. Zhang, L. Zheng, X. F. Wang, and L. You, "Improvement of the superconducting properties of nbn thin film on single-crystal silicon substrate by using a tin buffer layer," *Superconductor Science and Technology*, vol. 26, no. 4, p. 045010, 2013.

[115] W. L. McMillan, "Tunneling model of the superconducting proximity effect," *Physical Review*, vol. 175, pp. 537–542, Nov 1968.

[116] S. Ezaki, K. Makise, B. Shinozaki, T. Odo, T. Asano, H. Terai, T. Yamashita, S. Miki, and Z. Wang, "Localization and interaction effects in ultrathin epitaxial nbn superconducting films," *Journal of Physics: Condensed Matter*, vol. 24, no. 47, p. 475702, 2012.

[117] S. P. Chockalingam, M. Chand, J. Jesudasan, V. Tripathi, and P. Raychaudhuri, "Superconducting properties and hall effect of epitaxial nbn thin films," *Physical Review B*, vol. 77, no. 21, p. 214503, 2008.

[118] C. Delacour, L. Ortega, M. Faucher, T. Crozes, T. Fournier, B. Pannetier, and V. Bouchiat, "Persistence of superconductivity in niobium ultrathin films grown on r-plane sapphire," *Physical Review B*, vol. 83, no. 14, p. 144504, 2011.

[119] A. V. Linde, R.-M. Marin-Ayral, D. Granier, F. Bosc-Rouessac, and V. V. Grachev, "Synthesis of cubic niobium nitride by reactive diffusion under nitrogen pressure," *Materials Research Bulletin*, vol. 44, no. 5, pp. 1025–1030, 2009.

[120] W. Słysz, M. Guziewicz, M. Borysiewicz, J. Z. Domagała, I. Pasternak, K. Hejduk, W. Rzodkiewicz, J. Ratajczak, J. Bar, M. Węgrzecki, P. Grabiec, R. Grodecki, I. Węgrzecki, and R. Sobolewski, "Ultrathin nbn films for superconducting single-photon detectors," *Acta Physica Polonica A*, vol. 120, no. 1, pp. 200–203, 2011.

[121] J. A. Thornton, "High rate thick film growth," *Annual Review of Materials Science*, vol. 7, no. 1, pp. 239–260, 1977.

[122] Z. Wang, A. Kawakami, Y. Uzawa, and B. Komiyama, "Superconducting properties and crystal structures of single-crystal niobium nitride thin films deposited at ambient substrate temperature," *Journal of Applied Physics*, vol. 79, no. 10, pp. 7837–7842, 1996.

[123] G. Gol'tsman, O. Okunev, G. Chulkova, A. Lipatov, A. Dzardanov, K. Smirnov, A. Semenov, B. Voronov, C. Williams, and R. Sobolewski, "Fabrication and properties of an ultrafast nbn hot-electron single-photon detector," *Applied Superconductivity, IEEE Transactions on*, vol. 11, no. 1, pp. 574–577, 2001.

[124] R. op het Veld, "Study of tu/e grown nanowire single photon detectors," 2012. Eindhoven University of Technology, Bachelor report.

[125] E. A. Dauler, *Multi-element superconducting nanowire single photon detectors-Chapter 3*. PhD thesis, Massachusetts Institute of Technology, 2009.

[126] R. Sobolewski, A. Verevkin, G. N. Gol'tsman, A. Lipatov, and K. Wilsher, "Ultrafast superconducting single-photon optical detectors and their applications," *Applied Superconductivity, IEEE Transactions on*, vol. 13, no. 2, pp. 1151–1157, 2003.

[127] V. Anant, *Engineering the optical properties of subwavelength devices and materials - Chapter 6*. PhD thesis, Massachusetts Institute of Technology, 2007.

[128] L. Sansoni, F. Sciarrino, G. Vallone, P. Mataloni, A. Crespi, R. Ramponi, and R. Osellame, "Two-particle bosonic-fermionic quantum walk via integrated photonics," *Physical Review Letters*, vol. 108, no. 1, p. 010502, 2012.

[129] C. Schuck, W. H. P. Pernice, and H. X. Tang, "Nbtin superconducting nanowire detectors for visible and telecom wavelengths single photon counting on si3n4 photonic circuits," *Applied Physics Letters*, vol. 102, no. 5, pp. 051101–051101, 2013.

[130] G. Tittelbach, B. Richter, and W. Karthe, "Comparison of three transmission methods for integrated optical waveguide propagation loss measurement," *Pure and Applied Optics: Journal of the European Optical Society Part A*, vol. 2, no. 6, p. 683, 1993.

[131] B. E. A. Saleh, M. C. Teich, and B. E. Saleh, *Fundamentals of photonics*, vol. 22. Wiley New York, 1991.

[132] F. Marsili, D. Bitauld, A. Gaggero, S. Jahanmirinejad, R. Leoni, F. Mattioli, and A. Fiore, "Physics and application of photon number resolving detectors based on superconducting parallel nanowires," *New Journal of Physics*, vol. 11, no. 4, p. 045022, 2009.

[133] R. H. Brown and R. Twiss, "A test of a new type of stellar interferometer on sirius," *Nature*, vol. 178, no. 4541, pp. 1046–1048, 1956.

[134] E. A. Dauler, B. S. Robinson, A. J. Kerman, J. K. W. Yang, E. K. M. Rosfjord, V. Anant, B. Voronov, G. Gol'tsman, and K. K. Berggren, "Multi-element superconducting nanowire single-photon detector," *Applied Superconductivity, IEEE Transactions on*, vol. 17, no. 2, pp. 279–284, 2007.

[135] E. A. Patent, *Optical Self-Switching Effect in Mach-Zehnder Interferometers*. PhD thesis, Eindhoven University of Technology, 2005.

[136] T. Yamashita, S. Miki, H. Terai, K. Makise, and Z. Wang, "Crosstalk-free operation of multielement superconducting nanowire single-photon detector array integrated with single-flux-quantum circuit in a 0.1 w gifford–mcmahon cryocooler," *Optics Letters*, vol. 37, no. 14, pp. 2982–2984, 2012.

[137] K. S. Ilin, M. Lindgren, M. Currie, A. D. Semenov, G. N. Goltsman, R. Sobolewski, S. I. Cherednichenko, and E. M. Gershenzon, "Picosecond hot-electron energy relaxation in nbn superconducting photodetectors," *Applied Physics Letters*, vol. 76, no. 19, pp. 2752–2754, 2000.

[138] A. Korneev, Y. Vachtomin, O. Minaeva, A. Divochiy, K. Smirnov, O. Okunev, G. Gol'tsman, C. Zinoni, N. Chauvin, L. Balet, F. Marsili, D. Bitauld, B. Alloing, L. Li, A. Fiore, L. Lunghi, A. Gerardino, M. Halder, C. Jorel, and H. Zbinden, "Single-photon detection system for quantum optics applications," *Selected Topics in Quantum Electronics, IEEE Journal of*, vol. 13, no. 4, pp. 944–951, 2007.

[139] E. Knill, R. Laflamme, and G. J. Milburn, "A scheme for efficient quantum computation with linear optics," *Nature*, vol. 409, no. 6816, pp. 46–52, 2001.

[140] L. A. Jiang, E. A. Dauler, and J. T. Chang, "Photon-number-resolving detector with 10 bits of resolution," *Physical Review A*, vol. 75, p. 062325, Jun 2007.

[141] Q. Zhao, A. McCaughan, F. Bellei, F. Najafi, D. De Fazio, A. Dane, Y. Ivry, and K. K. Berggren, "Superconducting-nanowire single-photon-detector linear array," *Applied Physics Letters*, vol. 103, no. 14, pp. 142602–142602, 2013.

[142] T. Huang, X. Wang, J. Shao, X. Guo, L. Xiao, and S. Jia, "Single event photon statistics characterization of a single photon source in an imperfect detection system," *Journal of Luminescence*, vol. 124, no. 2, pp. 286 – 290, 2007.

[143] M. Bell, A. Antipov, B. Karasik, A. Sergeev, V. Mitin, and A. Verevkin, "Photon number-resolved detection with sequentially connected nanowires," *Applied Superconductivity, IEEE Transactions on*, vol. 17, no. 2, pp. 289–292, 2007.

[144] Z. Zhou, S. Jahanmirinejad, F. Mattioli, D. Sahin, G. Frucci, A. Gaggero, R. Leoni, and A. Fiore, "Superconducting series nanowire detector counting up to twelve photons," *arXiv preprint arXiv:1311.6458*, 2013.

[145] S. Jahanmirinejad, *Superconducting Single-Photon and Photon-Number-Resolving Detectors-Chapter 5*. PhD thesis, Eindhoven University of Technology, 2012.

[146] H. Terai, S. Miki, and Z. Wang, "Readout electronics using single-flux-quantum circuit technology for superconducting single-photon detector array," *Applied Superconductivity, IEEE Transactions on*, vol. 19, no. 3, pp. 350–353, 2009.

[147] H. Terai, K. Makise, and Z. Wang, "Operation of single-flux-quantum logic cells based on all-nbn integrated circuit technology," in *Superconductive Electronics Conference (ISEC), 2013 IEEE 14th International*, pp. 1–3, IEEE, 2013.

# Summary

## Waveguide Single-Photon and Photon-Number-Resolving Detectors

For the realisation of quantum photonic integrated circuits (QPICs), the integration of single-photon detectors (SPDs) with passive waveguides and single-photon sources is required. To this aim, in this thesis first single-photon detectors based on superconducting NbN nanowires on ridge waveguide have been realised, and then more functional detector structures have been integrated. In the first chapter, the concept of QPIC is introduced and three demanding applications are explained. Single-photon detectors (SPDs), in particular superconducting single-photon detectors (SSPDs) and photon-number-resolving detectors (PNRDs) as well as the relevant concepts are introduced.

In the first part of the second chapter, the fabrication, characterisation and processing of NbN SSPDs are discussed. Ti pre-deposition is discussed in order to obtain state-of-the-art films and the first TU/e developed fabrication process is described. In the second part, the experimental setups used to characterise NbN superconducting nanowire detectors are explained. Moreover, the dark count resulting from the blackbody radiation is discussed and addressed. In the last part, the design of the waveguide superconducting nanowire detectors and the model are discussed.

The third chapter is dedicated to the study of the NbN films grown on GaAs substrate. The optimisation of the films and electrical characterisation of NbN single nanowires are extensively discussed. Moreover, optical constants of ultrathin NbN films that are extracted by using a spectroscopic ellipsometer technique are presented.

In the fourth chapter, superconducting waveguide single-photon detectors are introduced. The concept, design and fabrication of these detectors as well as the experimental results are discussed. A device quantum efficiency of 20 % with a timing jitter of $\sim$ 60 ps is reported. The difference between the transverse-electric (TE) and transverse-magnetic (TM) polarisation efficiencies are attributed to the complex TM mode-profile due to non-optimised waveguide geometry for the TM polarisation. Therefore, it is difficult to couple the mode efficiently into the waveguide.

The fifth chapter introduces two types of waveguide nanowire detectors, both of which

can be used for the measurement of the second-order correlation function $g^{(2)}(\tau)$ by replacing the beam-splitter and the two distinct detectors of a Hanbury-Brown and Twiss type interferometer. The first device, which is called waveguide Hanbury-Brown and Twiss (WHBT), has one multi-mode interference coupler (MMI) with two inputs and two outputs. There are two detectors fabricated on each output arm. This device is optimised for 50:50 splitting at 1550 nm. The second device, called waveguide autocorrelator, is a more compact device where two detectors are fabricated on a single waveguide. As a proof of principle, the $g^{(2)}(\tau)$ measurement of a pulsed laser and a continuous-wave laser is demonstrated by using the waveguide autocorrelator. Furthermore, the closely-packed design of the waveguide autocorrelator is used to explore the crosstalk in our waveguide detectors. No crosstalk has been evidenced within the experimental error bar of 4 %.

In the sixth chapter a different type of detector, called waveguide photon-number-resolving detector (WPNRD) is discussed. While single-photon detectors behave as threshold detectors, photon-number-resolving detectors (PNRDs) resolve the number of photons at the input. By adding an integrated resistance parallel to each nanowire, it is possible to read out the sum of the detected signals with a single read-out. The WPNRDs consist of four-nanowires and therefore are shown to resolve up to four-photons. A device quantum efficiency of 24 % and 22 % for TE and TM polarisations are reported with a calculated maximum count rate of $> 50$ MHz. Moreover, it has been shown that the fidelity of WPNRDs is not significantly affected by the mode overlap difference between the central and lateral wires. Fast count rate, single read out and high efficiency at near-infrared wavelengths make these detectors very promising for high-speed quantum information processing.

Finally in the last chapter, the most relevant results obtained within this thesis and an outlook for the future work are summarised.

# Abbreviations

$\alpha_{TE(TM)}$: modal absorption coefficient in TE(TM) polarisation
$\beta_v$: propagation constant
$\Delta T_c$: transition temperature
$\eta$: efficiency
$\eta_i$: internal efficiency
$g^{(2)}(\tau)$: second-order correlation function
$\mu$-PS: micro-probe station
$\lambda$: wavelength
$\sigma$: standard deviation
$\tau_{1/e}$: 1/e decay time
$\eta$: coherence length
A: absorptance
AFM: atomic force microscope
$AL_2O_3$: sapphire (single crystal)
APD: avalanche photodiode
Ar: argon
CR: count rate
CW: continuous wave
d: thickness
D1(2): detector 1(2)
DBR: distributed-Bragg-reflector
DCR: dark count rate
DQE: device quantum efficiency
EBL: electron-beam lithography
ECR: electron cyclotron resonance
FP: Fabry-Perot
FWHM: full-width-half-maximum
GSG: ground-signal-ground
HBT: Hanbury-Brown and Twiss
HR-XTEM: high-resolution cross-section transmission electron microscopy
HSQ: hydrogen silsesquioxane (negative-tone resist)
$I_b$: bias current
$I_c$: critical current
$J_c$: critical current density

L$_{kin}$: kinetic inductance
L$_{\square}$: kinetic inductance per square
MgO: magnesium oxide
MMI: multi-mode interference coupler
N$_2$: nitrogen gas
Nb: niobium
NbN: niobium nitride
PhC: photonic crystal
PMMA: polymethyl methacrylate (positive-tone resist)
PMT: photo-multiplier tube
PNR: photon-number-resolving
PNRD: photon-number-resolving detector
QD: quantum dot
QE: quantum efficiency
QIP: quantum information processing
QKD: quantum key distribution
QPIC: quantum photonic integration circuit
qubit: quantum bit
RIE: reactive-ion etching
rms (or RMS): root-mean-square
RRR: residual resistivity ratio
R: resistance
R(T): temperature dependent resistance
SE: spectroscopic ellipsometer
SEM: scanning electron microscope
Si: silicon
Si$_3$ N$_4$: silicon nitride
S/N: signal-to-noise
SND: series nanowire detector
SPAD: single-photon avalanche detector
SPD: single-photon detector
SQE: system quantum efficiency
SSPD: superconducting single-photon detector
T$_{base}$: base temperature
T$_c$: critical temperature
T$_D$: Debye temperature
TCSPC: time-correlated single-photon counting
TE: transverse electric
TES: transition-edge sensor
TM: transverse magnetic
V: voltage
WHBT: waveguide Hanbury-Brown and Twiss
WPNRD: waveguide photon-number-resolving detector
WSi: tungsten silicide
WSPD: waveguide single-photon detector
w-PS: waveguide micro-probe station

# List of Publications

## Journal Publications

1. <u>D. Sahin</u>, A. Gaggero, Z. Zhou, S. Jahanmirinejad, F. Mattioli, R. Leoni, J. Beetz, M. Lermer, M. Kamp, S. Höfling, and A. Fiore, *Waveguide photon-number-resolving detectors for quantum photonic integrated circuits*, Appl. Phys. Lett.103, 111116 (2013)

2. <u>D. Sahin</u>, A. Gaggero, T. B. Hoang, G. Frucci, F. Mattioli, R. Leoni, J. Beetz, M. Lermer, M. Kamp, S. Höfling, and A. Fiore, *Integrated autocorrelator based on superconducting nanowires*, Opt. Express 21, 11162-11170 (2013)

3. S. Jahanmirinejad, G. Frucci, F. Mattioli, <u>D. Sahin</u>, A. Gaggero, R. Leoni, and A. Fiore, *Photon-number resolving detector based on a series array of superconducting nanowires*, Appl. Phys. Lett. 101, 072603-4 (2012)

4. J. P. Sprengers, A. Gaggero, <u>D. Sahin</u>, S. Jahanmirinejad, G. Frucci, F. Mattioli, R. Leoni, J. Beetz, M. Lermer, M. Kamp, S. Höfling, and A. Fiore, *Waveguide superconducting single-photon detectors for integrated quantum photonics*, Appl. Phys. Lett. 99, 181110-3 (2011)

5. A. Gaggero, S. Jahanmirinejad, F. Marsili, F. Mattioli, R. Leoni, D. Bitauld, <u>D. Sahin</u>, G. J. Hamhuis, R. Notzel, S. Sanjines, and A. Fiore, *Nanowire superconducting single-photon detectors on GaAs for integrated quantum photonic applications*, Appl. Phys. Lett. 97, 151108-3 (2010)

## Oral Presentations to National and International Conferences

1. *Waveguide photon-number-resolving detectors for quantum photonic applications* — Single-Photon Workshop, Oak Ridge TN, USA (2013)

2. *Single-photon and photon-number-resolving detectors integrated with waveguide circuits* — European Conference on Lasers and Electro-Optics (CLEO Europe), Munich, Germany, Post-deadline submission (2013)

3. *Waveguide superconducting single-photon autocorrelators for quantum photonic applications* — SPIE Photonics West, San Francisco CA, USA, in proceedings of SPIE 86351B (2013)

4. *Waveguide integrated quantum photonics: Superconducting single-photon detectors and autocorrelators* — Photon12, Durham, UK (2012)

5. *Integrated waveguide superconducting single photon detectors and autocorrelators* — IEEE Photonics Society Benelux Workshop, Eindhoven, The Netherlands (2012)

6. *Waveguide single photon detectors for integrated quantum photonic applications* — OSA Quantum Information and Measurement, Berlin, Germany in proceedings of Quantum Information and Measurement with Photons II QW3A.4 (2012)

7. *Waveguide - Integrated Single Photon Detectors* — Physics@FOM, Veldoven, The Netherlands (2012)

## Invited Talks

1. *Photon-number-resolving detectors for GaAs waveguide circuit* — SPIE Defence, Security and Sensing (DSS), Baltimore MD, USA (2014)

2. *Towards integrated quantum information photonics circuit: Fabrication and characterization of waveguide superconducting single photon detectors* — TUM-Walter-Schottky Institute, Munich, Germany (2012)

3. *Fabrication and characterization of waveguide single photon detectors for integrated quantum photonic applications* — Leiden University, Group of Quantum Optics and Quantum Information, Leiden, The Netherlands (2012)

# Acknowledgements

I would like to acknowledge several people in the following for their contribution to my work by one way or another.

First of all, I sincerely thank my promoter and daily supervisor, prof. dr. Andrea Fiore for giving me the opportunity to carry out this exciting and demanding project. I appreciated his availability and great interest to discuss the results as well as his useful comments and remarks throughout my project.

I would like to also thank prof. dr. Gregory Goltsman for being my second promoter and for his positive comments on my work. Moreover, I would like to acknowledge the rest of my defense committee: prof. dr. Jonathan J. Finley, prof. dr. Robert H. Hadfield, prof. dr. Erwin Kessels and dr. Jos van der Tol for their evaluations, and valuable feedback and comments.

This work was only possible thanks to a dedicated collaboration of several research labs in Europe within the project, QUANTIP. Therefore, I would like to express my sincere appreciation to dr. Roberto Leoni, dr. Franceso Mattioli and in particular dr. Alessandro Gaggero for fabricating the waveguide detectors in CNR-Rome, to prof. dr. Sven Höfling and prof. dr. Martin Kamp, and in particular Johannes Beetz for fabricating the waveguides and Matthias Lermer for growing the GaAs/AlGaAs heterostructures in University of Würzburg and also to dr. Mark Thompson and dr. Pisu Jiang for their contribution in the design of MMIs and the first characterisations of them in University of Bristol. I would like to acknowledge Alessandro also for the training on NbN film deposition in Lausanne which was the peculiar chance for me to learn about how to grow a superconductor material in the very beginning of my PhD adventure. I would like to extend my appreciation to dr. Beatriz B. Campo for preparing the NbN samples for TEM and dr. Marcel A. Verheijen for his great effort in taking HR-XTEM images. I would like to also thank prof. dr. Richard van de Sanden for authorizing me to use the ellipsometer in the PMP group and Jan-Willem Weber for his valuable help.

Half of this work was conducted in the NanoLab of TU/e, where life would not be as easy without the help of our talented technicians. Therefore, I would like to express my gratitude to Frank van Otten for his initial help on the sputter system, René Veldhoven for providing the DBR samples grown by MOVPE and Tjibbe de Vries for his support on the processing related issues with the optical lithography. Special thanks to Erik-Jan Geluk for his all time willingness to discuss the problems in any step of the processing in particular for SEM, EBL and sputtering and Barry Smalbrugge for sputtering and the chemicals. Barry, I will always remember your fatherhood attitude and our Turkish/Dutch discussions cheerfully, dankuwel voor alles!

I would like to acknowledge our academic staff members in the PSN group for their fruitful

# Curriculum Vitae

Döndü Şahin was born on 9 November 1984 in Ankara, Turkey. After finishing high school in June, 2002 at *Çankaya Atatürk Anadolu Lisesi* (mathematics and science division), she started studying Physics at *Middle East Technical University*. She completed her BSc studies with an honour degree in 2007 with a thesis on fabrication and characterisation of MOS structures. She continued her studies in the same university and received her MSc degree in 2009. She was involved in the research on structural and electrical properties of non-volatile memory cells with high-$\kappa$ tunnel oxide and with/without nanocrystals in the *Semiconductor Materials and Devices* group. After receiving her MSc degree, she started her PhD project in the *Photonics and Semiconductor Physics (PSN)* group at *Eindhoven University of Technology*. She was involved in the research on superconducting single-photon detectors, the main results of which are presented in this dissertation. She received the best poster prize in Fotonik 2013 for her PhD research.